ESCUELA POLITÉCNICA SUPERIOR DE ÁVILA

PROGRAMA DE DOCTORADO: INVESTIGACIÓN Y DESARROLLO EN GEOTECNOLOGÍAS.

DEPARTAMENTO DE INGENIERIA CARTOGRÁFICA Y DEL TERRENO

APLICACIÓN DE TÉCNICAS GEOFÍSICAS EN LA RESOLUCION DE PROBLEMAS GEOLÓGICOS, ESTRUCTURALES Y MINEROS A GRAN PROFUNDIDAD

TESIS DOCTORAL

Autor: Daniel Porras Sanchiz

Director de Tesis: Dr. Pedro Carrasco García

Ávila, noviembre de 2023

Informe de los supervisores de la Tesis Doctoral

"APLICACIÓN DE TÉCNICAS GEOFÍSICAS EN LA RESOLUCION DE PROBLEMAS GEOLÓGICOS, ESTRUCTURALES Y MINEROS A GRAN PROFUNDIDAD"

Presentada en el Departamento de Ingeniería Cartográfica y del Terreno por

Daniel Porras Sanchiz

La Tesis Doctoral titulada "Aplicación de técnicas geofísicas en la resolución de problemas geológicos, estructurales y mineros a gran profundidad", presentada por Daniel Porras Sanchiz, se engloba dentro de la línea de investigación de Energía correspondiente al Programa de Doctorado "Geotecnologías Aplicadas a la Construcción, Energía e Industria", y más concretamente, dentro de la rama de desarrollo y mejora de recursos geotérmicos.

La línea abordada se considera de gran relevancia para la comunidad científica internacional, con una clara propuesta de aplicación de metodologías de investigación en la resolución de problemas de diversa tipología donde la profundidad de investigación representa el factor limitante.

La tesis doctoral analiza, desde un punto de vista eminentemente práctico, las características y aplicabilidad de varias técnicas geofísicas que, dada su singular metodología de aplicación, permiten la resolución de problemas de tipo geológico, estructural y minero.

A través de la presente Tesis Doctoral, se ha podido identificar el potencial de aplicabilidad de las técnicas y metodologías aplicadas, y su importancia en el ámbito científico, hecho constatado por los artículos científicos publicados en revistas internacionales de impacto reconocido, los cuales han sido sometidos a los correspondientes procesos de revisión y evaluación crítica por parte de expertos internacionales de trayectoria reconocida.

Finalmente, la Tesis Doctoral presenta un apartado de conclusiones en el que se detallan, de forma precisa y concreta, las principales aportaciones de las investigaciones realizadas por el autor en el marco de la Tesis Doctoral, expuestas de manera que puedan ser objeto de un análisis crítico, así como constituir un punto de partida en el desarrollo de futuros trabajos integrados en esta línea de investigación.

Ávila, 10 de noviembre de 2023

CARRASCO GARCIA PEDRO - 70808154D

Firmado digitalmente por CARRASCO GARCIA PEDRO - 70808154D
Fecha: 2023.11.09 10:17:58 +01'00'

Dr. Pedro Carrasco García

Listado de Publicaciones

La presente tesis doctoral consiste en un compendio de tres artículos científicos publicados en revistas internacionales con alto índice de impacto, los cuales se enumeran a continuación:

- Imaging extensional fault systems using deep electrical resistivity tomography: A case study of the Baza fault, Betic Cordillera, Spain.
  Journal of Applied Geophysics, Volume 202, 2022, 104673, ISSN 0926-9851, https://doi.org/10.1016/j.jappgeo.2022.104673.

- Drone Magnetometry in Mining Research. An Application in the Study of Triassic Cu–Co–Ni Mineralizations in the Estancias Mountain Range, Almería (Spain).
  Drones 2021, 5, 151. https://doi.org/10.3390/drones5040151

- Deep TDEM Study for Structural and Mining Purposes: A Case Study of the Barbastro Saline-Evaporitic Formation, Spain.
  Appl. Sci. 2023, 13, 6385. https://doi.org/10.3390/app13116385

No quiero creer, quiero saber

Carl Sagan

Agradecimientos

A Tania, Daniela e Iván, pilares fundamentales en mi vida, a los que os he robado un tiempo precioso a lo largo de estos años para culminar un camino académico importante para mí. Espero que haya valido la pena. Este trabajo también os pertenece. Amor eterno.

A mis padres y hermanas.

A mi director de tesis Pedro Carrasco García. Sin tu apoyo constante e incondicional este trabajo no hubiera sido posible. Muchas gracias por tu ejemplo, consejo y ayuda durante todos estos años.

A mis compañeros de trabajo, especialmente a Javier Carrasco, Pablo González y José Luís Herrero. Por los buenos y malos momentos que hemos pasado tirando y recogiendo cables, pensando y discutiendo, así como por el esfuerzo recíproco que nos ha permitido llegar donde hoy estamos, y, sobre todo, hasta donde llegaremos. Lo mejor siempre está por llegar. Ha sido un placer y un privilegio trabajar junto a vosotros estos años. Sin vuestra ayuda esta tesis no habría sido posible, gracias por vuestro trabajo, consejo, paciencia y apoyo.

A Antonio Pineda Velasco, compañero de fatigas y de interminables charlas, gracias por contar con tu ayuda.

Por último, agradecer a Pedro Carrasco Morillo, porque no sabría mucho de lo que sé si no hubiera sido por la gratitud de compartir tu conocimiento, así como haber tenido la oportunidad de trabajar contigo.

Abstract

Applied Geophysics is a branch of science that allows for the determination of the subsurface structure and composition through the processing and interpretation of various physical parameters obtained with a series of equipment and sensors. Currently, applied geophysics serves as a powerful tool in addressing various constantly evolving issues in different fields, such as geological and structural analysis, geotechnics, hydrogeology, mining, etc. One of its primary advantages is that it employs non-destructive indirect techniques that provide valuable data for solving various challenges.

Throughout this thesis, the applied techniques and methodologies contribute to advancements in addressing a wide range of problems. Specifically, it deals with geological, structural, and mineralogical issues at significant depths. In particular, the following techniques have been employed: magnetometry, deep electrical resistivity tomography (DERT), and time-domain electromagnetic surveys (TDEM). The advancement proposed in this thesis is based on an innovative approach to the application of geophysical techniques, resulting in an innovative methodology that expands their scope of use while simultaneously reducing classical limiting factors, such as investigation depth.

The applied methodologies aim to improve both the depth of investigation and performance (productivity), enabling significant spatial coverage over complex areas that enhances data quality and, therefore, increases spatial resolution and resolving capacity.

This innovative approach has allowed for the study of geological formations and deep structures, some of which are of mining interest, as well as active regional fault zones with seismotectonic implications, where deep analysis is a fundamental aspect.

Resumen

La Geofísica aplicada es una rama de la ciencia que permite determinar la estructura y composición del subsuelo a partir del procesado e interpretación de diversos parámetros físicos obtenidos con una serie de equipos y sensores. En la actualidad, la geofísica aplicada se muestra como una potente herramienta en la resolución de diversas problemáticas en constante desarrollo en diferentes campos, tales como el análisis geológico y estructural, geotécnia, hidrogeología, minería, etc. contando como una de sus principales ventajas, el constituir técnicas indirectas no destructivas que aportan datos en la resolución de diversas problemáticas.

A lo largo de la tesis, las técnicas y metodologías aplicadas permiten un avance en la resolución de problemas de diversa tipología. En especial, se aborda la resolución de problemas geológicos, estructurales y minerales situados a profundidades notables. En concreto, se ha trabajado con las técnicas de la magnetometría, tomografía eléctrica profunda (DERT), y sondeos electromagnéticos en el dominio del tiempo (time-domain electromagnetics TDEM). El avance que se plantea en la presente tesis se basa en una aproximación novedosa a la aplicación de las técnicas geofísicas empleadas, que se traduce en una metodológica innovadora que amplía su campo de uso, reduciendo, al mismo tiempo, los factores limitantes clásicos de aplicación de las mismas, tales como la profundidad de investigación.

Las metodologías aplicadas persiguen alcanzar una mejora en la profundidad de investigación, así como en su rendimiento (productividad), permitiendo coberturas areales significativas en entornos complejos que redundan en la mejora de la calidad de los datos y, por tanto, incrementando la resolución espacial y capacidad resolutiva de las mismas.

Este enfoque novedoso ha permitido el empleo en el estudio de formaciones geológicas y estructuras profundas, algunas de ellas con interés minero, así como zonas activas de fractura de carácter regional con implicaciones sismotectónicas, donde el análisis a grandes profundidades es un aspecto fundamental.

INDICE

Capitulo 1 INTRODUCCIÓN

1.1. Introducción

Históricamente, la obtención de datos precisos acerca de las características del subsuelo ha representado una barrera de cara al desarrollo de investigaciones, proyectos constructivos o de aprovechamiento económico (minería, geotermia, etc.). Esta barrera ha sido especialmente importante en el caso de estudios a gran profundidad, donde las metodologías y sistemas tradicionales cuentan con resoluciones espaciales muy variables, limitaciones de aplicabilidad, así como costes muy elevados, dificultando y limitando su aplicabilidad final, donde únicamente en grandes proyectos se justificaba su empleo.

En la actualidad, el avance tecnológico está generando la aparición de técnicas y metodologías de investigación geofísica novedosas que permiten alcanzar y solventar muchas de las limitaciones históricas, permitiendo alcanzar profundidades elevadas e incrementando notablemente el grado de resolución espacial. Estos avances permiten su aplicación en la resolución de múltiples problemáticas tales como geología estructural, análisis de fallas activas con implicación sismotectónica, geología económica, etc.

Los resultados obtenidos en los artículos realizados en la presente tesis doctoral muestran como las metodologías o configuraciones aplicadas constituyen un importante avance que permitirá servir de referencia a otros trabajos, tanto de investigación académica como en la industria al proponer mejoras en los aspectos limitantes de toda técnica geofísica, multiplicando el valor tecnológico y económico.

La hipótesis de trabajo en los artículos se basa en la existencia de limitaciones de aplicabilidad de las técnicas de investigación geofísica tradicionales en la resolución de problemas geológicos, estructurales y mineros, ligados a factores como la penetración (profundidad de investigación), resolución espacial, costes y dificultad de acceso.

Los aspectos novedosos obtenidos en la presente han sido:

- Diseño de nuevas metodologías (configuraciones) de trabajo que permitan analizar cuerpos o estructuras a gran profundidad, mejorando la resolución espacial y solventando limitaciones de acceso y aplicabilidad en terrenos con dificultades de acceso, ya sean topográficos o de vegetación, incrementando la productividad y mejorando los costes de ejecución.
- Resolución de problemas geológico-estructurales. Aplicación a estudios sismotectónicos en fallas activas a gran profundidad, habilitando la definición geométrica y cinemática de las mismas proporcionando datos esenciales para mejorar la evaluación del potencial sismogénetico de las mismas.
- Resolución de problemas geológicos y mineros. Aplicación a estudios de geología y minería aplicada, permitiendo la localización del recurso y su geometría lo que define el potencial geológico y minero de la zona permitiendo el diseño y optimización de futuras actividades de investigación y explotación.

1.2. Motivación y Objetivos

La tesis doctoral ha contado con la siguiente motivación:

- Contribuir al avance en el conocimiento en el campo de la geofísica aplicada y su aplicabilidad a problemas de gran interés académico, profesional, así como propio, lo que ha constituido una motivación muy importante a la hora de abordar este trabajo.
- Una tesis doctoral constituye el último paso de un largo recorrido a nivel académico, que continuará con futuras investigaciones y artículos que complementen y avancen en la línea de investigación seleccionada en esta tesis doctoral.

Los objetivos de la tesis doctoral han sido los siguientes:

- Plantear una investigación original y significativa que contribuya a la mejora del conocimiento y aplicabilidad en el campo de la geofísica aplicada. En este caso, se abordan problemáticas clásicas en la geofísica aplicada tales como la limitación en la penetración (profundidad de investigación), resolución espacial, costes y dificultad de acceso en entornos agrestes sobre objetos de investigación variados de tipo geológico y minero.
- Publicación y difusión de las metodologías y resultados obtenidos de manera que sean accesibles a la académica e industria, en este caso, mediante artículos científicos en revistas de referencia.

Capítulo 2 ARTÍCULOS

ARTICULO 1: Imaging extensional fault systems using deep electrical resistivity tomography: A case study of the Baza fault, Betic Cordillera, Spain

Resumen:

La evaluación de la peligrosidad sísmica de fallas tectónicas actuales puede verse mejorada estudiando su estructura y cinemática. Estas características se han determinado principalmente mediante estudios geológicos de superficie de la traza aflorante de las fallas, segmentación estructural lateral o trincheras paleosísmicas. Todos estos enfoques se basan principalmente en un análisis bidimensional de los afloramientos superficiales, mientras que el conocimiento de las fallas en profundidad sigue siendo en gran medida inaccesible.

Para mejorar estas limitaciones, pueden aplicarse métodos geofísicos que permitan establecer información detallada sobre la morfología y segmentación de las fallas en profundidad. En este trabajo se analizan los resultados novedosos de un estudio de tomografía eléctrica de resistividad profunda de la Falla de Baza, una falla tectónica activa que controla la geometría de la Cuenca Intramontañosa Neógena de Baza (Cordillera Bética, España). La interpretación de nuestro modelo de resistividad preferido revela la estructura detallada hasta aproximadamente 1.000 m de profundidad. El estudio muestra un sistema de fallas normales complejo con una anchura mínima de 2 km, con bloques limitados por fallas normales potencialmente lístricas que generan la rotación de los mismos. Este estudio presenta evidencias de la falla de Baza (F3), coincidente con los principales escarpes topográficos. Sin embargo, el modelo geofísico y la evidencia geomórfica también apoyan una nueva ramificación (F1) que podría ser una fuente sismogénica adicional. La técnica de prospección geofísica presentada en este estudio proporciona datos esenciales para mejorar la evaluación del potencial sismogenético de la falla de Baza.

Journal of Applied Geophysics 202 (2022) 104673

Contents lists available at ScienceDirect

Journal of Applied Geophysics

journal homepage: www.elsevier.com/locate/jappgeo

Imaging extensional fault systems using deep electrical resistivity tomography: A case study of the Baza fault, Betic Cordillera, Spain

Daniel Porras [a], Javier Carrasco [a], Pedro Carrasco [a], Pablo J. González [b,*]

[a] Dpto. Ingeniería Cartográfica y del Terreno. Geología, Escuela Politécnica Superior de Ávila, Universidad de Salamanca, Avd. Hornos Caleros nº 50, 05003 Ávila. Spain
[b] Department of Life and Earth Sciences, Instituto de Productos Naturales y Agrobiología (IPNA-CSIC), Av. Astrofísico Francisco Sánchez, 3, 38206 San Cristóbal de La Laguna, Santa Cruz de Tenerife, Spain

ARTICLE INFO

Keywords:
Normal faulting
Deep electrical resistivity tomography
Present-day tectonics
Baza Basin
Betics
Seismic hazard assessment

ABSTRACT

Seismic hazard assessment of present-day tectonic faults may be improved by studying their structure and kinematics. These features have been mainly determined by surface geological studies of exposed fault traces, structural lateral segmentation or paleoseismic trenches. All these approaches rely mainly on two-dimensional analyses of surface outcrops, while knowledge of the faults at depth remain largely inaccessible. To improve on such limitations, geophysical methods can be applied to establish detailed information on fault morphology and segmentation at depth. This work analyzes new results of a deep electrical resistivity tomography survey acquired across the Baza Fault, a present-day tectonic fault that controls the geometry of the Neogene intramountainous Baza Basin (Betic Cordillera, Spain). Interpretation of our preferred resistivity model reveals its detailed structure down to approximately 1000 m depth. The survey shows a minimum 2 km wide complex normal fault system, with rotational tilting blocks bounded by potentially listric normal faults. This study presents subsurface evidence of the Baza fault (F3), coincident the main topographic scarps. However, the geophysical model and geomorphic evidence also support a fault branch (F1) that might be an additional active seismogenic source. The geophysical survey technique presented in this study provides essential data to improve assessment of the seismogenic potential of the Baza Fault.

1. Introduction

There is strong evidence that the seismogenic potential of a fault depends, to a large degree, on its geometry (Wesnousky, 2008; Pace et al., 2016). In particular, its magnitude depends on the maximum spatial extent of the fault rupture propagation during seismic events. Therefore, better understanding of the geometry of a fault system is essential to understand seismogenic processes and, from a practical point of view, its future seismic potential (Scholz, 2019; Biasi and Wesnousky, 2017). Most relevant studies have made progress in characterizing their lateral segmentation and geometry, mainly due to easy access to surface expression of faults. However, the fault geometries at depth remain largely unknown. For instance, this lack of knowledge affects the estimated maximum rupture, which mainly relies on surface slip profiles and empirical fault-length relationships (Wells and Coppersmith, 1994).

The Baza Fault is one of the major active faults in the Betic Cordillera (Fig. 1). It presents background seismicity with low-magnitude events (Fig. 2), during the historical and instrumental record periods (IGN (Spanish Instituto Geográfico nacional) seismic Catalogue, 2020; Martínez-Solares and Mezcua, 2002). The largest historical earthquake (M_w 6.0) occurred in 1531 CE, known as the Baza earthquake, destroying Baza and Benamaurel towns (Sanz de Galdeano et al., 2012). The Baza fault kinematics indicate predominant normal faulting with a minor strike-slip component. Previous studies have established it as an active and potentially seismogenic fault source (Sanz de Galdeano et al., 2012; Medina-Cascales et al., 2020). However, those estimates are mainly based on its surface expression. Therefore, new work is necessary to constrain the fault geometry and segmentation, in particular at depth.

In this study, the data and models arising from a new geoelectrical survey are presented. The geoelectrical profile with 4.5 km-long was acquired across the Baza Fault in its south-western sector. The relatively large aperture of this survey allowed us to reach greater depths than usual, improving our knowledge of the deep (1000 m depth) fault structure and characteristics. Resistivity surveys have been widely applied in mining, geology, engineering and environmental studies to

* Corresponding author.
E-mail address: pabloj.gonzalez@csic.es (P.J. González).

https://doi.org/10.1016/j.jappgeo.2022.104673
Received 6 May 2021; Received in revised form 25 March 2022; Accepted 9 May 2022
Available online 12 May 2022

solve multiple problems, including structural and active seismic zones, and provide high-resolution subsurface resistivity models at shallow depths <200 m (Kolawole et al., 2018; Suzuki et al., 2000; Steeples, 2001), which is the usual length of cables used in industry. The deep electrical resistivity tomography (DERT) is a specific survey acquisition and modeling method that analyzes larger depth ranges, usually between 500 and 1500 m depth. These have been specifically applied in the study of structural and active seismic zones (Balasco et al., 2011; Günther et al., 2011; Pucci et al., 2016; Rizzo et al., 2004).

In this study, a 2D deep electrical resistivity tomography model was obtained applying a damped least squares inversion. Model selection was carried out using automatic methods, trading-off data misfit and model complexity. The preferred final model compared favourably against literature, geological-structural data and previously available geophysics. It allows for an improved, new and detailed geological and structural view of the Baza Fault at depth. The model suggests that the system is segmented with several normal faults. Some normal fault branches were not previously recognized and might not be currently active. However, an unmapped fault branch shows geomorphic evidence for recent Quaternary fault slip. The fault system features separate rotational tilting blocks, indicating a potential listric geometry at greater depths (>1000 m). The new results confirm and extend previous surveys establishing the fault geometry and kinematics using surface analysis, available geophysical data, gravity (Alfaro et al., 2008) and seismic methods (Haberland et al., 2017). Hence, our study contributes to the seismic hazard assessment, and generally to tectonosedimentary reconstruction of the Baza basin, e.g., basement throw estimation.

2. Geological setting

The Baza Fault is located in the Baza Basin, a sub-basin within the main Guadix-Baza Basin. The wider Guadix-Baza Basin is the largest intramontane Neogene basin in the Betic Cordillera (Vera, 1970a, 1970b). This Cordillera is an orogen resulting from a Neogene NNW – SSE oblique convergence of 3–5 mm/year between the Eurasian and Nubian plates (Nocquet, 2012; Palano et al., 2015). The shortening is synchronous with an ENE-WSW orogen-parallel extension (Galindo Zaldívar et al., 1999; Marín-Lechado et al., 2017). The regional ENE–WSW extension in the central Betics accomodates between 0.5 and 1.5 mm/yr (Palano et al., 2013). This tectonic extension rate is accommodated by NNW–SSE-striking normal faults like Baza Fault (Galindo Zaldívar et al., 1989, 1999; Sanz de Galdeano et al., 2012; Sanz de Galdeano et al., 2020), further developing the basins (e.g., Baza basin).

The Baza Fault delimits the NNW-SSE border of the Baza Basin (Galindo Zaldívar et al., 1999). With more than 35 km of surface topographic expression, the Baza Fault is a normal fault system with a relatively acute curved trace. The fault system strikes from N-S at the northern end to a NW-SE trend at its middle-southern termination. Overall, it presents numerous parallel splays, increasing in number towards the southern end. The Baza Fault dips from 45° to 65° to the East (Alfaro et al., 2008; Sanz de Galdeano et al., 2012; Haberland et al., 2017), with an inferred vertical slip rate of 0.12–0.49 mm yr^{-1} calculated using the displaced glacis (ca. 500Kyr - García Tortosa et al., 2011; Sanz de Galdeano et al., 2012). The fault seems to have been active since the Late Miocene (García-García et al., 2006). The relatively fast fault slip rate of the Baza Fault generates a half-graben structure on its hanging wall, with a maximum sediment thickness of 2200 m based on

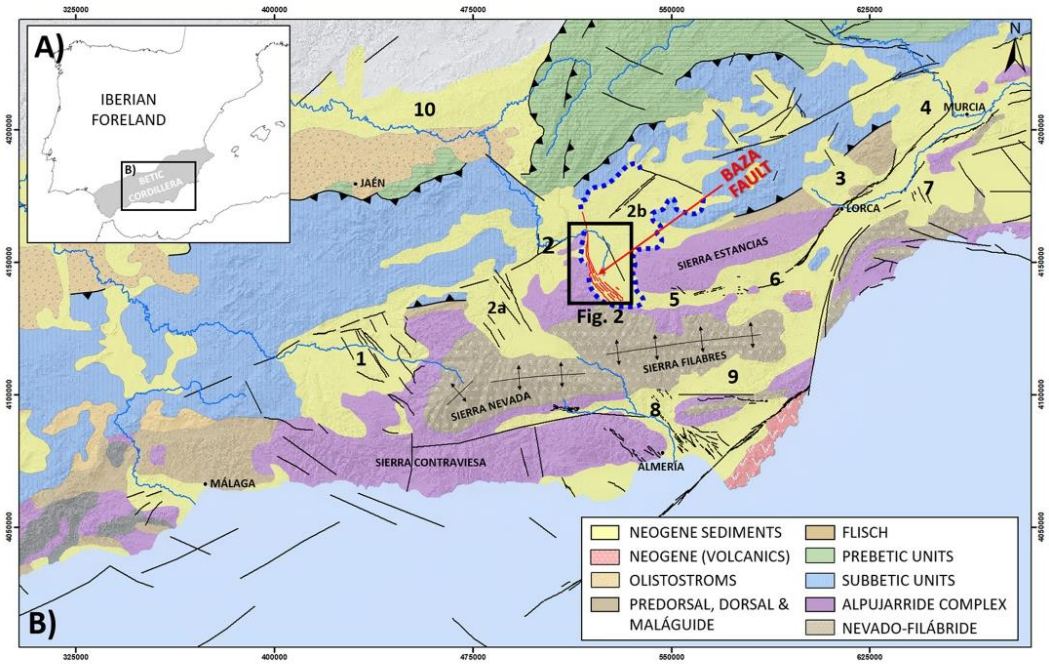

Fig. 1. A) Location of the Betic Cordillera. B) Simplified geological map of the Betic Cordillera. Numbers indicate intramontane sedimentary basins. 1: Granada basin; 2: Guadix-Baza Basin; 2a: Guadix subbasin; 2b: Baza subbasin; 3: Lorca basin; 4: Mula-Fortuna basin; 5: Almanzora corridor; 6: Huerca Overa basin; 7: Totana basin; 8: Tabernas basin; 9: Sorbas basin. Blue dotted line indicates the limits of the Baza subbasin, and black rectangle shows the Fig. 2 location. (For interpretation of the references to colour in this figure legend, the reader is referred to the web version of this article.)

seismic surveys (Haberland et al., 2017). The basin was filled by sediments over Triassic metamorphic basement rocks from the Alpujarride Complex (García-Dueñas et al., 1992; Orozco and Alonso-Chaves, 2002). Baza Basin infills consist of Upper Miocene marine deposits, which transition upwards into continental deposits during the Pliocene / Pleistocene age. The progressive uplift disconnecting the basin from the Mediterranean Sea was caused by this transition (Vera, 1970a, 1970b; Soria et al., 1998; Rodríguez-Fernandez et al., 2012). Later on, the higher subsidence of the hanging wall of the Baza Fault generated an endorheic fluvial and lacustrine system until the late Pleistocene, through capture of its drainage system by the Guadalquivir fluvial network (Sanz de Galdeano and Vera, 2007; Sanz de Galdeano et al., 2012; Alfaro et al., 2008). The Quaternary sedimentation is restricted to depressed areas, forming alluvial fans and piedmont systems, which are affected frequently by the Baza Fault slip, generating stepped fault scarps (García Tortosa et al., 2008; García Tortosa et al., 2011; Castro et al., 2018).

2.1. Previous geophysical studies

The Baza basin structure and its *syn*-tectonic infilling sedimentation have been extensively studied at regional scale (basin-wide). However, there is scarce information about the detailed subsurface structure of the basin near the Baza Fault. Previous studies were mainly based on the use of surface geological and geomorphological data (Sanz de Galdeano and Vera, 1992; Soria et al., 1998; Rodríguez-Fernandez et al., 2012). Recent work further suggests a tectono-stratigraphic evolution from 6 Ma to 0.6 Ma, marked by a long sedimentary history. The Baza fault induced more than 1000 m of subsidence, supported by geological evidence and migrated P-receiver functions that indicate variable crustal thicknesses under the hanging wall and footwall of the Baza fault (Pérez-Peña et al., 2018).

Alfaro et al. (2008) carried out a gravimetric study, recording negative anomalies. Those anomalies are the maximum negative values found in the entire Betic Cordillera. The gravity anomaly map shows two gravity minima along the Basin axis running parallel along the fault strike: one south of the village of Benamaurel, and a secondary one at the southeast of Baza town. The inferred basin structure in this study estimated a 2000–3000 m throw in the basement, with the southern section formed by a structurally simple half-graben and the northern area significantly more complex, with various fractures compartmentalizing the basement.

In 1977, a seismic reflection line was shot crossing the Baza fault and the western part of the basin (BT-2 seismic line, ITGE, 1999). This line struck NNW-SSE, and obliquely crossed the Baza fault. The survey results were not favorable enough to illuminate the fault zone or the basin's structure, due to its orientation with respect to the Baza fault strike. However, it revealed tectonic complexity with some associated synthetic and antithetic faults. The BT-2 seismic line showed the contact between the acoustic basement and the sedimentary basin infill, with the alternation of strong reflectors and transparent levels. In addition, the ESCI-Béticas project contained two deep-seismic profiles in the Baza Basin (García-Dueñas et al., 1994; Jabaloy et al., 1995). Due to the focus on imaging the complete crust structure, this survey did not show detailed structural information on the basin (Jabaloy et al., 1995). Only a small reflectivity layer in the upper part (0–2 s) confirmed the asymmetric shape of the basin sediments and the inferred active western boundary fault, the Baza fault. Finally, Haberland et al. (2017) shot three high-

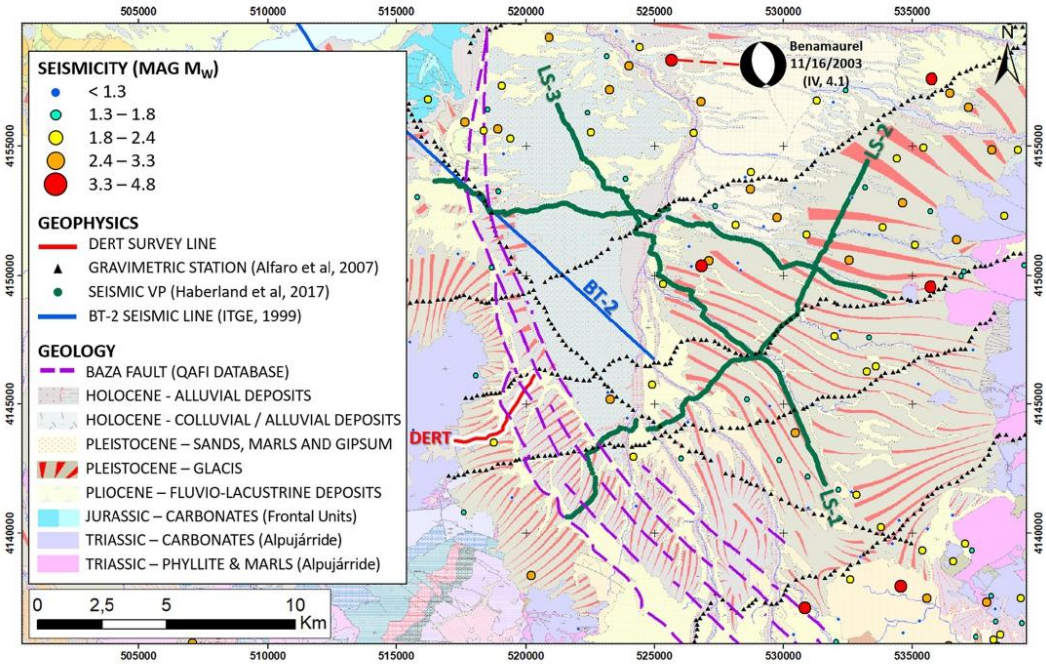

Fig. 2. Geological map of the southern part of the Baza Basin. Deep electrical resistivity tomography survey line is displayed (red line) with the Baza Fault trace with its different splays (Quaternary Faults Database of Iberia (QAFI)), previous geophysical surveys (gravimetric and seismic), and seismicity, including the 4.1 Benamaurel earthquake focal mechanism (Instituto Andaluz de Geofísica, https://iagpds.ugr.es/). (For interpretation of the references to colour in this figure legend, the reader is referred to the web version of this article.)

resolution deep-seismic profile lines across the basin and fault in different directions. The study revealed and confirmed the asymmetric shape of the infilling sediments. It detected the continuance at depth of the Baza fault and several others throughout the basin, affecting the deeper sedimentary layers. The seismic study also constrained the maximum sediment thickness to 2200 m.

2.2. Seismicity of the Baza fault

The Baza Fault is one of the most active faults in the central Betic Cordillera, presenting a general low-magnitude seismicity during the historical and instrumental record (Spanish Instituto Geográfico Nacional (IGN) catalogue; Martínez-Solares and Mezcua, 2002), with an important maximum historical earthquake in 1531 (VIII-IX) (Martínez-Solares and Mezcua, 2002). This event is known as the Baza earthquake, and was estimated at a magnitude of M_w 6.0. This earthquake destroyed the original settlements of Baza and Benamaurel (Sanz de Galdeano et al., 2012). There is also geological evidence of previous large events, with the presence of seismites or liquefaction features, and earthquake-induced landslides (Alfaro et al., 1997; Gibert et al., 2005).

The seismogenic potential of the Baza Fault was preliminarily estimated by Sanz de Galdeano et al. (2012) to be of the order of M_w 6.9 (Wells and Coppersmith, 1994). More recent estimates for M_{max}, to predict if a future seismic event would rupture the entire Baza fault, range from Mw 6.2 to Mw 7.1 using different empirical laws, and highlight the considerable uncertainties involved (Medina-Cascales et al., 2020).

3. Data and methodology

3.1. Electrical resistivity tomography for fault detection

Electrical Resistivity Tomography (ERT) is a widely used geophysical technique. Among many applications, it has been successfully applied to image subsurface structures and, in particular, faults (Suzuki et al., 2000; Steeples, 2001; Caputo et al., 2003; Kolawole et al., 2018). The ERT method is based on taking measurements of ground resistivity along a connected line or array, by applying an electric current to the subsurface via two metal stakes (*current electrodes*) coupled to the ground. The current passing through the ground sets up an electrical potential in the subsurface. The difference in electrical potential between two additional *potential electrodes* is measured as a voltage. Using Ohm's law, this voltage can be converted to values of apparent resistivity for the ground between the two potential electrodes. Measurements are repeated, rolling over in sets of four electrodes. To reach greater depths, four electrodes with a wider spacing are selected, usually a multiple of the first set. This is repeated with wider separations, in this way increasing the effective depth of the survey. A subsurface ground-resistivity image or pseudo-section is generated using the input current, measured voltage and the array geometry (Edwards, 1977). Hence, the array geometry varies and determines the survey sensitivity, with its two main parameters being the array spacing and aperture. The separation between electrodes controls the spatial resolution, while the depth penetration depends strongly on the total distance spanned by the electrode array.

Fault detection is based on resistivity contrasts in the subsoil between the geological units, which provide information on the physical conditions of the rocks (Caputo et al., 2003; Drahor and Berge, 2017; Storz et al., 2000). Despite its usefulness, the geoelectrical method to investigate the Baza Fault system has not applied in previous studies. Here, a modification of the deep ERT (DERT) is applied, aiming to reach greater depths. DERT has been applied to study deep structures including faults and active seismic zones (Balasco et al., 2011; Günther et al., 2011; Pucci et al., 2016; Rizzo et al., 2004), the shape of basins and infilling materials geometry and characteristics (Rizzo et al., 2019; Rizzo and Giamapolo, 2019), and also, geothermal systems (Carrier et al., 2019; Troiano et al., 2019).

3.2. Survey and data acquisition

During the study, ERT data were collected over a line with 4.5 km length. The array was set up across the southern sector of the Baza Fault. In that region, the fault system strikes NW–SE, and it is composed of several splays with a local width of about 2.5 km (Fig. 2). The line was acquired using a roll-along acquisition technique dividing the total line length into two segments. Segments were deployed using two 3 km lengths of multicore reversible cable with electrode separation of 100 m. A Syscal Pro resistivity meter was used, with a 1200 W AC/DC converter. The recording array selected was Pole-Dipole, deploying an infinite electrode orthogonal to the line direction with a minimum offset of 5 km, designed with a 100 m X spacing and n values from 1 to 29, with a total 435 data points (Fig. 3-1). This array configuration was selected to obtain high penetration capability, strong signal and high-density data (Carrasco García, 2013). A 50% segment length overlap was used to avoid loss of information at depth (Fig. 3-2). The inversion was based on a model of 364 blocks distributed in 11 model layers, where the minimum pseudodepth was 51.9 m and maximum 899.4 m.

Data quality in ERT during acquisition depends on three factors, resistivity of the materials, noise, and contact resistance. The first two factors are mitigated by using a high-power transmitter and an AC/DC converter, incrementing the effective working voltage. The third factor impact depends on the resistivity of the most superficial layer of the terrain. In case of not allowed contact resistances, over 2000 Ohm for conductive and 20,000 Ohm in resistive materials (heuristic criteria) longer and/or multiple linked electrodes are installed at the electrode position, and if needed, enhancing the galvanic contact of the electrodes with the ground can be enhanced by adding salt water solution. Electrode locations were determined using a handheld GPS with a horizontal accuracy ≈3 m. Topography heights were extracted for the GPS coordinates and a 5 m resolution DEM (Instituto Geográfico Nacional, https://centrodedescargas.cnig.es/CentroDescargas/index.jsp). The elevation values of each data point were used during the data inversion.

3.3. Inverse modeling strategy

The following data processing approach was applied. The field raw data (binary) into ASCII format to numerically process the field datasets were converted. Using X2IPI software, outlier data points were removed following criteria that there were un-measured intensities or that measurement was less than 100 mA (Robain and Bobachev, 2002). Then, the two roll-along survey segments were combined into a single 2D data file. Topographic data were assigned to each node. Finally, the apparent resistivity data were inverted via using a linearized least-squares algorithm to obtain true resistivity models (Loke and Dahlin, 2002). The ERT data was modeled using the commercial RES2DINV software (Loke and Barker, 1995). This code utilizes a finite element or a difference algorithm to obtain the forward modeling of the voltage response to current injection. The resistivity models produced by RES2DINV are divided into a number of rectangular blocks with specific resistivity values derived from the field measurements. Apparent resistivity data is finally presented as a pseudo-section, a contour diagram in which apparent resistivity values are assigned depending on the array type, to a predefined location (Telford et al., 1990).

The inversion method selected was the smooth L2 norm or smoothness-constrained least-squares optimization method, depending on a damping factor. The L2 norm is supposed to minimize the sum of squares between the observed and calculated apparent resistivity values, generating smooth variations in resistivity within the inversion model. The inversion process starts from the initial model parameters and damping factors, which are refined by an iterative process (Lines and Treitel, 1984). The discrepancy between the calculated values of apparent resistivity and those inferred from field data are expressed

Fig. 3. 1) Sketches of the designed acquisition array configuration, the array consisted of 31 nodes with 100 m spacing and $n = 1$ to 29. 2) Sketch of data points distribution, highlighting the 50% recording segment length overlap.

through the root mean square (RMS).

The model results depend on the damping factor and number of iterations. Therefore, the effect of the number of iterations was evaluated for this investigation (Fig. 4). The effect was analyzed by running different inversions while varying the number of iterations, a procedure known as convergence curve method. The curve displays how the RMS misfit error varies with the number of iterations. As shown in Fig. 4-a, the curve shows an RMS value of 42.09% for the first iteration and a final RMS value of 22.75% after 10 iterations. The RMS misfit between the observed and computed data (RMS) rapidly decreases before the 3rd iteration and stabilizes with a minor decrease after the 6th iteration. This indicates that to obtain stable model results with our discretization and dataset the number of iterations should be between 3 and 6.

The effect of the starting range of damping factors was also tested. The optimal damping factor is found iteratively but can be affected by the initial values. RES2DINV allows selection of an initial and minimum pair of damping factors, as initial values. Therefore, 10 experiments were conducted (Fig. 4-b) and different sets of initial and minimum damping factors, following by a one-fifth rule to establish the minimum were provided (Loke, 2019, Geotomo Software). As already shown, the number of iterations rapidly reduces the RMS of the data misfit. The curves obtained show that there are no significant variations in the inversion results based into the initial damping factor variations, indicating that the software inversion routine obtains an optimum smoothing automatically, with little necessity of fine-tuning (Fig. 4-b). According to this analysis, subsequent models were obtained fixing the initial and minimum damping factors as 0.4 and 0.08 respectively.

4. Inversion results

According to the choice of inversion parameters from the previous section, two geoelectric models representing smoother and rougher possible solution were selected for further discussion (Fig. 5). Model A represents an example of a smooth model and higher misfit value, while Model B is our preferred model (parsimonious model). Model B is preferred because it is the smoothest model that achieves the lowest RMS value in the lowest number of iterations. Increasing the number of iterations do not further improve misfit levels. Models with higher model iterations do not achieve lower RMS values (Fig. 4A). Model A was obtained at iteration 3, and shows an RMS of 28.79% (Fig. 5-1). This model shows great variability in resistivity values, ranging from 20 up to more than 3000 Ohm•m. The main characteristic of the model is the presence of two resistive bodies (A and B), and two conductive zones (C and D). The two resistive bodies ($\rho > 1500$ Ohm•m) are located in the western part of the profile, outcropping (A), and in the central section along the model's deeper sections (B). The anomalies lack strong resistivity gradient transitions (> 500 Ohm•m/100 m) in resistivity values to the conductive zones. However, the eastern half of the profile is dominated by conductive materials (D) ($\rho < 400$ Ohm•m), although these materials are overlaid by subhorizontal anomalies with higher resistivity values (E). There is also a conductive body (C) present in the deeper parts, located to the SW of the modeled profile. Between the 800 and 1600 m profile length marks, the model shows greater variability in resistivity at shallow depths, forming a region with increased heterogeneity of resistive and conductive anomalies (F).

Model B was obtained after iteration 6, and shows an RMS of 23.1% (Fig. 5-2). It presents some notable variations with respect to model A.

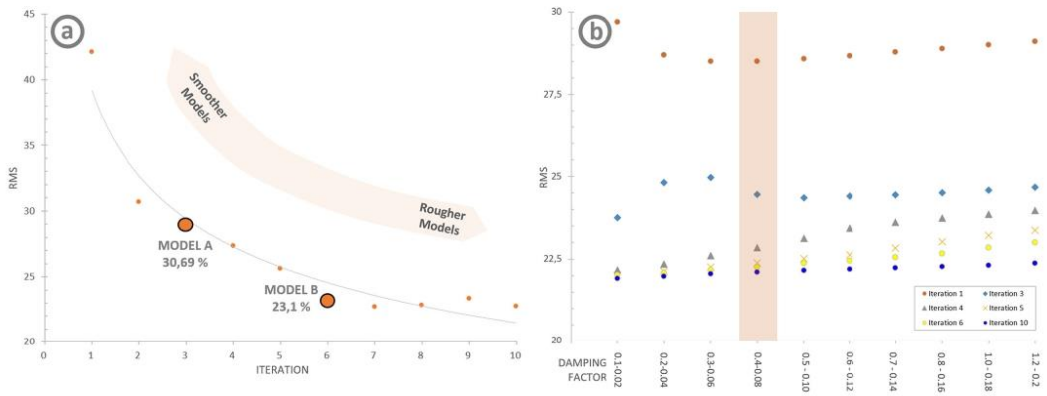

Fig. 4. a) RMS misfit variation as a function of the number of iterations to search for the optimal damping factor; b) Results of the automatic search for the regularized least squares inversion. Increasing the number of iterations decreases the RMS of the models rapidly but this flattens after a third iteration. In addition, the starting damping factor does not strongly affect the final misfit of the inverted models.

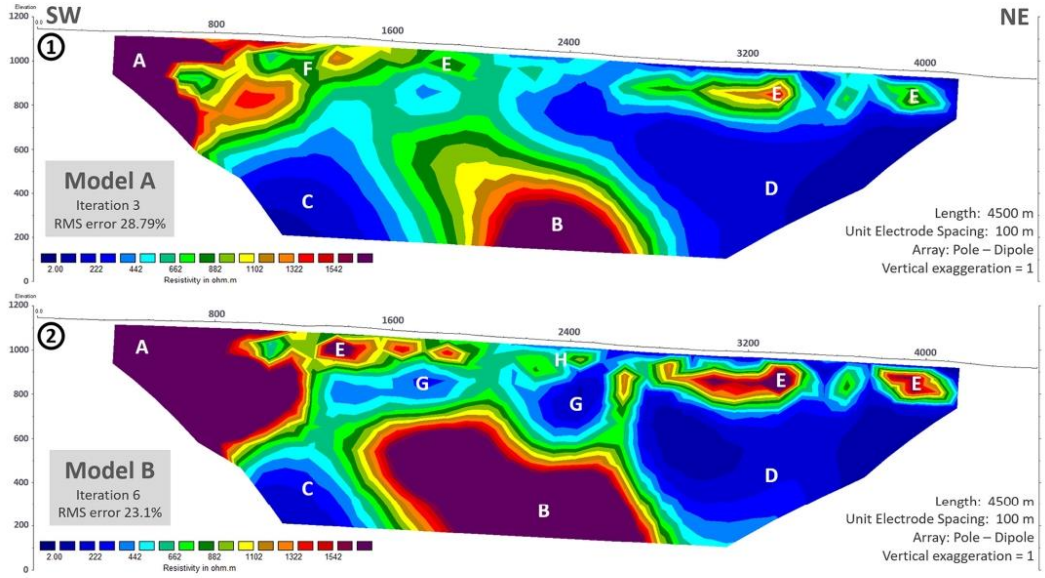

Fig. 5. (1) Model A (Iteration 3, RMS error 28.79%), (2) Model B (Iteration 6, RMS error 23.1%). A to G: resistive and conductive bodies delimited in the models.

The size and morphology of the resistive bodies (A and B) are larger and shows a higher resistivity gradient (> 500 Ohm•m/100 m) to the conductive zones than in model A, permitting the resistivity contrast limits of the anomalies to be established more precisely. The central resistive body (B) shows subvertical edges on its eastern and western sides. Resistive body B also presents a clear subvertical step discontinuity in its central part. Above the central discontinuity, a much clearer upper conductive area (G) is perceptible, which appears to be separate from some upper outcropping resistive layers (E and H). This horizontal outcropping resistivity layer shows a more continuous extent and can be differentiated into two types, in terms of resistivity value: E (more resistive) and H (less resistive). Comparing the main conductive zones, the conductive zone (C) in the southwest part of the model covers a smaller area than in model A.

5. Discussion

5.1. Model selection and validation

Geophysical inversion is inherently ill-posed and an infinite number of solutions are consistent with the observational data. Therefore, regularization is necessary to reduce the model space. Nevertheless, there still remains a variety of geologically acceptable models. Here, the results with external datasets to further reduce the model space are combined. The aim is to validate which geoelectrical model is more likely to represent the subsurface and at the same time provides a good fit to 1) the surface geology and lithostratigraphic units based on geological cartography of the Baza basin, 2) a qualitative correlation of the models A and B with geological and geophysical constraints, and3) the known Baza fault position and dip angles.

The IGME (Instituto Geologico y Minero de España) has produced 1:50,000 scale geological map of the study area. Based on this cartographic layer, the profile intersects few lithostratigraphic changes at the surface. Starting at the SW, Triassic substrata (basin basement rocks) crop out on the surface. These are covered by Plio-Quaternary glacis levels over Mio-Pliocene fluvio-lacustrine deposits over a short distance along the profile (Fig. 5).

Traces of the Baza Fault are obtained from Quaternary Active Faults Database of Iberia (QAFI). The QAFI database is a joint project between the Spanish Instituto Geológico y Minero de España (IGME) and the Portuguese Laboratório Nacional de Energia e Geologia (LNEG). QAFI provides the most up to date and authoritative inventory of active faults that affect Quaternary rocks and sediments. QAFI aims to capture the main faults displaying tectonic activity in the last 2.6 million years. All faults in the Baza fault zone present a 65° dip angle (Alfaro et al., 2008; Sanz de Galdeano et al., 2012; Haberland et al., 2017).

In addition to the geological information, the Baza Basin has been the subject of numerous geophysical studies to characterize its structure and infilling stratigraphy, including gravimetry and seismic reflection surveys (Figs. 2 and 6). Alfaro et al. (2008) conducted gravity gravity profiling studies covering the Baza Basin. The survey showed an asymmetric negative Bouguer anomaly close to the Baza fault with two gravity minima along the Basin axis running parallel along the fault strike. The Bouguer anomalies were interpreted as variations in the thickness of the basin infill. In the vicinity of DERT survey line, there are two gravimetric survey profile lines, named P2 and P3 in Alfaro et al. (2008) (Fig. 6). The two-dimensional models of the residual gravity anomaly registered on the P2 and P3 profiles provide evidence that the Baza Fault presents a clear half-graben geometry of the hanging wall, with an elongated trough bounded by the normal fault system. Line P-3 intersects the trace of the DERT survey line (Fig. 6) at its north-eastern end. The model used by Alfaro et al. (2008) suggested that at the resolution scale of the gravity data the Baza Fault is a single normal fault located to the East of the topographic range-front boundary, bounding the half-graben geometry and with a sedimentary filling thickness of 2400 m.

In 2013, high-resolution seismic profiles were used to image the basin, crossing the Baza Fault in different directions (Haberland et al., 2017). This seismic survey revealed an asymmetric basin shape bounded by Baza Fault, and several other buried faults in the East. Most of these

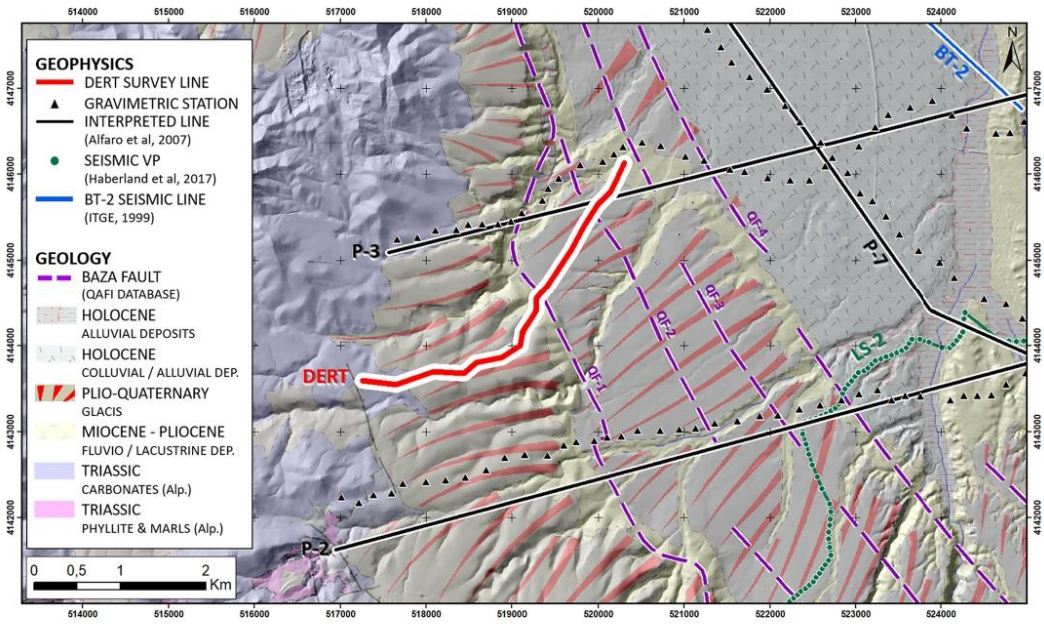

Fig. 6. Geological map of the study area based on 1:50.000 cartography (sheet 994, BAZA, Instituto Geológico y Minero de España (IGME), 1978), with location of the deep electrical resistivity survey line (red), Baza Fault main traces (QAFI database – dashed purple line) and geophysical surveys (black, blue and green dots and lines). (For interpretation of the references to colour in this figure legend, the reader is referred to the web version of this article.)

affect the deeper sedimentary layers of the Baza Basin. The basin was estimated to reach a maximum sediment thickness of 2200 m, in good agreement with the gravity models above (Alfaro et al., 2008). The closest seismic acquisition line to the deep electrical resistivity survey line was LS-2. However, it was still far away from it, so it was not possible to correlate it closely with the electrical resistivity models. Generally, it can only be analyzed in terms of structural style. Due to its long distance and different strike direction from the DERT line, the BT-2 seismic line was also not considered in discussion of the results. Analysis of relevant borehole survey profiles is dealt with in section 5.2.

Model A (Fig. 7-1) shows a good geoelectric correlation with surface outcropping materials, especially in the SW and central part of the model, with the presence of lateral resistivity changes between carbonates, glacis and fluvio-lacustrine materials.

The location and dip angles of two of the identified QAFI faults that were intersected (QF1 and QF2) are compared with the deep electrical resistivity model A. QF1 could be interpreted to continue at depth in the model because the lateral resistivity changes are related to a fault structure discernible in the upper and bottom parts of the model. However, the absence of a sharp resistivity contrast makes it difficult to precisely define its morphology and position. Model A suggests it is a structure with significant lateral displacement with respect to the cartographic position. Fault QF2 is barely identified in A. Weak resistivity with lateral loss of continuity was detected in the upper outcropping resistive sediments of the basin (Plio-Quaternary glacis), and hint at the presence of this fault.

Model A (Fig. 7-1) also correlates well with the IGME surface geology. In the Southwestern part of the model, high resistivity values coincide with the outcropping Triassic carbonate materials. In the central sector, Mio-Pliocene fluvio-lacustrine materials appear as a local resistivity decrease while the higher resistive values in the northeastern part of the model tend to coincide with the Plio-Quaternary glacis.

Although it may appear that the misfit to the data is similar, model B (Fig. 7-2) shows important variations from A, especially considering its correlation with fault information. The resistivity anomalies indicate that the QF1 fault may be located slightly to the West with respect to the QAFI surface trace location. This discrepancy could be due to a locally more complex fault gouge zone or multiple single fault strands like inferred faults 1 and 2 (Fig. 7-2), which cut the Triassic basement to the Northeast. This model shows that the anomalies associated with QF2 are more pronounced, with changes in lateral resistivity due to more resistive infillings among the shallower sediments in the basin. This should be interpreted as a strong indication of a discontinuity. This feature was less evident in model A. Model B correlates better with the outcropping materials, with well-defined lateral resistivity contrasts, especially between the Mio-Pliocene fluvio-lacustrine materials and Plio-Quaternary glacis in the central sector of the model.

5.2. *Model interpretation and implications for the Baza fault structure*

The electrical resistivity models A and B provide insights into the structure of the fault, in high spatial resolution from the surface down to around 1000 m depth. Both models show good agreement with the general structural geometry of the Baza Basin and a notable correlation with the lithostratigraphic units based on geological cartography. However, model B agrees more accurately with high-spatial resolution and low uncertainty information, such as the mapped surface lithostratigraphic units. Fig. 8 displays a geological interpretation of the preferred model B, including several inferred fault traces, named F1 to F6. Fig. 8 also shows the QAFI database fault positions (QF1 and QF2) and outcropping geological lithostratigraphic units.

The structural interpretation of the preferred model B (Fig. 8-1)

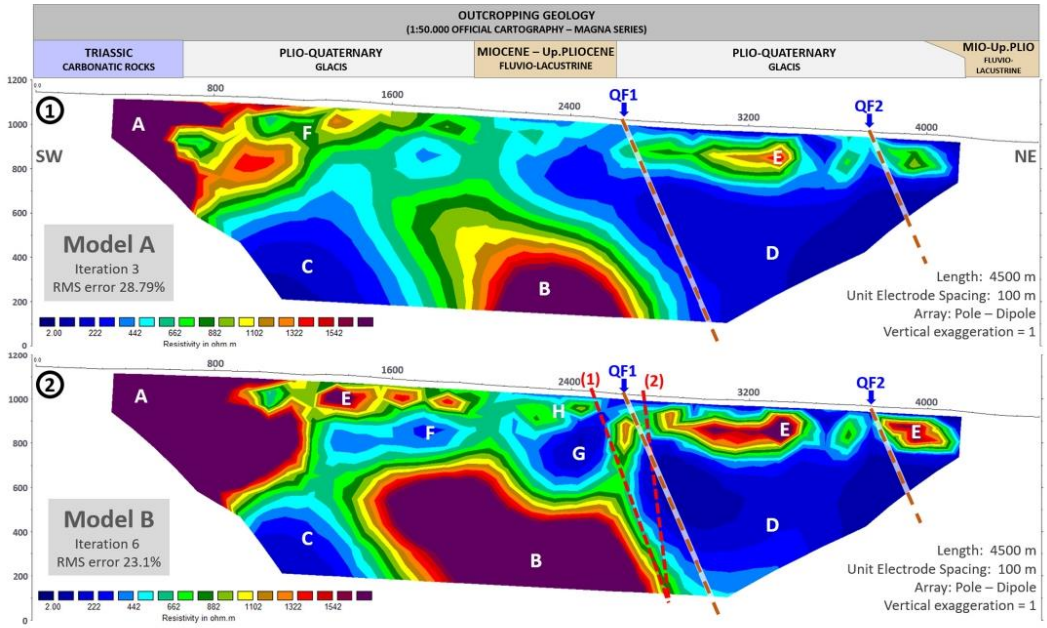

Fig. 7. (1) Model A; (2) Model B. Comparison with available data constraints, namely the outcropping geology (IGME cartography), location and dip angle from known fault traces (QAFI database). The fault plane dip angles were not inferred but taken from the reported 65° in the QAFI database.

shows evidence for up to six faults or structural discontinuities. All structures dip towards the NE, progressively rooting to the basement of the Baza Basin with a staircase morphology. Due to different amounts of inferred normal fault displacement and morphology expression, the faults were interpreted according to two criteria. Fault displacement was estimated using lateral resistivity variations with the assumption they correspond to lithological changes related to the former. This is especially clear in faults involving the variably resistive Triassic materials and conductive basin infillings, and between outcropping glacis levels and fluvio-lacustrine deposits. The first group includes the main inferred faults in terms of size and displacement, named F1, F2 and F3. This set of faults affect the lateral continuity of the resistive Triassic carbonate basement and also the basin infilling materials with a measurable vertical displacement of several hundred metres. The second set of faults, namely F4, F5 and F6, were only inferred by clear loss of lateral continuity of resistivity bodies in the upper infilling basin materials, particularly in the central and northeastern sections of the profile. Consequently, the interpretation of this second set of faults must be taken with caution, as their slip history is not constrained at all, but could provide a useful baseline for further studies.

Fault F1 is located in the western part of the profile and model, close to the 1200 m of the line. According to its morphology, it can be interpreted as a normal fault with a dip angle potentially varying from nearly vertical to 70° to the Northeast. This fault has accumulated a vertical throw, displacing the resistive Triassic basement at ≈ 350 ± 100 m. The fault plane of F1 changes its dip with depth, indicating a potential rotational tilting of the resistive Triassic basement rocks. This could indicate a listric fault geometry (Fig. 8). Based on high-resolution topographic information, the outcropping location coincides with the presence of a minor geomorphological alignment (Fig. 9). Such slope changes, perpendicular to the local drainage system, could be small escarpments compatible with the position and direction of slip along the fault plane. It is suggested that this location should be a target for future additional paleoseismic and/or detailed geological studies, as it affects recent geological deposits and may indicate an active structure.

F2 is also inferred by the rupture and observed vertical displacement of the resistive Triassic basement materials. This fault is clearly visible in the model as a lateral change in resistivity, also affecting the shallow resistive basin-infilling materials. The fault plane presents similar characteristics to F1, displacing the Triassic basement another 250 ± 100 m. The morphology of the basement between F1 and F2, showing a slight apparent dip to the west, indicates block rotation and the listric behavior of these faults. This is also observable in the shallow resistive basin-infilling materials between F1 and F2, indicated by a change in the thickness of the materials to the southwest.

These results are novel because to the best of our knowledge the F1 and F2 structures have not been previously identified. The position of these two new faults further west of the topographic range basin front boundary, and the QAFI fault QF1 position, permits displacement of the Baza Basin boundary by ≈ 1300 m to the west (Fig. 9).

Fault F3 is located in the central part of the model, close to the QF1 fault. This fault generated the largest displacement of the Triassic basement materials according to the preferred model B. The fault slip is unbounded but it must be larger than our maximum penetration depth of the DERT method (≈ 1 km). As commented previously, basal Triassic carbonates between F2 and F3 reveal a small apparent dip indicating a potential rotational structure, and suggest a shallow listric fault geometry.

F4, F5 and F6 were interpreted only on the basis of a lateral resistivity change in the upper outcropping resistive fillings of the basin, due to the absence of Triassic basement materials. According to the style observed in the previous faults, a normal-type representation was preferred. F4 seems to be a lesser feature associated with the main fault F3, which generates a local sinking of sedimentary infilling materials in

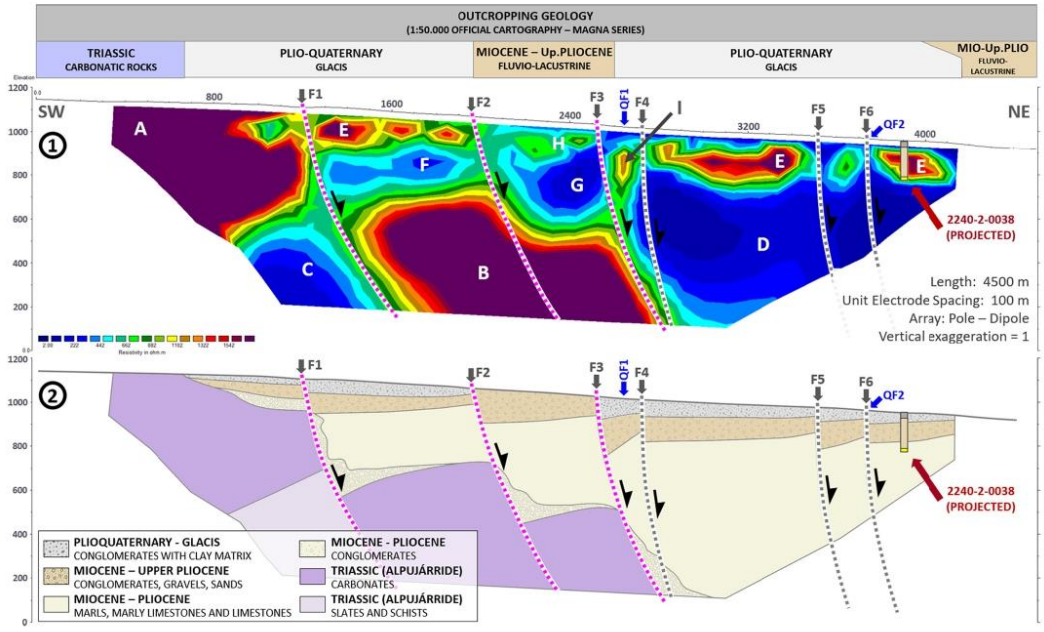

Fig. 8. 1) Structural interpretation of the deep electrical resistivity survey line, including several inferred faults. The F1 to F3 and F4 to F6 fault group were inferred using two different criteria. F1 to F3 are considered main faults, as they affect the Triassic basin basement and its infilling materials, with associated vertical fault displacement. F4 to F6 were inferred due to lateral resistivity changes detectable in the upper infilling basin materials with unknown slip history. QF1 and QF2: QAFI fault position. A to I: geoelectrical bodies discussed in the main text. 2) The preferred litho-stratigraphical interpretative model for the Baza Fault system in this sector, including the projected chrono-stratigraphical interpretation of borehole 2240–2-0038 at the NE end of the line.

the basin (I, Fig. 8-1).

QF2 fault trace intersected Model B in its eastern sector, close to the inferred position for fault F6. The geoelectrical model suggested that if the fault exists it has a small/short displacement history and should only involve materials of similar age and resistive properties. The local lateral resistivity change only affects the upper resistive materials where the F6 fault was interpreted.

In this study, the depth of investigation (DOI) index described by Oldenburg and Li (1999) was determined to assess reliability and to eliminate artefacts produced by mathematical inversion. The DOI index will be close to zero in areas where the final models are constrained well by the data, considering the inversion process to be reliable. However, cells with a DOI index greater than 0.2 were considered less reliable and therefore rejected (Oldenburg and Li, 1999; Thompson et al., 2012; Troiano et al., 2019) (Fig. 10).

This analysis (Fig. 10) shows how the unreliable zones do not affect the interpretation of the preferred geoelectric resistive model (Fig. 8-1 and -2), especially regarding the definition of the inferred fault zones. From the lithological point of view, the preferred resistivity model B shows how the high resistivity Triassic carbonate basement materials (A and B, Fig. 8-1) are strongly affected by the different splays of the Baza Fault. In the westernmost sector of the model, Triassic materials crop out up to the vicinity of F1, being progressively vertically displaced until fault F3, reaching the maximum depth sensitivity of the inversion model (> 1 km depth). Below the resistive Triassic carbonates ($\rho > 1500$ Ohm•m), a conductive area is discernable (C), probably related to Triassic phyllites, slates and calcschist (C), generating a clear resistivity in contrast with the upper carbonates (García Dueñas et al., 1992; Orozco and Alonso-Chaves, 2002).

In the central and northeastern part of the model and above the high-resistivity Triassic carbonates, conductive materials ($\rho < 400$ Ohm•m) belonging to the Miocene-Pliocene basin infilling sediments were detected (F, G and D). The resistivity of these materials is variable, but in general more conductive in the central deeper part of the basin (NE). The transition between resistive Triassic carbonates and conductive infillings is often gradual, indicating the presence of proximal breccias and conglomerates. These proximal sediments are especially noticeable close to the main faults, in concordance with deposition models of the basin.

More resistive materials ($\rho > 400$ Ohm•m) can be found in the shallower part of the profile (less than 300 m depth), which is associated with a higher granulometry of Miocene - upper Pliocene materials (E and H). These materials present lateral changes in resistivity that may be linked to fault discontinuities or local compositional rock variations. Glacis deposits are rarely observed in the profile because of their outcropping position and thickness. According to the cartographic data, glacis may have a maximum thickness of ≈50 m, coinciding with the loss of resolution of our model at shallow depths due to our minimum electrode spacing (≈100 m).

Fig. 8-2 shows a tectonic and litho-stratigraphic interpretation of our preferred geoelectrical model. According to this interpretation, the Baza Fault system could be a complex structure more than 2 km wide, with at least three and possibly six normal fault branches and a listric geometry. These faults affect the basin basement and infillings, indicating a long history of normal faulting displacement. The fault system generates an asymmetric segmentation with increasing basin thickness to the SW, clearly observable in the upper Miocene to Plio-Quaternary units. The results confirm that the fault should be active as present-day tectonic

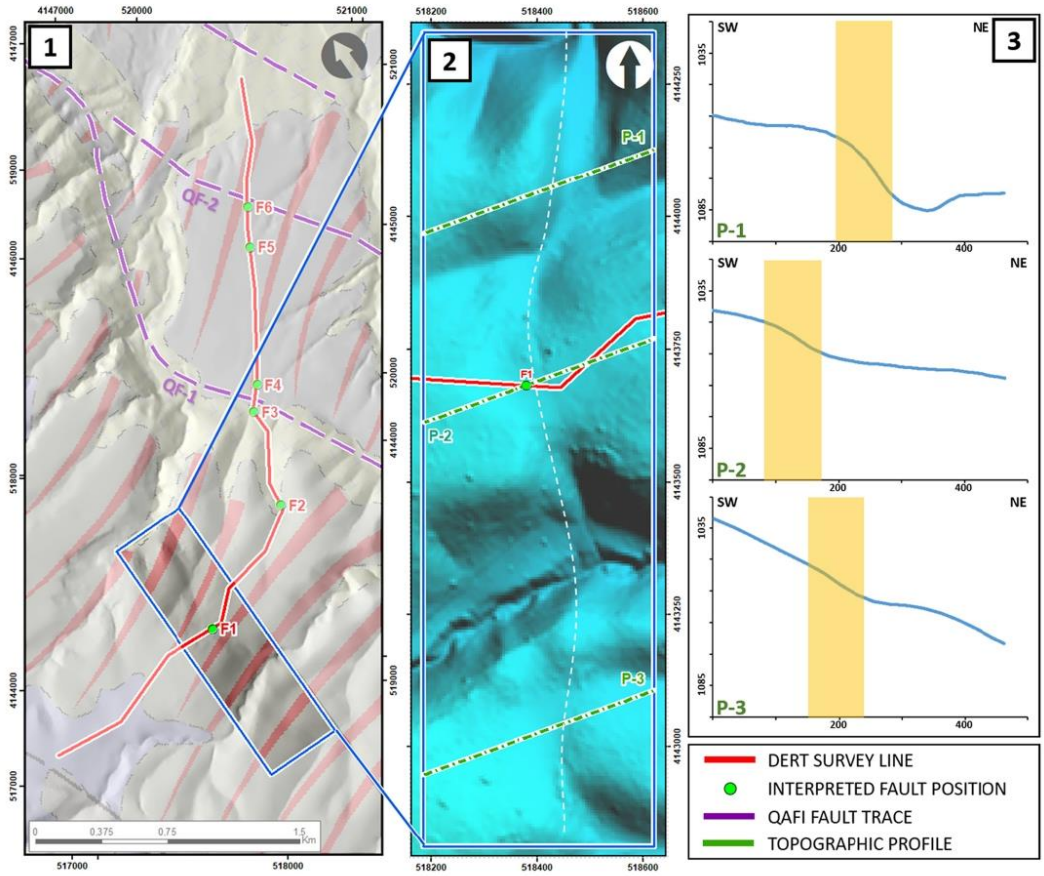

Fig. 9. Topographic analysis of fault F1. 1) Deep electrical resistivity survey line position, with inferred fault positions (F1 to F6), QAFI fault traces and topographic analysis area (blue rectangle). 2) Hillshade representation of the analysis area topography showing position of the interpreted F1 fault, deep electrical resistivity survey line, and topography analysis profiles (P-1 to P-3). The white dashed line represents a potential alineation of the F1 fault. 3) Topographic analysis profiles P-1, P-2 and P-3 showing escarpments (orange areas) compatible with a fault. (For interpretation of the references to colour in this figure legend, the reader is referred to the web version of this article.)

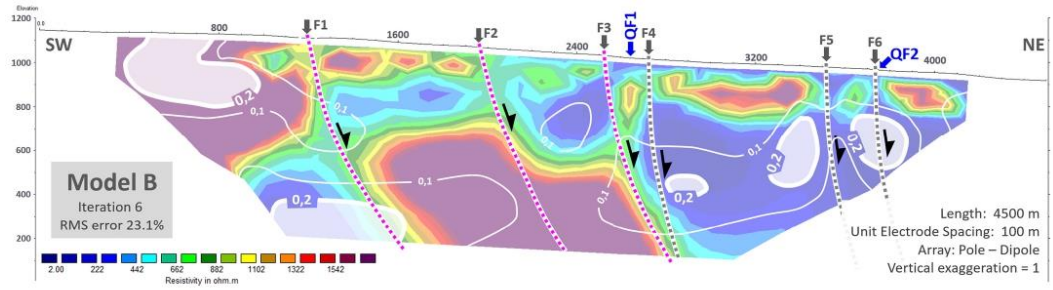

Fig. 10. Depth of Investigation Index (DOI) of the resistivity model. Cells with DOI index greater than 0.2 are considered less reliable. This figure shows how the obtained DOIN index do not affect the structural interpretation of the model (Fig. 8).

faults due to the fact that they are cutting through all the sedimentary materials, including glacis Plio-Quaternary levels. This is particularly the case of the previously unrecognized fault F1, which has geomorphic expression (5–10 m) (Fig. 11).

In this study, public databases of boreholes (lithologic or geophysical core drilling) in the vicinity of the line of investigation were consulted for better interpretation. According to the lithological scheme available, the 2240–2-0038 code borehole reached a depth of 185 m. The column shows a complex lithological succession with alternation of conglomerates, sands, marls, silts and clays. Unfortunately, there are no chronostratigraphic differentiations in the public database. Moreover, a tentative analysis of that column suggests an increase in clay content from 141 to 173 m, which could be interpreted as a change in sedimentation regime. This change may reflect a different age, possibly the transition between Plio-Quaternary and upper Mio-Pliocene materials to lower Mio-Pliocene materials, with a mainly marly character (Fig. 12-2). However, a precise interpretation was not possible without further geological analysis.

Borehole 2240–2-0038 can be projected at around 3800–4000 m of the profile, taking into account the structure of the study area and position of the main faults. The interpretation of the borehole was analyzed by the geoelectric resistive model and its geological interpretation (Figs. 8-1 and -2). Overall, a correspondence was observed between the borehole geology and the geoelectric model (Fig. 8), but there were significant divergences in the thickness of the stratigraphic layers. These differences are to be expected, owing to the uncertainty of the borehole location with respect to the profile and spatial resolution of the inverted model.

6. Conclusions

This study presents the new results of a deep electrical resistivity tomography (DERT) study to gain insights into the shallow geometry of the Baza Fault system. The DERT model is sensitive to structures with depth ranges complementary to previous gravity and seismic and surface geology. Specifically, this investigation was conducted in the southwestern part of the Baza Basin. Resistivity data were obtained using two 3 km long multicore reversible cables with electrode spacing of 100 m to allow a depth penetration of more than 1 km. The inversion models are in good agreement with geological and geophysical constraints. The preferred resistivity model presents resistivity values ranging from 20 to 3000 Ohm•m, which were calibrated with the lithostratigraphic characteristics and fault database position (QAFI). A new, more detailed geological and structural view of the Baza Fault is provided.

The results strongly support that the main strand of the system is the fault here named F3, close to the known QF1 mapped in the QAFI database. This F3/QF1 structure progressively plunges the Triassic basement below the maximum penetration depth of the DERT method (indicating a cumulative slip history of >1 km). The new model furnishes higher-spatial resolution information at depth for the Baza fault system, and supports a segmented active normal fault system, considerably wider than previously recognized (> 2 km wide). This study confirms that, as in previous studies, the Baza fault system consist of northeast dipping normal faults controlling the basin's development and structure. The inferred structures suggest progressive change in dip angle with depth, supporting listric fault geometries.

A fault system located southwestward of QF1 emerges with this study. A previously unmapped fault (F1) with significant accumulated slip, located west from previous known faults and hence representing a major basin-bounding fault (1300 m southwestward of QF1) was determined. F2 is another unmapped fault located between (F1) and (QF1), inferred by the rupture and observed vertical displacement of the resistive Triassic basement materials. In addition, there is geophysical, and possible geomorphic, evidence suggesting that F1 is an active fault affecting the youngest Plio-Quaternary glacis levels. It is expected that these new results will motivate future paleoseismologic studies on this candidate fault(s).

Our study has revealed that the deep electrical resistivity research method can be an important tool to study active fault systems, such as Baza. It is thought that the method applied in this study will be a complementary method in regional gravity and seismic surveys and detailed geological mapping. The results from deep electrical resistivity models can improve the identification of seismogenic active faults.

Authors statement

We, the authors, declare that this material is new and has not been

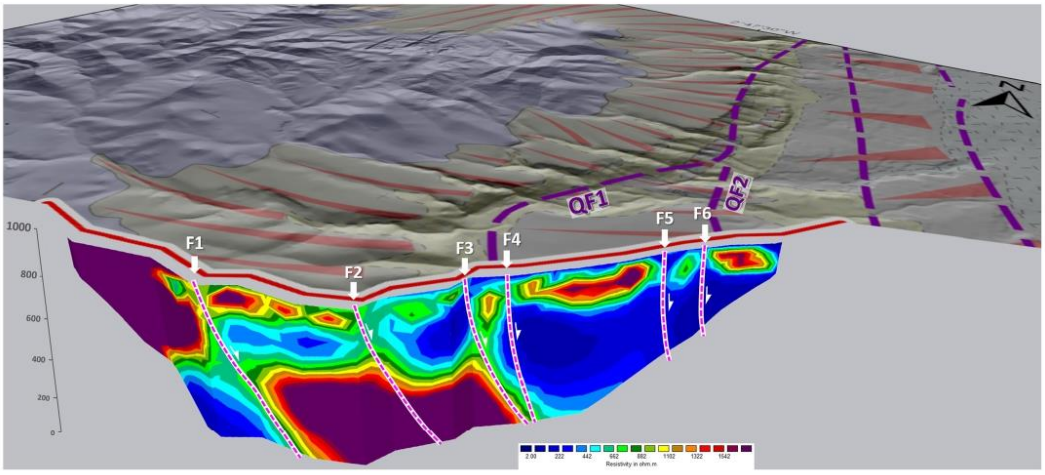

Fig. 11. 3D sketch showing the fault interpretation along the deep electrical resistivity tomography (DERT) survey line with geological cartography and fault traces according to the Quaternary Active Faults Database of Iberia (QAFI). The presence of new faults F1 and F2, and conductive infilling materials, shows a western position of the Baza Basin limit.

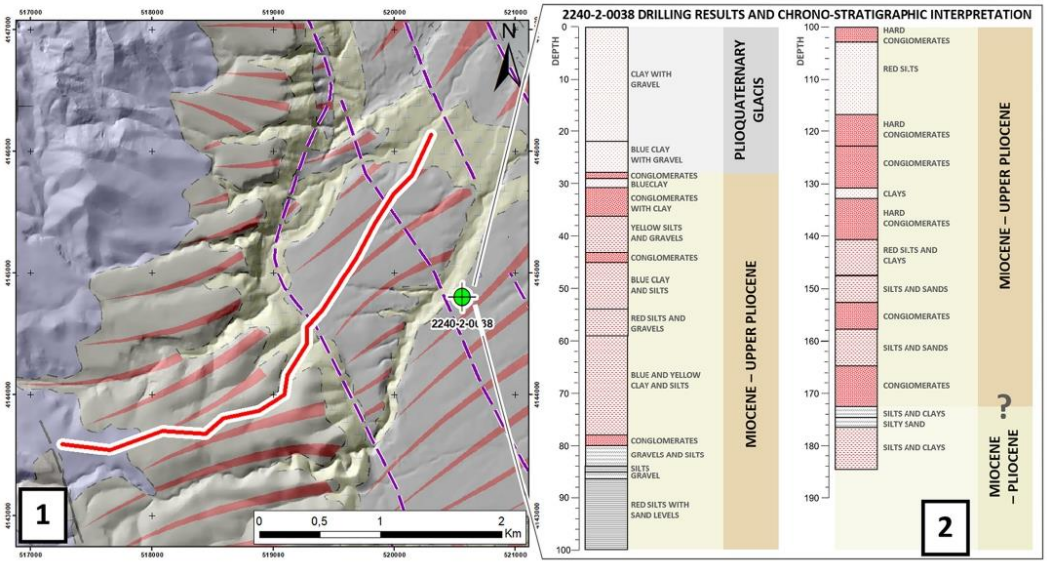

Fig. 12. 1) Geological map of the study area based on 1:50.000 cartography (sheet 994, BAZA, Instituto Geológico y Minero de España (IGME), 1978), with location of the deep electrical resistivity (DERT) survey line (red), Baza Fault main fault traces (QAFI database – dashed purple line), geophysical surveys (black, blue and green dots and lines), and boreholes with lithological information (Instituto Geológico y Minero de España, Base de datos de puntos de agua (http://info.igme.es/BDAguas/), SIGEOF, Sistema de informacion Geofísica (http://info.igme.es/sigeof/) and Litoteca de sondeos (http://www.igme.es/servicios/litoteca.htm)). 2) Lithological scheme of borehole 2240–2-0038, located 950 m to the SE of the survey line, and a tentative chrono-stratigraphic interpretation. (For interpretation of the references to colour in this figure legend, the reader is referred to the web version of this article.)

submitted to any other journal.

Declaration of Competing Interest

We, the authors, declare that we do not have any conflict of interest regarding the content of the manuscript submitted to Journal of Applied Geophysics.

Acknowledgments

The project was funded by GEOLAND SERVICES SL and Técnicas Geofísicas SL. The authors appreciate the assistance of anonymous reviewers for their comments and support on this paper, especially professor D. Pedro Carrasco Morillo. Without his vision this work would not have been possible. This manuscript has been edited by Guido Jones, currently funded by the Cabildo de Tenerife, under the TFinnova Programme supported by MEDI and FDCAN funds. PJG's contribution was supported by the Spanish Ministerio de Ciencia e Innovación research project COMPACT (proyecto PID2019-104571RA-I00 de investigación financiado por MCIN/AEI/10.13039/501100011033) and a 2020 Leonardo Fellowship Grant for Researchers and Cultural Creators, BBVA Foundation (IN[20]_CMA_CCT_0015).

References

Alfaro, P., Moretti, M., Soria, J.M., 1997. Soft-sediment deformation structures induced by earthquakes (seismites) in Pliocenelacustrine deposits (Guadix-Baza Basin, Central Betic Cordillera). Eclogae Geol. Helv. 90, 531–540. https://doi.org/10.5169/seals-168193.

Alfaro, P., Delgado, J., Sanz de Galdeano, C., Galindo Zaldívar, J., García-Tortosa, F.J., López-Garrido, A.C., López-Casado, C., Marín-Lechado, A., Gil, A., Borque, M.J., 2008. The Baza Fault: a major active extensional fault in the central Betic Cordillera (south Spain). Int. J. Earth Sci. 97, 1353–1365. https://doi.org/10.1007/s00531-007-0213-z.

Balasco, M., Galli, P., Giocoli, A., Gueguen, E., Lapenna, V., Perrone, A., Iscitelli, S.P., Rizzo, E., Romano, G., Siniscalchi, A., Votta, M., 2011. Deep geophysical electromagnetic section across the middle Aterno Valley (Central Italy): preliminary results after the April 6, 2009 L'Aquila earthquake. Boll. Geofis. Teor. Appl. 52 (3), 443–455. https://doi.org/10.4430/bgta0028.

Biasi, G., Wesnousky, S., 2017. Bends and ends of surface ruptures. Bull. Seismol. Soc. Am. 107, 2543–2560. https://doi.org/10.1785/0120160292.

Caputo, R., Piscitelli, S., Oliveto, A., Rizzo, E., Lapenna, V., 2003. High-resolution resistivity tomographies in active tectonic studies. Examples from the Tyrnavos Basin, Greece. J. Geod. 36 (1–2), 19–35. https://doi.org/10.1016/S0264-3707(03)00036-X.

Carrasco García, P., 2013. Avance en Técnicas Geofísicas para la caracterización del subsuelo mediante innovación y el uso de herramientas de gestión de información espacial. PhD Thesis. Escuela Politécnica Superior de Avila. Univ de Salamanca, 523 pp.

Carrier, A., Fischanger, F., Gance, J., Cocchiararo, G., Morelli, G., Lupi, M., 2019. Deep electrical resistivity tomography for the prospection of low-to medium enthalpy geothermal resources. Geophys. J. Int. 219, 2056–2072. https://doi.org/10.1093/gji/ggz411.

Castro, J., Martin-Rojas, I., Medina-Cascales, I., García-Tortosa, F.J., Alfaro, P., Insua-Arévalo, J.M., 2018. Active faulting in the central Betic Cordillera (Spain): palaeoseismological constraint of the surface-rupturing history of the Baza Fault (Central Betic Cordillera, Iberian Peninsula). Tectonophysics 736, 15–30. https://doi.org/10.1016/j.tecto.2018.04.010.

Drahor, M.G., Berge, M.A., 2017. Integrated Geophysical Investigations in A Fault Zone located on Southwestern part of Izmir City, Western Anatolia, Turkey. J. Appl. Geophys. 136, 114–133. https://doi.org/10.1016/j.jappgeo.2016.10.021.

Edwards, L.S., 1977. A modified pseudosection for resistivity and IP. Geophysics 42, 1020–1036. https://doi.org/10.1190/1.1440762.

Galindo Zaldívar, J., González-Lodeiro, F., Jabaloy, A., 1989. Progressive extensional shear structures in a detachment contact in the Western Sierra Nevada (Betic Cordilleras, Spain). Geodin. Acta 3 (1), 73–85. https://doi.org/10.1080/09853111.1989.11105175.

Galindo Zaldívar, J., Jabaloy, A., Serrano, I., Morales, J., González- Lodeiro, F., Torcal, F., 1999. Recent and present-day stresses in the Granada Basin (Betic Cordilleras): example of a late Miocene-present-day extensional basin in a convergent plate boundary. Tectonics 18 (4), 686–702. https://doi.org/10.1029/1999TC900016.

García Tortosa, F.J., Alfaro, P., Galindo Zaldívar, J., Gibert, L., López Garrido, A.C., Sanz de Galdeano, C., Ureña, M., 2008. Geomorphologic evidence of the active Baza Fault

(Betic Cordillera, South Spain). Geomorphology 97 (3–4), 374–391. https://doi.org/10.1016/j.geomorph.2007.08.007.
García Tortosa, F.J., Alfaro, P., Galindo Zaldívar, J., Sanz de Galdeano, C., 2011. Glacis geometry as a geomorphic marker of recent tectonics: the Guadix-Baza Basin (South Spain). Geomorphology 125 (4), 517–529. https://doi.org/10.1016/j.geomorph.2010.10.021.
García-Dueñas, V., Balanyá, J.C., Martínez-Martínez, J.M., 1992. Miocene extensional detachments in the outcropping basement of the northern Alboran Basin (Betics) and their tectonic implications. Geo-Marine Lett. 12, 88–95. https://doi.org/10.1007/BF02084917.
García-Dueñas, V., Banda, E., Torné, M., Cordoba, D., ESCI-Béticas Working Group, 1994. A deep seismic reflection survey across the Betic Chain (Southern Spain): first results. Tectonophysics 232, 77–89. https://doi.org/10.1016/0040-1951(94)90077-9.
García-García, F., Fernández, J., Viseras, C., Soria, J.M., 2006. Architecture and sedimentary facies evolution in a delta stack controlled by fault growth (Betic Cordillera, southern Spain, late Tortonian). Sediment. Geol. 185 (1–2), 79–92. https://doi.org/10.1016/j.sedgeo.2005.10.010.
Gibert, L., Sanz de Galdeano, C., Alfaro, P., López Garrido, A.C., 2005. Seismic-induced slump in early Pleistocene deltaic deposits of the Baza Basin (SE Spain). Sediment. Geol. 179 (3), 279–294. https://doi.org/10.1016/j.sedgeo.2005.06.003.
Günther, Thomas, Schaumann, Gerlinde, Musmann, Patrick, Grinat, Michael, 2011. Imaging of a Fault Zone by a Large-scale DC Resistivity Experiment and Seismic Structural Information. https://doi.org/10.3997/2214-4609.20144450.
Haberland, C., Giber, L., Jurado, M.J., Stiller, M., Baumann- Wilke, M., Scott, G., Mertz, D.F., 2017. Architecture and tectono-stratigraphic evolution of the intramontane Baza Basin (Betics, SE-Spain): constraints from seismic imaging. Tectonophysics 709, 69–84. https://doi.org/10.1016/j.tecto.2017.03.022.
IGN (Spanish Instituto Geográfico nacional) seismic Catalogue, 2020. https://www.ign.es/web/sis-catalogo-terremotos.
Instituto Geológico y Minero de España (IGME), 1978. Mapa geológico de la hoja n° 994 (Baza Hoja de Baza 994). Mapa Geológico de España E. 1:50.000. Segunda Serie (MAGNA), Primera edición. IGME. Depósito legal: M-6791-1978.
Jabaloy, A., Galindo Zaldivar, J., Gonzalez-Lodeiro, F., Aldaya, F., 1995. Main features of the deep structure of the central Betic Cordillera (SE Spain) from the ESCI-Béticas deep seismic reflection profiles. Rev. Soc. Geol. Esp. 8 (4), 461–476.
Kolawole, F., Atekwana, E.A., Laó-Dávila, D.A., Abdelsalam, M.G., Chindandali, P.R., Salima, J., Kalindekafe, L., 2018. High-resolution electrical resistivity and aeromagnetic imaging reveal the causative fault of the 2009 M_w 6.0 Karonga, Malawi earthquake. Geophys. J. Int. 213 (2), 1412–1425. https://doi.org/10.1093/gji/ggy066.
Lines, L.R., Treitel, S., 1984. Tutorial: a review of least-squares inversion and its application to geophysical problems. Geophys. Prospect. 32, 159–186. https://doi.org/10.1111/j.1365-2478.1984.tb00726.x.
Loke, M.H., 2019. Rapid 2-D Resistivity and IP inversión Using the Least-Squares Method. Geotomo Software, Malaysia, 146 pp.
Loke, M.H., Barker, R.D., 1995. Least-square inversion of apparent resistivity pseudosections. Geophysics 60, 1682–1690. https://doi.org/10.1190/1.1443900.
Loke, M., Dahlin, T., 2002. A comparison of the Gauss–Newton and quasi-Newton methods in resistivity imaging inversion. J. Appl. Geophys. 49 (3), 149–162. https://doi.org/10.1016/S0926-9851(01)00106-9.
Marín-Lechado, C., Pedrera, A., Peláez, J.A., Ruiz-Constán, A., González-Ramón, A., Henares, J., 2017. Deformation style and controlling geodynamic processes at the eastern Guadalquivir foreland basin (Southern Spain). Tectonics 36, 1072–1089. https://doi.org/10.1002/2017TC004556.
Martínez-Solares, J.M., Mezcua, J., 2002. Catálogo sísmico de la Península Ibérica (880 AC-1900). Madrid (Spain), Instituto Geográfico Nacional (IGN). Monografía 18, 254 pp.
Medina-Cascales, I., Martin-Rojas, I., García-Tortosa, F.J., Peláez, J.A., Alfaro, P., 2020. Geometry and kinematics of the Baza Fault (central Betic Cordillera, South Spain): insights into its seismic potential. Geol. Acta 18 (11), 1–25. https://doi.org/10.1344/GeologicaActa2020.18.11.
Nocquet, J.-M., 2012. Present-day kinematics of the Mediterranean: A comprehensive overview of GPS results. Tectonophysics 579, 220–242. https://doi.org/10.1016/j.tecto.2012.03.037.
Oldenburg, D.W., Li, Y., 1999. Estimating depth of investigation in DC resistivity and IP surveys. Geophysics 64, 403–416. https://doi.org/10.1190/1.1444545.
Orozco, M., Alonso-Chaves, F.M., 2002. Estructuras de colapso extensional en el Dominio de Alborán. In: Orozco, M. (Ed.), Región de La Axarquía-Sierra Tejeda (provincias de Málaga y Granada). XIV Reunión de la Comisión de Tectónica de la Sociedad Geológica de España, Guía de Campo, Granada, 120pp. ISBN: 84-607-5712-9.
Pace, B., Visini, F., Peruzza, L., 2016. FiSH: MATLAB tools to turn fault data into Seismic-Hazard Models. Seismol. Res. Lett. 87 (2A), 374–386. https://doi.org/10.1785/0220150189.
Palano, M., González, P.J., Fernández, J., 2013. Strain and stress fields along the Gibraltar Orogenic Arc: Constraints on active geodynamics. Gondwana Res. 23 (3), 1071–1088. https://doi.org/10.1016/j.gr.2012.05.021.
Palano, M., González, P.J., Fernández, J., 2015. The Diffuse Plate boundary of Nubia and Iberia in the Western Mediterranean: Crustal deformation evidence for viscous coupling and fragmented lithosphere. Earth Planet. Sci. Lett. 430, 439–447. https://doi.org/10.1016/j.epsl.2015.08.040.
Pérez-Peña, J.V., Azañón, J.M., Galve, J.P., Booth-Rea, G., de Lis Mancilla, F., Stich, D., Morales, J., 2018. A post-Tortonian pull-apart basin controlled by lithosphere tearing processes at a STEP boundary of the Gibraltar Arc Subduction System. In: 20th EGU General Assembly, EGU2018, Proceedings from the Conference held 4-13 April, 2018 in Vienna, Austria, p. 15695. https://ui.adsabs.harvard.edu/abs/2018EGUGA..2015695P/abstract.
Pucci, S., Finizola, S., Civico, R., Sapia, V., Barde-Cabusson, S., Orefice, S., Peltier, A., Villani, F., Ricci, T., De Martini, P.M., Brothelande, E., Poret, M., Gusset, R., Torres, L., Delcher, E., Daniela, Pantosti, Mezon, C., Suski, B., 2016. Deep electrical resistivity tomography along the tectonically active Middle Aterno Valley (2009 L'Aquila earthquake area, Central Italy). Geophys. J. Int. 207 (2), 967–982. https://doi.org/10.1093/gji/ggw308.
Rizzo, E., Giamapolo, V., 2019. New deep electrical resistivity tomography in the High Agri Valley basin (Basilicata, Southern Italy). Geomat. Nat. Hazards Risk 10 (1), 197–218. https://doi.org/10.1080/19475705.2018.1520150.
Rizzo, E., Colella, A., Lapenna, V., Piscitelli, S., 2004. High-resolution images of the fault-controlled High Agri Valley basin (Southern Italy) with deep and shallow electrical resistivity tomographies. Phys. Chem. Earth 29, 321–327. https://doi.org/10.1016/j.pce.2003.12.002.
Rizzo, E., Giampaolo, V., Capozzoli, L., Grimaldi, S., 2019. Deep Electrical Resistivity Tomography for the Hydrogeological setting of Muro Lucano Mounts Aquifer (Basilicata, Southern Italy). Geofluids 2019, 6594983. https://doi.org/10.1155/2019/6594983.
Robain, H., Bobachev, A., 2002. X2IPI Tool Box for 2D DCand DC-IP Measurements. http://geophys.geol.msu.ru/x2ipi/x2ipi.html#boba.
Rodríguez-Fernandez, J., Azor, A., Azañón, J., 2012. The betic intramontane basins (SE Spain): stratigraphy, subsidence, and tectonic history. In: Tectonics of Sedimentary Basins, pp. 461–479. https://doi.org/10.1002/9781444347166.ch23.
Sanz de Galdeano, C., Vera, J.A., 1992. Stratigraphic record and palaeogeographical context of the Neogene basins in the Betic Cordillera, Spain. Basin Res. 4 (1), 21–36. https://doi.org/10.1111/j.1365-2117.1992.tb00040.x.
Sanz de Galdeano, C., Vera, J.A., 2007. Stratigraphic record and palaeogeographical context of the Neogene basins in the Betic Cordillera, Spain. Basin Res. 4, 21–36. https://doi.org/10.1111/j.1365-2117.1992.tb00040.x.
Sanz de Galdeano, C., García-Tortosa, F.J., Peláez, J.A., Alfaro, P., Azañón, J.M., Galindo Zaldívar, J., López-Casado, C., López- Garrido, A.C., Rodríguez-Fernández, J., Ruano, P., 2012. Main active faults in the Granada and Guadix-Baza Basins (Betic Cordillera). J. Iber. Geol. 38 (1), 209–223. https://doi.org/10.5209/rev_JIGE.2012.v38.n1.39215.
Sanz de Galdeano, C., Azañón, J.M., Cabral, J., Ruano, P., Alfaro, P., Canora, C., Ferrater, M., García-Tortosa, F., Mayordomo, J., Gràcia, E., Insua-Arévalo, J.M., Jiménez, A., Lacan, P., Marín-Lechado, C., Martín-Banda, R., Martín-González, F., Martínez-Díaz, J.J., Martín-Rojas, I., Masana, E., Simón, J.L., 2020. Active faults in Iberia. In: Quesada, C., Oliveira, J. (Eds.), The Geology of Iberia: A Geodynamic Approach. Springer, Cham, Regional Geology Reviews, pp. 33–75.
Scholz, C.H., 2019. The Mechanics of Earthquakes and Faulting, 3rd edition. Cambridge University Press, Cambridge. 493pp.
Soria, J.M., Viseras, C., Fernandez, J., 1998. Late Miocene–Pleistocene tectono-sedimentary evolution and subsidence history of the central Betic Cordillera (Spain): A case study in the Guadix intramontane basin. Geol. Mag. 135 (4), 565–574. https://doi.org/10.1017/S0016756898001186.
Steeples, D.W., 2001. Engineering and environmental geophysics at the millenium. Geophysics. 66 (1), 31–35. https://doi.org/10.1190/1.1444910.
Storz, H., Storz, W., Jacobs, F., 2000. Electrical resistivity tomography to investigate geological structures of the earth's upper crust. Geophys. Prospect. 48, 455–471. https://doi.org/10.1046/j.1365-2478.2000.00196.x.
Suzuki, K., Toda, S., Kusunoki, K., Fujimitsu, Y., Mogi, T., Jomori, A., 2000. Case studies of electrical and electromagnetic methods applied to mapping active faults beneath the thick quaternary. Dev. Geotech. Eng. 84, 29–45. https://doi.org/10.1016/S0165-1250(00)80005-X.
Telford, W.M., Geldart, L.P., Sheriff, R.E., 1990. Applied Geophysics, 2nd ed. Cambridge Univ. Press, Cambridge, UK. https://doi.org/10.1017/CBO9781139167932.
Thompson, S., Kulssa, B., Luckman, A., 2012. Integrated electrical resistivity tomography (ERT) and self-potential (SP) techniques for assessing hydrological processes within glacial lake moraine dams. J. Glaciol. 58 (211), 849–858. https://doi.org/10.3189/2012JoG11J235.
Troiano, A., Isaia, R., Di Giuseppe, M.G., Tramparulo, D.A., Vitale, S., 2019. Deep electrical resistivity tomography for a 3D picture of the most active sector of Campi Flegrei caldera. Sci. Rep. 9, 15124. https://doi.org/10.1038/s41598-019-51568-0.
Vera, J.A., 1970a. Facies del Plioceno de la Depresión de Guadix- Baza. Cuadernos Geol. Univ. Granada 1, 23–25.
Vera, J.A., 1970b. Estudio estratigráfico de la Depresión de Guadix-Baza. Boletín Inst. Geol. Miner. Esp. 81, 429–462.
Wells, D.L., Coppersmith, K.J., 1994. New empirical relationships among magnitude, rupture length, rupture width, rupture area, and surface displacement. Bull. Seismol. Soc. Am. 84 (4), 974–1002. https://doi.org/10.1785/BSSA0840040974.
Wesnousky, S.G., 2008. Displacement and geometrical characteristics of earthquake surface ruptures: issues and implications for seismic-hazard analysis and the process of earthquake rupture. Bull. Seismol. Soc. Am. 98 (4), 1609–1632. https://doi.org/10.1785/0120070111.

ARTICULO 2 Drone Magnetometry in Mining Research. An Application in the Study of Triassic Cu–Co–Ni Mineralizations in the Estancias Mountain Range, Almería (Spain)

Resumen:

El uso de drones en la exploración geológica y minera está experimentando un rápido desarrollo, especialmente en el campo de la prospección magnética, gracias a las ventajas que ofrece frente a los levantamientos terrestres tradicionales al permitir una elevada densidad de toma de datos con una muy baja perdida de resolución, siendo, además, una herramienta útil en determinados escenarios donde la vegetación, topografía y el acceso son factores limitantes.

En este trabajo se analizan los resultados de una prospección magnética con drone adquirida sobre las antiguas labores de la mina de Don Jacobo, donde se explotaba una mineralización estratoligada de Cu-Co-Ni en la Sierra de las Estancias, Cordillera Bética (España).

Los trabajos de investigación se han llevado a cabo empleando un magnetómetro de vapor de cesio instalado sobre un hexacóptero Matrice 600 Pro. Se han adquirido un total de veinticuatro líneas paralelas entre sí y orientadas ortogonalmente a la estructura geológica regional con una velocidad de vuelo de 5 m / s., 50 m de separación lateral y 20 m de elevación sobre el suelo. La interpretación de los datos magnéticos permite determinar y modelar dos cuerpos de alta susceptibilidad magnética con magnetización residual, próximos a las antiguas labores mineras y muestras con mineralización en afloramientos. Estos cuerpos podrían estar relacionados con potenciales zonas mineralizadas no explotadas cuya formación podría estar relacionada con una falla normal situada al sur de la zona de prospección.

El estudio geofísico proporciona datos esenciales para mejorar el potencial geológico y minero de la zona, permitiendo diseñar futuras actividades de investigación.

.

drones

MDPI

Article

Drone Magnetometry in Mining Research. An Application in the Study of Triassic Cu–Co–Ni Mineralizations in the Estancias Mountain Range, Almería (Spain)

Daniel Porras [1], Javier Carrasco [2], Pedro Carrasco [3], Santiago Alfageme [4], Diego Gonzalez-Aguilera [3,*] and Rafael Lopez Guijarro [5]

[1] Geoland Services S.L., 28008 Madrid, Spain; dporras@geoland.es
[2] Técnicas Geofísicas S.L., 05003 Avila, Spain; tgeofisicas@gmail.com
[3] Departamento Ingeniería Cartográfica y del Terreno Geología, Escuela Politécnica Superior de Ávila, Universidad de Salamanca, Avd. Hornos Caleros 50, 05003 Avila, Spain; retep81@usal.es
[4] Gesminle S.L., 24001 Leon, Spain; sca@gesminle.es
[5] Exco Mining S.L., 28008 Madrid, Spain; rlopez@excomining.es
* Correspondence: daguilera@usal.es; Tel.: +34-920353500

Abstract: The use of drones in mining and geological exploration is under rapid development, especially in the field of magnetic field prospection. In part, this is related to the advantages presented for over ground surveys, allowing for high-density data acquisition with low loss of resolution, while being particularly useful in scenarios where vegetation, topography, and access are limiting factors. This work analyzes results of a drone magnetic survey acquired across the old mines of Don Jacobo, where Copper-Cobalt-Nickel stratabound mineralizations were exploited in the Estancias mountain range of the Betic Cordillera, Spain. The survey carried out used a vapor magnetometer installed on a Matrice 600 Pro Hexacopter. Twenty-four parallel survey lines were flown with a speed of 5 m/s, orthogonal to the regional strike of the geological structure, and mineralization with 50 m line separation and 20 m flight height over the ground was studied. The interpretation of the magnetic data allows us to reveal and model two high magnetic susceptibility bodies with residual magnetization, close to the old mines and surface mineral shows. These bodies could be related to potential unexploited mineralized areas whose formation may be related to a normal fault placed to the south of the survey area. Our geophysical survey provides essential data to improve the geological and mining potential of the area, allowing to design future research activities.

Keywords: aeromagnetics; drone survey; mineral exploration; geophysical prospecting

Citation: Porras, D.; Carrasco, J.; Carrasco, P.; Alfageme, S.; Gonzalez-Aguilera, D.; Lopez Guijarro, R. Drone Magnetometry in Mining Research. An Application in the Study of Triassic Cu–Co–Ni Mineralizations in the Estancias Mountain Range, Almería (Spain). *Drones* **2021**, *5*, 151. https://doi.org/10.3390/drones5040151

Academic Editor: Giordano Teza

Received: 19 October 2021
Accepted: 14 December 2021
Published: 18 December 2021

1. Introduction

The demand for raw materials is rapidly increasing, proving a fundamental pillar in modern development as well as the future prospects of European industries. The product of this is a rise in demand for new material extraction sites that are able to support this type of development. In the case of Europe, geological and mining research is currently hindered by the effectiveness and speed of traditional methodologies in this type of research. This has resulted in adaptations in the field of geophysics in response to increasingly stricter requirements.

In this context, the use of drones is under important development, incorporating more autonomous systems allowing for the integration of multiple sensors such as: RGB sensors, ultrasonic sensors, Infrared Sensors (IR), stereo camera, laser range finders (LRFs), Ultra-Wideband Radar (UWB), and hyperspectral sensors like hyperspectral cameras, which allows for its use in a variety of civilian and military applications [1,2] and missions including the magnetometer for geological and mining research [3–9]. Other authors have used drone magnetometry in the oil and gas industry to locate abandoned wells and other

buried infrastructures such as pipelines over wide areas [10–12]. Traditionally, magnetic surveys are performed on-site moving the sensor manually, thus capturing high resolution spatial data at the cost of low productivity. These approaches are additionally limited by access to the area of study. Other approaches consist in the installation of sensors on planes, increasing productivity by being able to study larger areas in smaller periods of time, at the cost of spatial resolution [13]. The use of drones is thus an alternative of interest presenting multiple operative advantages, such as flexibility, ease of use, and a lower logistic cost. Additionally, drones present high capacity for obtaining data over large areas in short periods of time, with less restrictions based on low accessibility, topographical, environmental, and vegetative conditions.

One of the most common techniques used in geological and mining research is magnetometry, employing the use of specially designed sensors that can be made airborne using drones [14–16]. This consists of a means of remotely carrying out geophysical surveys based on the measurement of terrestrial magnetic variations at regular intervals along a set of profiles. The majority of minerals present their own particular non-magnetic behavior. Nevertheless, another group of minerals exists, called ferromagnectic minerals, which include the cobalt ores frequently found in the Estancias mountain range of the Betic Cordillera, Spain, whose concentration in the Earth's crust generates detectable local variations in the magnetic field.

The present research project is focused on the analysis of the Don Jacobo mine, where copper and cobalt minerals were found in Triassic carbonates and have been extracted since the mid-19th century, up to the beginning of the 21st century [17]. These minerals include azurite, malachite, limonite, pyrite, galena, and erythrite. Mining works in the area were limited to small galleries that penetrated only few meters into the rock. There are no data from previous geophysical surveys or drilling activities.

This study thus has the primary objective of extracting information from this area in relation to the possible presence of mineral bodies located under areas of complex topographies where high slopes, scree debris, and vegetation make the application of ground geophysical techniques difficult. It is known that these topographic particularities make it difficult to study this area using other ground geophysical techniques such as, for example, electrical tomography, induced polarization, and ground magnetometry, which highlights the importance of research with drones in this application.

2. Geological Context and General Characteristics of the Locality

The region of interest is located in the Estancias mountain range, in the southeastern part of the Iberian peninsula, geologically positioned in the northern region of the Internal Betic Cordillera (Figure 1A), in materials of the The Alpujárride Complex, belonging to the Internal Zones of the Betic Cordillera. The diverse lithologies present can be organized into three large lithological units defining this complex. Stratigraphically, these three units correspond with, from bottom to top: Paleozoic shales, Triassic phyllite-quartzites, and Triassic carbonates (dolomitic-limestone). The first two units are additionally affected by Alpine metamorphism.

These units are presented with a general east-west orientation (N75-90E) (Figure 1B), conditioned by a strong deformation due to tectonic accidents [18,19]. These accidents have been interpreted mostly as fault propagation folds towards the south/south-east [20], thus conditioning the geological structures within this region (Figure 1B,C).

The area occupied by the Don Jacobo mine, and the general location of the target minerals, are dispersed in a topographically abrupt region, positioned on a 1000 m by 300 m (length × width) portion of the Triassic dolomitic-limestone unit. This unit is located above phyllites and is constricted towards the south by an interpreted as a possible normal tertiary fault, partially covered by plio-quaternary materials (Figure 1C).

From a metallogenetic perspective, the mineralizations are located within the Upper Triassic dolomites and limestones of the Alpujarride Complex, and are considered to be stratobound [18]. Rich Co-Cu mineralization can be found here alongside other minor elements

(Ni-Pb-Zn-Ag-Se-As-Hg) [21]. This is similar to the geological-lithological contexts of the Betic region, such as those found in Molvízar (Granada) and Huércal-Overa (Almería).

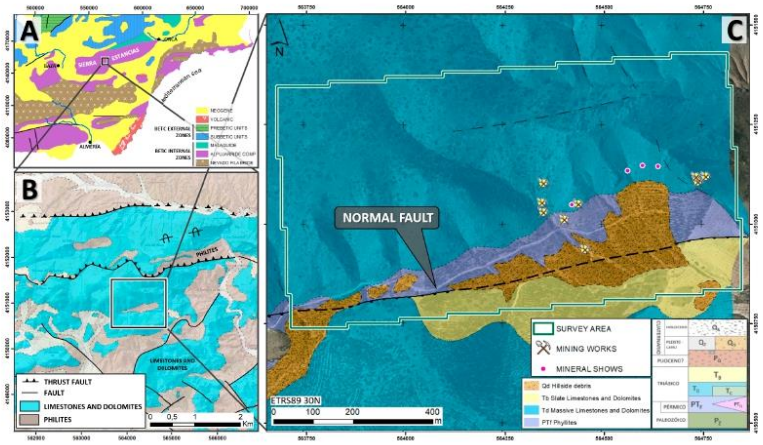

Figure 1. (**A**) Geological Context of the southeastern part of the Iberian Peninsula; (**B**) 1:50,000 Geological map (sheet 973—Chirivel and 995—Cantoria, Instituto Geológico y Minero de España, 1972 [18,19]), where the general east-west trend of the Alpujarride Complex can be observed; (**C**) 1:5000 cartographic revision of the Don Jacobo mine area, showing the main tectonic accident in the area (southern normal fault—black dashed line), survey area, and position of the Don Jacobo mines and outcropping mineral shows.

Genetically, these mineralizations have been attributed to a Mississippi Valley type, where metals are a product of the hydrothermal washing of marine series or from mafic intrusions, with carbonates acting as a reducing trap for the mineralization. The carbonated lithologies are constituted by large structures separated among themselves by phyllite lithologies, typically associated with important tectonic accidents. These accidents are then considered the potential channels for hydrothermal circulation [20].

The geochemical studies as well as nearby mineral indices documented from the initial exploitation of the Don Jacobo mine indicate the presence of Cu-Co-Ni primary mineralizations, with the presence of Pb-Zn (Ag), and with Cu and Co contents of >3% and 1%, respectively (Figure 2, [21]). No drilling data or geophysical surveys are available.

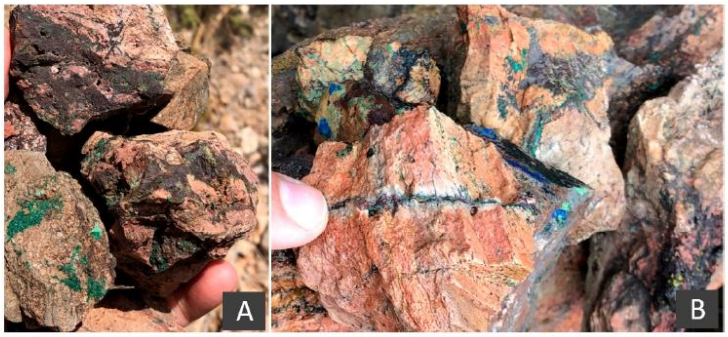

Figure 2. Mineralizations of the Don Jacobo mine; (**A**,**B**) Cu carbonates (green and blue colors) and veins of black Co oxides (black colors).

3. Materials and Methods

This research project consisted in the analysis of the mine's surroundings and outcropping mineral shows. Additionally, this research has tried to analyze the carbonated outcrops that appear over the 80 ha area.

3.1. Site Conditions

Data collection was performed on 14 June 2020 in warm, sunny, uncloudy, and low wind speed (<16 m/s) day, and lasted a total of 4 h (from 10 am. to 2 pm.). The area under study is practically covered with matorral type shrub-land, and scattered with dense wooded areas (Corine Land Cover 2018 types 312 and 323—https://land.copernicus.eu/pan-european/corine-land-cover/clc2018—accessed on 1 November 2021). The area is accessible by only one track and is characterized by a low anthropogenic magnetic noise area and a severe topography, with an average slope of >26° (Figure 3). To minimize risks such as drone collision with topographic or vegetative elements (the tallest trees in the area reaching approximately 8 m Above Ground Level-AGL) and to ensure flight at a constant height above the ground, a digital elevation model (DEM) of the area was first generated. For this flight, the most important geometric criteria for photogrammetric applications were considered [22], allowing the generation of cartographic data of high quality and obtaining a Ground Sample Distance (GSD) of 4 cm/pixel. This DEM was calculated using a Dji Mavic 2 Pro drone with a 1" CMOS sensor, flying at 150 m AGL.

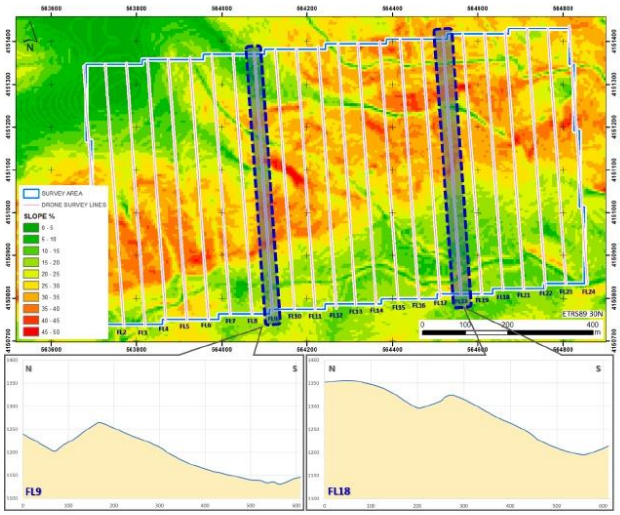

Figure 3. Slope map of the study area including drone flight lines (pink lines). The topographic profiles of flight lines 9 (FL9) and 18 (FL18) show the wild topographical characteristics of the area.

3.2. Platform and Flight Planning

The platform employed for the present study was the multi-rotor hexacopter Dji Matrice 600 Pro (Figure 5A), equipped with a A3Pro flight controller, and compatible with the UgCS mission planning tool software. This equipment has a total takeoff weight of 9.6 kg, and up to 6 kg payload, while being powered by 6 lithium polymer batteries (4500 mAh).

Flight software (UgCS) was used for the design and control of the survey. Twenty-four 650 m length parallel survey lines were flown trending N170E, orthogonal to the regional strike of the geological structure and mineralization (N75-90E), with a 50 m line separation in order to obtain a high spatial resolution that allows observing variations in the magnetic

field of target size. Due to the extension of the survey area, the total flight was divided into four flight blocks and two take-off and landing points taking into account the capacity of the batteries (Figure 4). The flight was programmed with a speed of 5 m/s and a sampling interval of 200 ms, obtaining measurements every meter along the registered profile. This selected configuration results in a total of 14,500 magnetic total field registration points. The altitude of the flight (20 m AGL) was selected to maximize the resolution of the sensor while guaranteeing safety against obstacles, integrating the DEM acquired previously. A 1 m tolerance level was also used for altitude adjustments.

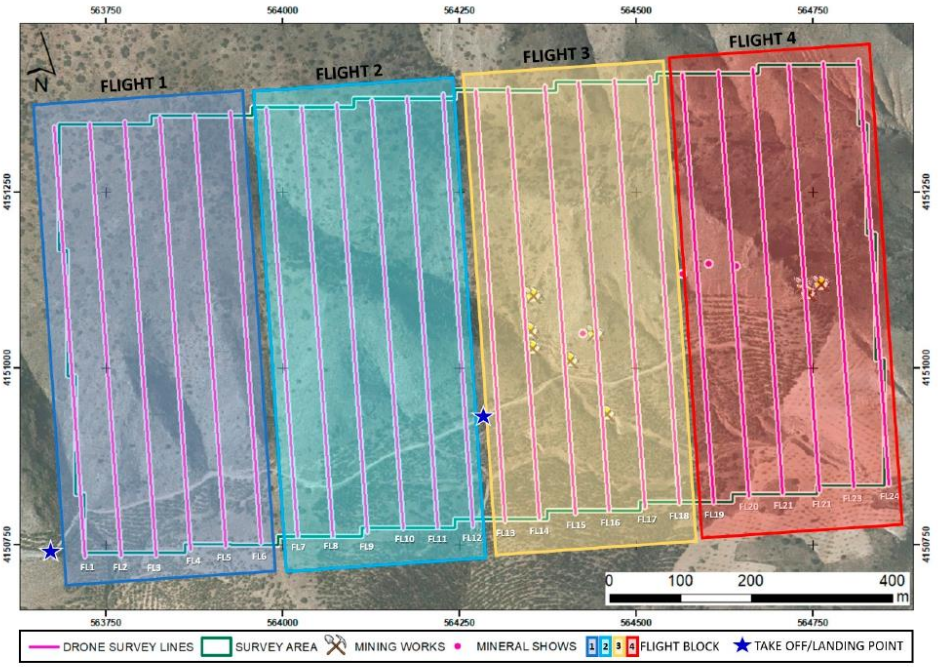

Figure 4. Survey design including flight lines (pink lines) and flying blocks division, including the take-off and landing points.

The effect produced by the distance between the sensor and the surface generates a low decrease of spatial resolution and intensity compared to ground surveys [16,23,24], compensated by a regular and higher density data acquisition.

3.3. Magnetometry

The drone was equipped with a GSMP-35U GEM-Systems potassium-vapor magnetometer, with a sensibility of 0.0002 nT/1 Hz. This system is additionally equipped with a simultaneous register of the magnetic field, as well as a real-time single-frequency (L1) GPS receiver with up to 0.7 m absolute accuracy in Satellite Based Augmentation System coverage areas.

This equipment consists of a sensor attached by cable to a controller, datalogger, 5 V battery power-source, and GPS, with a total weight of <2 kg. The datalogger and batteries were securely fixed and balanced in the payload container of the drone's undercarriage, while the GPS antenna was installed on the upper portion of the drone, so as to ensure a constant signal. Due to the magnetic interference that is generated by electromagnetic motors within the platform [5,24,25], the magnetic sensor was installed at a 3 m distance from the base of the drone, connected by cable, so as to counteract this electromagnetic

effect (Figure 5B). For this configuration, the magnetic field produced by the drone is attenuated and does not affect the measurements of the GSMP-35U magnetometer [20].

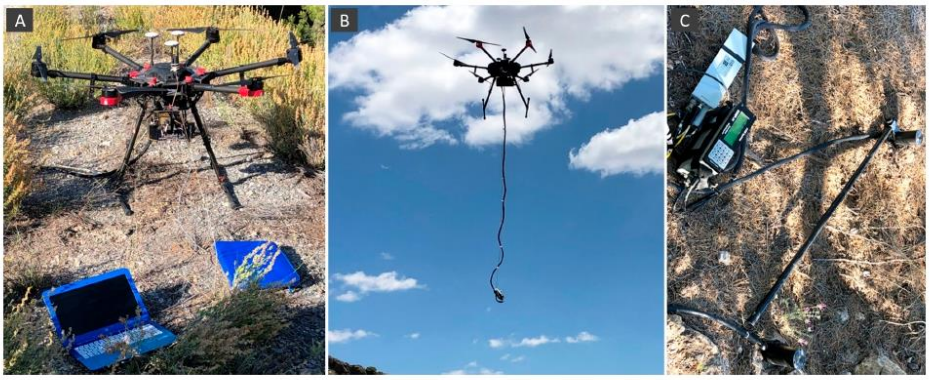

Figure 5. Registration system. (**A**) a Mavic Matrice 600 Pro Hexacopter drone; (**B**) static drone position with the magnetometer hanging below; (**C**) base magnetometer for diurnal corrections.

The magnetic sensor was deployed with no rotational restrictions about any of the axes. The survey was designed by adding an extra 25 m at each extremity of the flying lines at the 180° turn and reducing flight speed, preventing the pendulum motion of the sensor that creates yaw, pitch, and roll axis variations.

In parallel, a fixed magnetometer was installed in a nearby area away from sources of magnetic interference to calculate the diurnal effect correction caused by the temporal variation of the magnetic field throughout the day (Figure 5C). The magnetometer was set up with a 1 s time total field interval record, found to register a maximum of 11 nT throughout the data collection period.

3.4. Data Processing

Data were processed using the OASIS Montaj 9.8 software, using classic methods in the calculation of anomalies by applying a series of different filters so as to obtain anomaly residual maps. First, erroneous values due to drone position, take-off, landing, pitch, excess roll, and lag errors between the sensor and the drone are deleted. All points placed over the extended extremes of the survey lines and other outliners were discarded, applying a 1D median filter. Finally, diurnal variation of the Earth's magnetic field values caused by sun activity were used to correct the data obtained during the survey period [26].

Aeromagnetic data processing is based on a gridding computation routine that interpolates the observed aeromagnetic data from the survey data, placing these locations into a regular grid with the nodes displayed as a 2D total magnetic field contour map (RGB image). The minimum curvature gridding method was applied to the observed data [27], at $\frac{1}{4}$ of the flight line spacing (12.5 m) [28].

4. Results

4.1. Total Magnetic Field (TMF) and Reduction to Pole (TMFRP)

Data interpretation begins with the calculation of the Total Magnetic Field (TMF), from the filtered data (Figure 6A), and the Reduction to Pole (TMFRP). From this perspective, applying the data regarding magnetic inclination and declination of this area on the day of data collection, and in combination with the International Geomagnetic Reference Field (IGRF), a view of the central magnetic sources can be obtained directly for the bodies that generated them (Figure 6B).

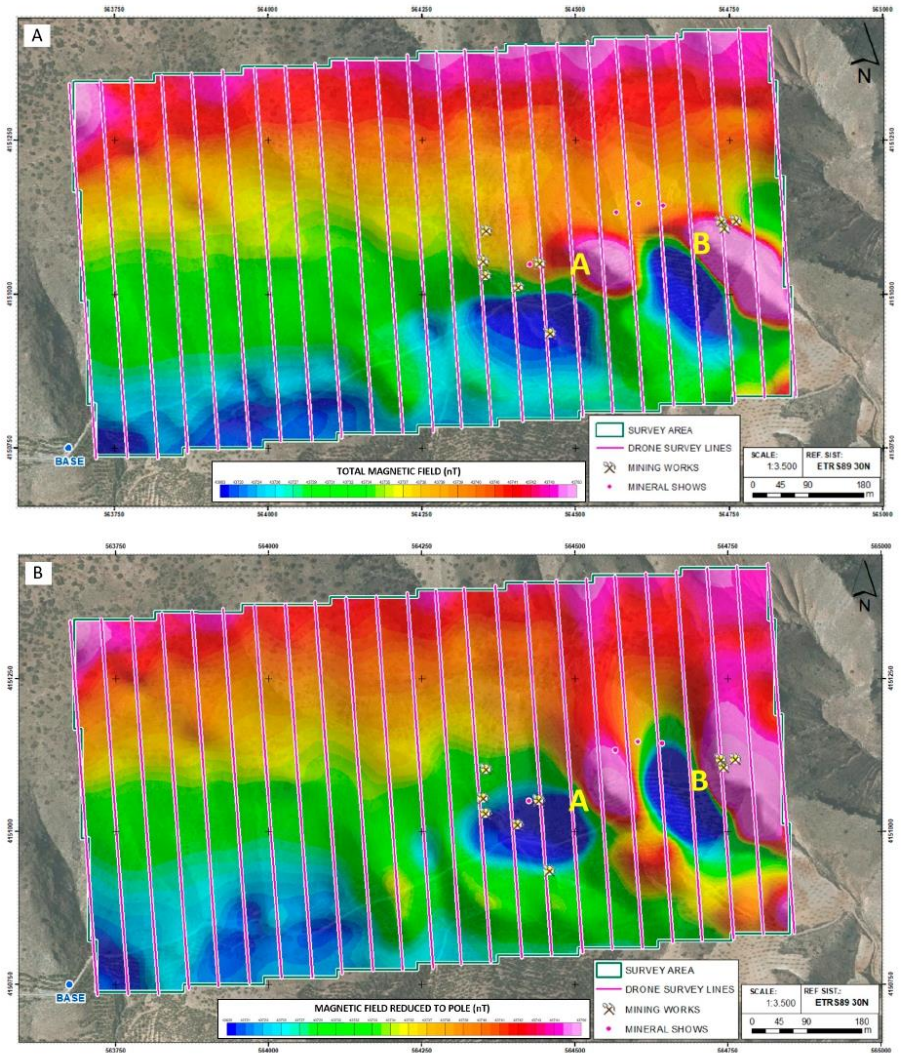

Figure 6. (**A**) Total Magnetic Field (TMF) and (**B**) Total Magnetic Field with Reduction to Pole (TMFRP). Dipoles A and B have been marked on each map, as well as the location of different mining activities and areas where the mineralization had been observed on the surface.

On both planes, the presence of two strong magnetic dipoles can be observed (A and B) towards the south-east quadrant of the region of interest. Both dipoles are located on carbonated materials and can be found in the immediate surroundings of the old mine as well as areas where the mineralization had originally been detected on surface.

TMFRP presents a slight variation in the position of the dipoles with reference to the TMF (Figure 6B), as well as an increase in its intensity, reaching a variation in the magnetic field of up to 88 nT (dipole A) and 165 nT (dipole B). The dipoles can be related to the

presence of ferromagnetic elements compatible with the paragenesis of the minerals from this locality.

It is important to point out that reduction to pole has not removed the dipolar character of the magnetic anomalies, which indicates a remaining magnetization of the materials found in this source. This is product of the natural axis of these dipoles, found approximately E-W and not N-S, as would be expected in the actual position of the magnetic field. Under this premise, the mineral bodies that generate these dipoles obtained the remaining magnetization at a moment in time when the magnetic field was different from present day.

4.2. Analytical Signal

The filtered Analytical Signal (AS) allows for the spatial identification of the two sources producing the observed dipoles. The calculation of AS is based on the execution of directional derivatives, where the obtained anomalies are organized in a bell-shape, and where the maxima are located directly on the edges of the anomalous bodies, with their amplitude being proportional to the depth of the location of the magnetic source [29].

The map displaying the computed analytical signal (Figure 7) presents a preferential lineation of anomalous areas with an approximate orientation of N80E, coinciding with the two maxima (A and B, Figure 7), and the general trend of the main geological contacts and structures, specially, with the normal fault defined through the geological cartography of the area (Figure 8).

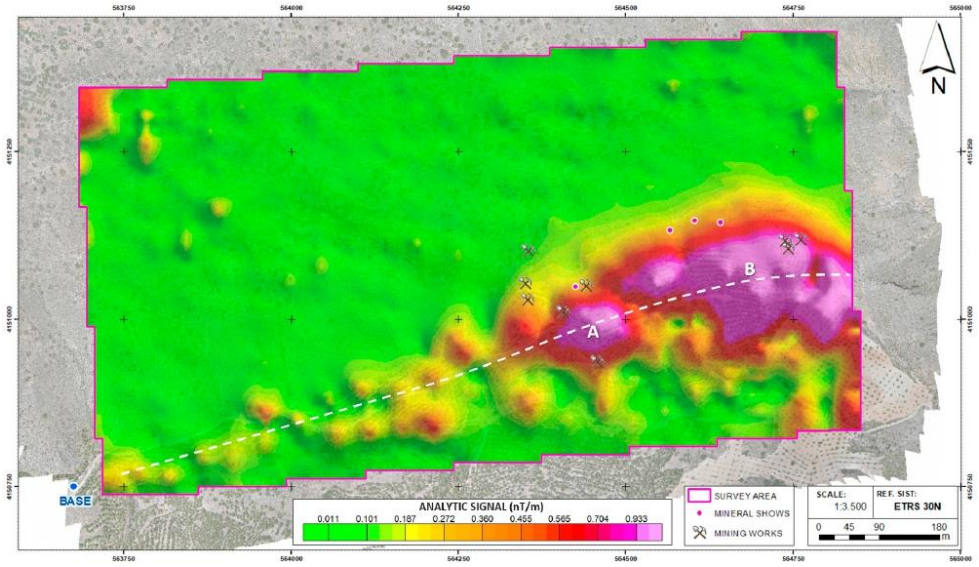

Figure 7. Analytical signal map over the aerial RGB image of the area of Don Jacobo with the position of the main mining works and outcropping mineral shows. Note the alignment of the analytical signal anomalies with approximate N80E orientation (white dashed line) and with the two AS maxima (A and B), as well as the position of the mining works and the outcropping mineral shows close to the main anomalies.

It is important to point out that all the mining works and outcropping mineral shows are located surrounding the northern part of the analytical signal anomalies, with all of them situated in the northern block of the normal fault.

4.3. D Inversion Model

The creation of a uniform grid with a high density of information obtained by drone allows to the creation of 3D models displaying magnetic susceptibility by applying the technique of Magnetic Vector Inversion (MVI) [30]. The model generated using the VOXI Earth Modeling software by OASIS Montaj is made up of a data mesh of 117 × 69 × 82, generating a total of 661,986 cells of 10 × 10 m size. This model facilitated the spatial definition of the precise magnetic bodies of interest. These methods also allow for the characterization of these bodies, through computing magnetization vectors for each block that contain information about directionality as well as intensity.

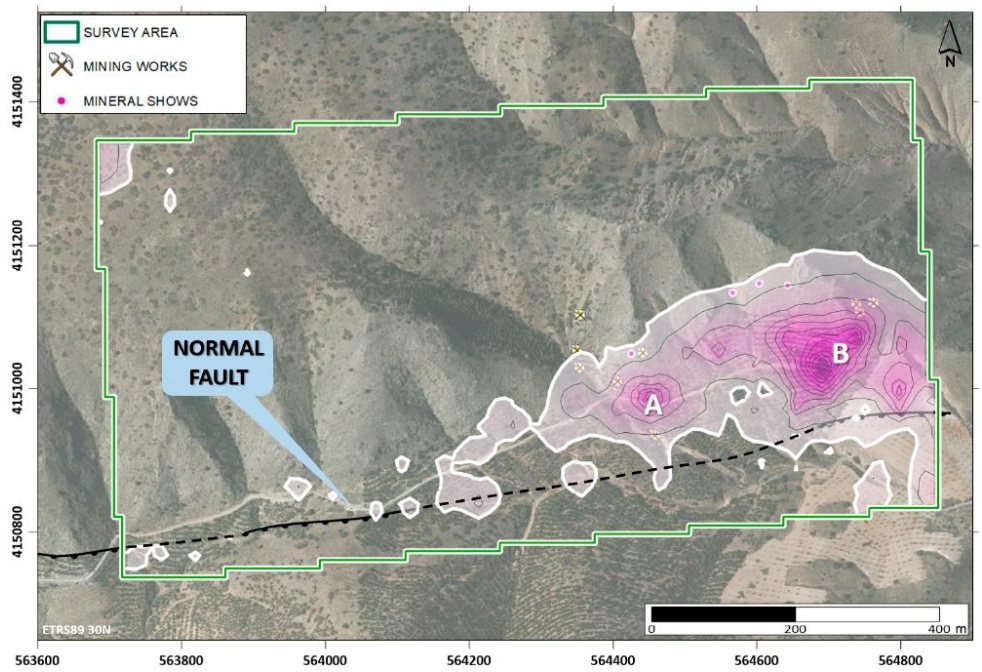

Figure 8. Analytical Signal anomalies over the aerial RGB image and normal fault trace from the 1:5000 geological cartography (Figure 1C) of the area of Don Jacobo. Note the alignment of analytical signal anomalies parallel to the normal fault placed at the south of the survey area.

The results from this modeling (Figure 9) reveals the presence of two bodies with high magnetic susceptibility (A and B), presenting susceptibility values over 12×10^{-4}, with peak values of 15×10^{-3}. Both bodies are modelled to prevent an oval morphology, with the maximal magnetization located at 45 m and 60 m in depth below surface (Figure 9A,B). This depth is an estimation and other methods such as drilling would be required to validate the proposed depth.

In the case of magnetization vectors, a preferential W-E orientation has been observed, different from the direction of the Earth's natural magnetic field. This model confirms the presence of a residual magnetization in the materials encountered here, coinciding with those observations obtained from TMFRP, and therefore, could be related to the presence of mineralized bodies.

Both bodies are located towards the south of the mining works and outcropping mineral shows and just at the north of the normal fault that crosses the southern border of the survey area (Figure 10), making it possible to interpret that the fault may have played

an important role in the formation of the mineralization, probably as a channel for the circulation of hydrothermal mineralizing fluids.

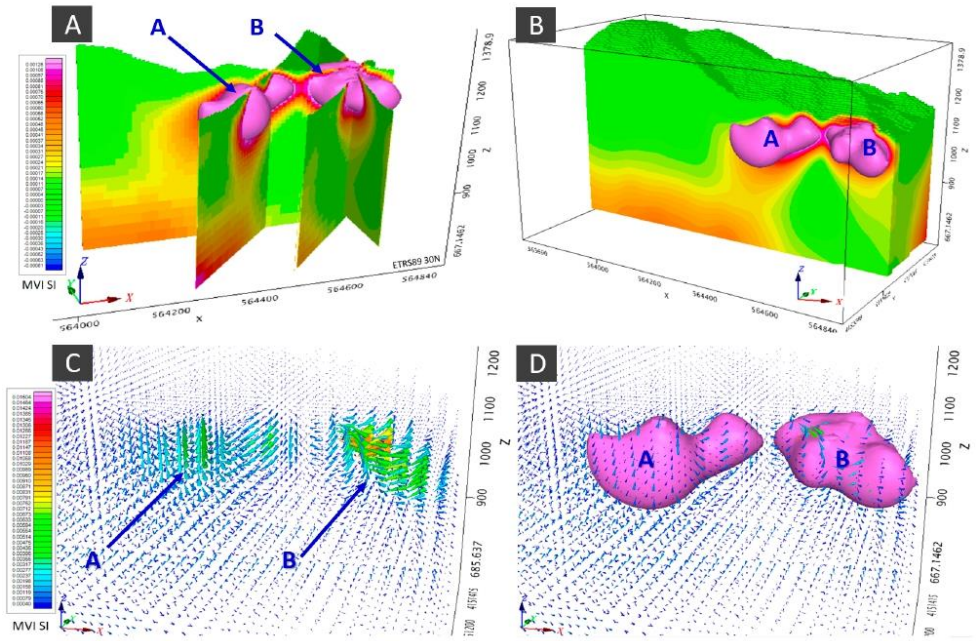

Figure 9. 3D model of the magnetic susceptibility in the area of Don Jacobo. (**A**,**B**) Different views and sections of the two magnetic bodies defined by the model. (**C**,**D**) Visualization of magnetization vectors obtained from each of the studies and their relationship with magnetic susceptibility.

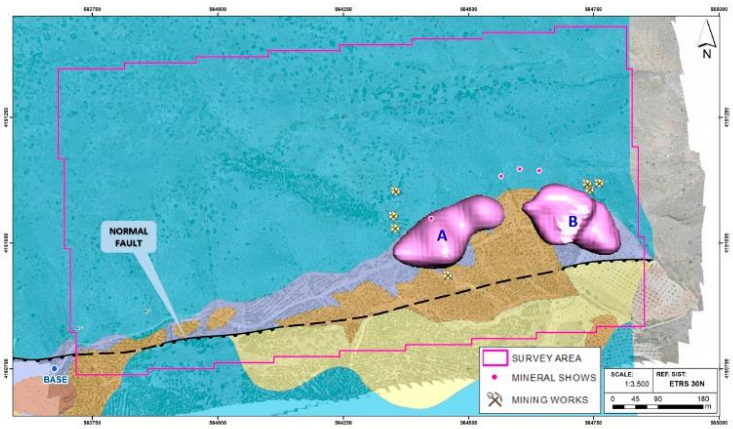

Figure 10. 3D model of the magnetic susceptibility of the Don Jacobo area, displaying the position of the two bodies of high magnetic susceptibility A and B (12×10^{-4} susceptibility threshold value); over the 1:5000 geological cartography and aerial RGB image of the area of Don Jacobo; normal fault placed at the south of the survey area and mining works and outcropping mineral shows.

5. Conclusions

We present results of the drone magnetometry survey for mineral exploration over the Don Jacobo mining area. We demonstrate the utility and advantages of using drone magnetometry in the study of mineral deposits, allowing for the acquisition of high-quality data in unfavorable conditions where traditional approaches are limited.

The present study was able to detect the presence of two magnetic dipoles with residuals magnetization in the nearby surroundings of old mining activities.

The use of 3D inversion was able to define the morphology and limits of the two potential mineral bodies, and further confirm their relation to the surrounding geological features, such as the normal fault to the south of the region of interest.

Our results strongly support that these dipoles are related to the potential presence of ferromagnetic mineral elements compatible with the Copper-Cobalt-Nickel paragenesis of the Don Jacobo area. The alignment of the analytical signal anomalies parallel and close to a normal fault indicate that this fault played an important role in the formation of the mineralization, probably as a channel for the circulation of hydrothermal mineralizing fluids.

We conclude that the drone magnetics survey method could be an important tool to study mineralized areas, such as the Don Jacobo mine, where precise modeling allows the precise definition of magnetic anomalies and the design and development of future investigation activities.

Author Contributions: D.P. and S.A.; methodology, D.P.; software, P.C. and J.C.; validation, D.P.; formal analysis, D.P.; investigation, D.P.; resources, D.P.; data curation, P.C. and J.C.; writing—original draft preparation, D.P. and R.L.G.; writing—review and editing, D.G.-A.; visualization, D.P.; supervision, D.G.-A.; project administration, D.G.-A.; funding acquisition, D.P. and R.L.G. All authors have read and agreed to the published version of the manuscript.

Funding: This research received no external funding.

Institutional Review Board Statement: Not applicable.

Informed Consent Statement: Not applicable.

Data Availability Statement: Not available.

Acknowledgments: We would like to acknowledge EXCO MINING SL and GEOLAND SERVICES SL for permitting the publication of this research, as well as for the chance to participate in this research project.

Conflicts of Interest: The authors declare no conflict of interest.

References

1. Giordan, D.; Adams, M.S.; Aicardi, I.; Alicandro, M.; Allasia, P.; Baldo, M.; De Berardinis, P.; Dominici, D.; Godone, D.; Hobbs, P.; et al. The use of unmanned aerial vehicles (UAVs) for engineering geology applications. *Bull. Eng. Geol. Environ.* **2020**, *79*, 3437–3481. [CrossRef]
2. Aleshin, I.M.; Ivanov, S.D.; Koryagin, V.N.; Matveev, M.A.; Morozov, Y.A.; Perederin, F.V.; Kholodkov, K.I. Review on the Use of Light Unmanned Aerial Vehicles in Geological and Geophysical Research. *Seism. Instrum.* **2020**, *56*, 509–515. [CrossRef]
3. Parvar, K.; Braun, A.; Layton-Matthews, D.; Burns, M. UAV magnetometry for chromite exploration in the Samail ophiolite sequence, Oman. *J. Unmanned Veh. Syst.* **2018**, *6*, 57–69. [CrossRef]
4. Shahmoradi, J.; Talebi, E.; Roghanchi, P.; Hassanalian, M. A comprehensive review of applications of drone technology in the mining industry. *Drones* **2020**, *4*, 34. [CrossRef]
5. Malehmir, A.; Dynesius, L.; Paulusson, K.; Paulusson, A.; Johansson, H.; Bastani, M.; Wedmark, P.; Marsden, P. The potential of rotary-wing UAV-based magnetic surveys for mineral exploration: A case study from central Sweden. *Lead. Edge* **2017**, *36*, 552–557. [CrossRef]
6. Park, S.; Choi, Y. Applications of unmanned aerial vehicles in mining from exploration to reclamation: A review. *Minerals* **2020**, *10*, 663. [CrossRef]
7. Kim, B.; Lee, S.; Park, G.; Cho, S.-J. Development of an unmanned airship for magnetic exploration. *Explor. Geophys.* **2020**, *52*, 1–6. [CrossRef]

8. Le Maire, P.; Bertrand, L.; Munschy, M.; Diraison, M.; Géraud, Y. Aerial magnetic mapping with an unmanned aerial vehicle and a fluxgate magnetometer: A new method for rapid mapping and upscaling from the field to regional scale. *Geophys. Prospect.* **2020**, *68*, 2307–2319. [CrossRef]
9. Schmidt, V.; Becken, M.; Schmalzl, J. A UAV-borne magnetic survey for archaeological prospection of a Celtic burial site. *First Break* **2020**, *38*, 61–66. [CrossRef]
10. Alex, N.; Timothy, S.d.S. A UAV-based magnetic survey method to detect and identify orphaned oil and gas wells. *Lead. Edge* **2019**, *38*, 447–452.
11. Hammack, R.W.; Veloski, G.A.; Lowe, R.; Zorn, A.; Wylie, L.; Schlagenhauf, M. *Using Drone-Mounted Geophysical Sensors to Map Legacy Oil and Gas Infrastructure*; National Energy Technology Laboratory (NETL): Pittsburgh, PA, USA; Medium: Morgantown, WV, USA, 2020.
12. De Smet, T.S.; Nikulin, A.; Romanzo, N.; Graber, N.; Dietrich, C.; Puliaiev, A. Successful application of drone-based aeromagnetic surveys to locate legacy oil and gas wells in Cattaraugus county, New York. *Appl. Geophys.* **2021**, *186*, 104250. [CrossRef]
13. Everett, M. *Near-Surface Applied Geophysics*; Cambridge University Press: Cambridge, UK, 2013.
14. Parvar, K. Development and Evaluation of Unmanned Aerial Vehicle (UAV) Magnetometry Systems. Master's Thesis, Department of Geological Sciences and Geological Engineering, Queen's University, Kingston, ON, Canada, 2016; pp. 1–141.
15. Parshin, A.; Morozov, V.; Blinov, A.; Kosterev, A.; Budyak, A. Low-altitude geophysical magnetic prospecting based on multirotor UAV as a promising replacement for traditional ground survey. *Geo-Spat. Inf. Sci.* **2018**, *21*, 1–8. [CrossRef]
16. Jackisch, R.; Madriz, Y.; Zimmermann, R.; Pirttijärvi, M.; Saartenoja, A.; Heincke, B.H.; Salmirinne, H.; Kujasalo, J.-P.; Andreani, L.; Gloaguen, R. Drone-borne hyperspectral and magnetic data integration: Otanmäki Fe-Ti-V deposit in Finland. *Remote Sens.* **2019**, *11*, 2084. [CrossRef]
17. Empresa Nacional Adaro de investigaciones Mineras (ADARO). *Programa de Investigación Sistemática de Recursos*; Zona Sureste, Sierra de Las Estancias; ADARO: Madrid, Spain, 1987.
18. IGME MAGNA; Instituto Geológico y Minero de España (IGME). *Hoja de Chirivel (973)*; Mapa Geológico de España (E. 1:50.000); Servicio de Publicaciones del Ministerio de Industria y Energía: Madrid, Spain, 1972; 46p.
19. IGME MAGNA; Instituto Geológico y Minero de España (IGME). *Hoja de Cantoria (995)*; Mapa Geológico de España (E. 1:50.000); Servicio de Publicaciones del Ministerio de Industria y Energía: Madrid, Spain, 1972; 51p.
20. EXCO MINING, SL. *Informe Geológico y Minero del Permiso de Investigación Burán*; Sierra de Oria, Informe Interno no Publicado; EXCO MINING SL: Madrid, Spain, 2019.
21. EXCO MINING, SL. *Análisis Geoquímico y Petrográfico de Muestras Superficiales Tomadas en el Permiso de Investigación Burán*; Informe Interno no Publicado; EXCO MINING SL: Madrid, Spain, 2020.
22. Hernandez-Lopez, D.; Felipe-Garcia, B.; Gonzalez-Aguilera, D.; Arias-Perez, B. An automatic approach to UAV flight planning and control for photogrammetric applications. *Photogramm. Eng. Remote Sens.* **2013**, *79*, 87–98. [CrossRef]
23. Cunningham, M.; Samson, C.; Wood, A.; Cook, I. Aeromagnetic Surveying with a Rotary-Wing Unmanned Aircraft System: A Case Study from a Zinc Deposit in Nash Creek, New Brunswick, Canada. *Pure Appl. Geophys.* **2018**, *175*, 3145–3158. [CrossRef]
24. Walter, C.A.; Braun, A.; Fotopoulos, G. Impact of three-dimensional attitude variations of an unmanned aerial vehicle magnetometry system on magnetic data quality. *Geophys. Prospect.* **2019**, *67*, 465–479. [CrossRef]
25. Jirigalatu, J.; Krishna, V.; Silva, E.; Døssing, A. Experiments on magnetic interference for a portable airbone magnetometry system using a hybrid unmanned aerial vehicle (UAV). *Geosci. Instrum. Methods Data Syst.* **2020**, *10*, 25–34. [CrossRef]
26. Telford, W.M.; Geldart, L.R.; Sheriff, R.E. *Applied Geophysics*, 2nd ed.; Cambridge University Press: Cambridge, UK, 1990; 770p.
27. Briggs, I.C. Machine contouring using minimum curvature. *Geophysics* **1974**, *39*, 39–48. [CrossRef]
28. Lee, M.; Morris, W. Quality assurance of aeromagnetic data using lineament analysis. *Explor. Geophys.* **2013**, *44*, 104. [CrossRef]
29. Nabighian, M.N.; Grauch, V.J.S.; Hansen, R.O.; LaFehr, T.R.; Li, Y.; Peirce, J.W.; Phillips, J.D.; Ruder, M.E. The historical development of the magnetic method in exploration. *Geophysics* **2005**, *70*, 33–61. [CrossRef]
30. MacLeod, I.N.; Ellis, R.G. Magnetic Vector Inversion, a Simple Approach to the Challenge of Varying Direction of Rock Magnetization. Australian Society of Exploration Geophysicists, Extended Abstracts. 2013, pp. 1–4, Melbourne. Available online: https://www.semanticscholar.org/paper/Magnetic-Vector-Inversion-%2C-a-simple-approach-to-of-Macleod-Ellis/9cd186fe7e6843baeb43c706d80fc64ffed3109a (accessed on 1 December 2021).

ARTICULO 3 Deep TDEM Study for Structural and Mining Purposes: A Case Study of the Barbastro Saline-Evaporitic Formation, Spain

Resumen:

El objetivo de este estudio ha sido la obtención de la estructura profunda de una formación salino-evaporítica afectada por una estructura anticlinal, definiendo la posición y espesor para su futura explotación (sales potásicas). Para mejorar este conocimiento se pueden aplicar métodos geofísicos que permitan establecer información detallada de la estructura geológica profunda. En este trabajo se analizan los resultados de una investigación profunda mediante sondeos eletromagnéticos en el dominio del tiempo (TDEM) en el flanco sur del anticlinal de Barbastro-Balaguer situado en la Cuenca del Ebro en las proximidades de Graus (Huesca, España), que controla la geometría de la formación Barbastro de naturaleza salino-evaporítica, de interés desde el punto de vista minero. Se ha empleado el sistema TDEM con una configuración que proporciona una capacidad de penetración hasta 3,0 km de profundidad. El procesado se ha basado en una inversión paramétrica sobre un sondeo con la columna litológica conocida (Monzón-1) para obtener un modelo de resistividad que posteriormente se aplica al resto de puntos de investigación. La metodología aplicada contribuye a mejorar el conocimiento geológico, permitiendo la obtención de la estructura geológica detallada y específicamente de la formación salino-evaporítica Barbastro, afectada por el anticlinal Barbastro-Balaguer.

El estudio muestra que la formación salino-evaporítica Barbastro presenta una estructura con el techo en forma de rampa con buzamiento general al SO y muro aplanado, con un espesor decreciente de 1103 m a 601 m, concordante con el modelo geológico y estructural aceptado previamente. El nuevo estudio geofísico aporta datos esenciales que permiten el diseño y optimización de sondeos en futuras explotaciones mineras.

applied sciences

MDPI

Article

Deep TDEM Study for Structural and Mining Purposes: A Case Study of the Barbastro Saline-Evaporitic Formation, Spain

Daniel Porras [1], Javier Carrasco [2], Pedro Carrasco [1,*] and José Luis Herrero-Pacheco [1]

[1] Department of Cartographic and Terrain Engineering, Geology, Polytechnic School of Avila, University of Salamanca, Av. Hornos Caleros, n° 50, 05003 Ávila, Spain; dporras@geoland.es (D.P.); joseluis.herrero@inge.es (J.L.H.-P.)
[2] Técnicas Geofísicas S.L., 05003 Ávila, Spain; tgeofisicas@gmail.com
* Correspondence: retep81@usal.es; Tel.: +34-920353500

Abstract: The objective of this study was to obtain the deep subsurface structure of a saline-evaporitic formation affected by an anticlinal structure, defining the position and thickness for its future exploitation (potassium salts). To improve this knowledge, geophysical methods can be applied to establish detailed information on geological structures at depth. This work analyzes the results of a deep time domain electromagnetic (TDEM) survey acquired over the southern flank of the Barbastro-Balaguer Anticline present in the Ebro Basin in the vicinity of Graus (Huesca, Spain), that controls the geometry of the Barbastro saline-evaporitic formation, of interest from the mining point of view. A deep time domain electromagnetic system (TDEM) is used, providing a penetration capability down to 3.0 km depth. A parametric constrained inversion over a lithological known borehole (Monzón-1) is used to obtain a resistivity model and then applied to the rest of the survey points. The applied methodology contributes to improving the geological knowledge, revealing a new detailed geological structure of the Barbastro saline-evaporitic formation affected by the Barbastro-Balaguer Anticline. The survey shows that the Barbastro saline-evaporitic formation presents a structure with a ramp hanging wall and close to flat footwall, generally dipping to the SW, with a decreasing thickness from 1103 m to 601 m, in concordance with the previous accepted geological structural model. The new geophysical study provides essential data, allowing design and drilling optimization in future mining exploitations.

Keywords: deep time domain electromagnetics; geophysics; mineral exploration; saline deposits; Barbastro Formation

Citation: Porras, D.; Carrasco, J.; Carrasco, P.; Herrero-Pacheco, J.L. Deep TDEM Study for Structural and Mining Purposes: A Case Study of the Barbastro Saline-Evaporitic Formation, Spain. *Appl. Sci.* **2023**, *13*, 6385. https://doi.org/10.3390/app13116385

Academic Editors: Paolo Mauriello and Domenico Patella

Received: 21 April 2023
Revised: 11 May 2023
Accepted: 18 May 2023
Published: 23 May 2023

1. Introduction

The constant increase in raw materials demand to supply the global industry necessitates the investigation of increasingly complex mineral deposits at greater depths. This type of project represents a challenge, in which the development of investigation tools is a fundamental pillar. In this context, geophysical investigation techniques are presented as a fundamental tool for the investigation and analysis of these new mineral deposits.

In the North of Spain there is an industry based on the extraction of potassium salts. The exploitation of these salts is carried out by dissolution processes through drilling and subsequent evaporation and processing of the extracted brine in ponds. These salts are found within the Barbastro Formation, which is located in an outcropping anticline structure (Barbastro-Balaguer Anticline). The progressive depletion of the currently exploited areas, located in the outcropping part of the formation and nearby areas, makes necessary the investigation and delimitation of the saline materials at greater depths, given its affectation by the regional anticline structure.

The application of geophysical tools in the resolution of geological and structural problems has experienced an important evolution in recent times, due to the improvement in the equipment power, resolution and penetration capacity. In this case, one of the most

used geophysical investigation systems due to its high resolution and penetration capacity is the time domain electromagnetic method (TDEM).

TDEM surveys have been widely applied to investigate and solve problems in geology, hydrogeology, environmental studies, mining and geothermics, providing subsurface resistivity models at relatively shallow depths (up to 1000 m) [1–8]. There are few publications about the use of the TDEM system (Monex Geoscope LTD.; The Basin, VIC, Australia) to analyze great depths, mainly due to the technical limitations of the equipment; however, depths greater than 2000 m have been reached in hydrogeological studies [9–14], and also in oil and gas exploration, in which TEM data allows a resources estimation and well optimization [10]. The equipment used in this study, TerraTEM with TerraTX-50 transmitter (Monex Geoscope LTD.; The Basin, VIC, Australia) and the acquisition parameters and configuration (coincident-loop 600 m × 600 m square configuration, 96 volts output voltage and 40 ampere transmitter current, and late delay times (over 1 s)) allowed us to reach larger depth ranges than usual in the industry, reaching up to 3000 m depth.

In this study, TDEM was applied to obtain a novel approach to the structure of the saline-evaporitic Barbastro formation in the southern flank of the Barbastro-Balaguer anticline in an area southwest of Graus (Huesca, Spain), where the development of new mining projects related to the exploitation of potassium salts is expected. Different inverted models were confronted with one parametric layered constrained model based on a lithological drilling log (borehole Monzon-1). The parametric constrained model was then used in the rest of the TDEM survey points as a starting model. Data, 1D models, and formation surfaces arising from a new electromagnetic survey are presented. The applied methodology allows for an improved detailed geological and structural view of the saline-evaporitic Barbastro Formation.

The new survey suggests that the general structure of the saline-evaporitic Barbastro Formation, and, therefore, of the materials affected by the regional anticlinal structure, presents a ramp hanging wall and close to flat footwall structure dipping to the SW, in concordance with the previous accepted geological structural model. This structure involves a thickness loss to the SW due to the defined structure, ranging in the survey area from 1103 m to 601 m. Hence, our study contributes to improving the geological structure and position of the saline materials, allowing design and drilling optimization in future mining exploitations.

2. Geological Settings

The study area is located at the northern margin of the Ebro Foreland Basin in the central sector of the South Pyrenean fold and thrust belt, which formed during the continental collision between the Iberian and Eurasian plates, from the Late Cretaceous to Miocene [15–19] (Figure 1). This collision resulted in the growth of an antiformal stack of basement-involved thrust sheets in the axial zone acting as a boundary between the South and North Pyrenean fold and thrust belts [20]. The South Pyrenean fold and thrust belt consists of a system of south-verging thrust sheets and the related Ebro Foreland basin emplaced in a piggy-back sequence from the Late Cretaceous to the Oligocene Pyrenean compression [21–24]. These tectonic units detached predominantly above Upper Triassic evaporites [25] and above Eocene evaporites deposited in the foreland basin [26,27]. The Foreland Ebro Basin is the late non-marine stage of the South Pyrenean foreland basin, which developed since the middle Priabonian at 36 Ma [28]. The system of folds deforming this foreland basin detached above the Cardona salt and gypsum from the Barbastro Formation [27,29] resulting in the formation of the Barbastro-Balaguer Anticline [30].

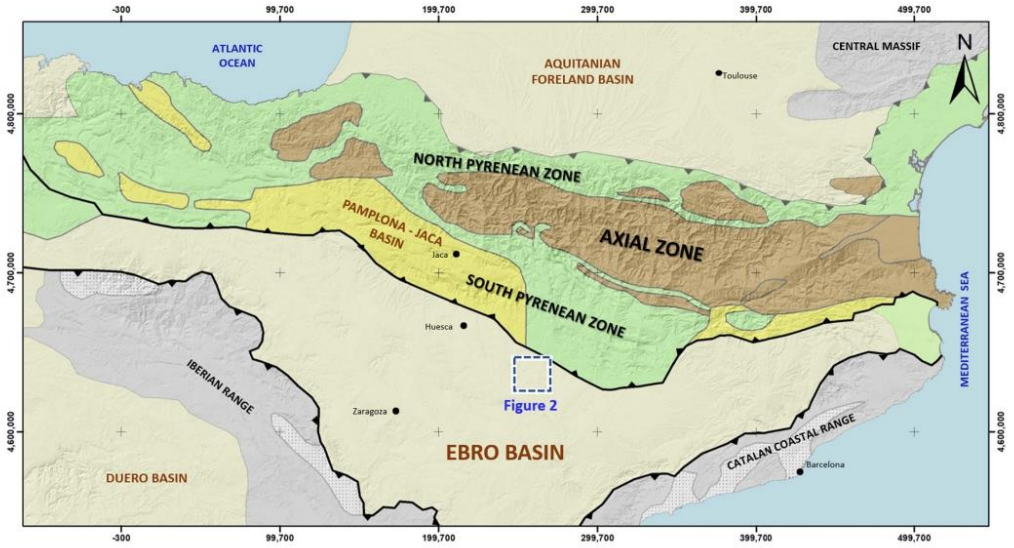

Figure 1. Simplified geological sketch of the Pyrenees and Ebro Basin area. Blue dotted line indicates the location of the survey area reflected in Figure 2.

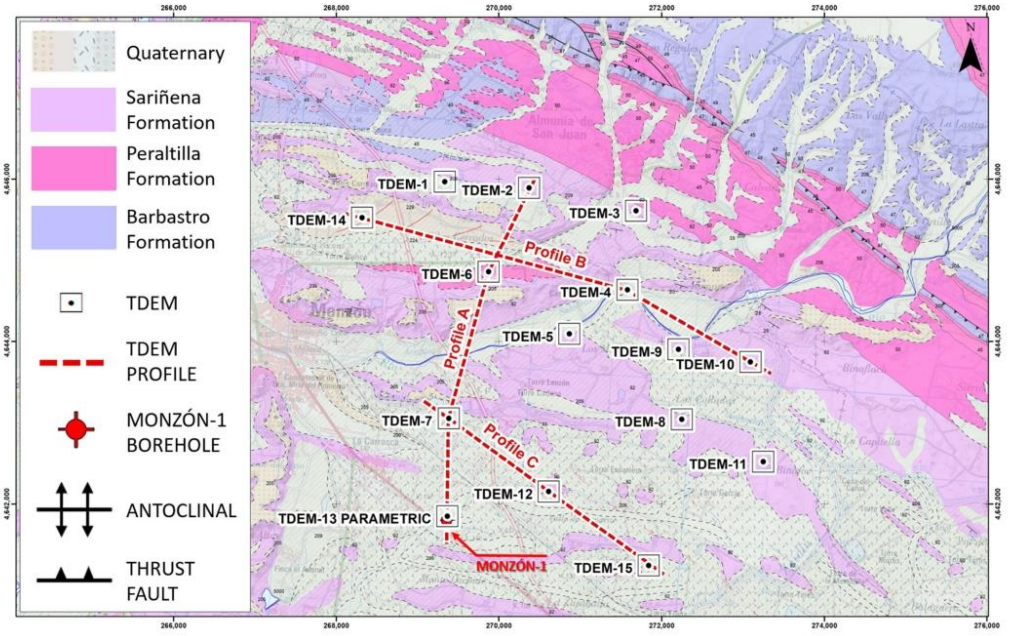

Figure 2. Geological map of the study area based on 1:50,000 cartography (sheet 326, Monzón, Instituto Geológico y Minero de España, 1974). Location of the Monzón-1 borehole and TDEM survey points are displayed with geophysical profiles described in Section 5.

The study area is located in the surroundings of the Monzón-1 well. It is located at the southern flank of the Barbastro-Balaguer anticline [31] which detached in the evaporites of the Barbastro Formation at the front of the Southcentral Pyrenean unit [32,33]. According to Lanaja [31], the infra-detachment stratigraphy consists of: (1) Lower Triassic red sandstones and claystones from the Bundanstein Facies; (2) Middle Triassic limestones, dolostones and anhydrite from the Muschelkalk; (3) Upper Triassic red claystones and evaporites from the Keuper; (4) Lower Jurassic limestones, dolostones and carbonatic breccias; and (5) Lower Eocene limestones. Folded strata from the Barbastro anticline comprise Cenozoic strata related to the later stages of evolution of the South Pyrenean foreland Basin. The main detachment is the Barbastro Formation, which consists of Priabonian gypsum and grey lutites deposited in a lacustrine evaporite sedimentary environment [34], with interbedded decameter halite and anhydrite packages [33]. Significant halite deposits are also known in this formation, as evidenced in the Monzón-1 well as in different wells where this material is exploited for the electrochemical industry. Significant halite deposits are also known in this formation, as evidenced in the Monzón-1 and other wells in the area where this material is exploited for the electrochemical industry. The upper part of the Barbastro Formation consists of lacustrine limestones, mudstones, sandstones and minor contents of gypsum acting as a transition to the overlying Peraltilla Formation. The Barbastro Formation outcrops in the core of the Barbastro-Balaguer Anticline [30,35], a 150 km NW-SE direction structure parallel to the Sierras Marginales front. The thickness of the gypsiferous zone of the Barbastro Formation is difficult to measure at the surface, due to the great deformation on the anticlinal outcropping area, although it decreases progressively towards the South [36]. The Peraltilla Formation consists of Middle Rupelian to Chattian conglomerates, sandstones and mudstones covered by similar sedimentary rocks from the Chattian to Aquitanian Sariñena Formation [36–38]. Both detrital siliciclastic formations are interbedded with decimeter-thick lacustrine limestones and gypsum [39,40].

Monzón-1 Borehole

The Monzón-1 borehole lithological drilling log with chronostratigraphic interpretation is available. Monzón-1 is an oil & gas wildcat borehole drilled by ENPASA in 1963 that reached 3714.60 m depth.

This borehole is a very important element, as it is the basis for the interpretation of the geophysical data. The borehole crosses the Cenozoic continental series of the northern edge of the Ebro Basin, reaching the base of the sedimentary basin constituted by the local Mesozoic substratum. The Barbastro Formation presents a depth of 886 m, located between 1402 m and 2268 m deep. From the lithological point of view, the Barbastro Formation is composed by an alternacy of gypsum and marls levels with interbedded decameter-thick halite and anhydrite packages, with a 90 m thick massive gypsum level close to the hanging wall of the formation. A detailed lithological log analysis lets us conclude that the salt and evaporites content is not constant, decreasing to the hanging wall and footwall of the formation; this content, being the zone of interest due its saline composition, is located between 1433 and 2034 m depth, reducing the real thickness to 601 m.

3. Data and Methodology

3.1. Time Domain Electromagnetics (TDEM)

TDEM uses transient electromagnetic field diffusion under time-domain control [41,42]. A time-varying magnetic field is created using a loop of wire. The methodology is based on a ground current injection through a transmitter (T_x) loop that is alternatively turned on and off. As a consequence of the current injection, a magnetic field perpendicular to the plane of the transmitter loop will be produced. When the current injection is turned off, the decay of the primary field induces electromotive forces within the surface, generating eddy currents that penetrate into the ground, creating a secondary magnetic field whose amplitude decreases with time (transient). The voltage against time for the decay secondary magnetic field associated with the eddy currents produced by the primary transmitter is

measured during the turn-off period by the receiver loop (R_x). The decay is measured at several times, obtaining of a curve which amplitude and shape reflects the distribution of resistivity with depth, where early times provide information at shallow depths while later times provide the information about deeper depths. Detailed description of the physical background of the TDEM method can be found, for example, in Fitterman and Stewart [43].

3.2. Survey and Data Acquisition

A total of 15 deep TDEM survey points were executed on a close to flat area covered mainly by vegetable crops. TDEM data were acquired using a TerraTEM system (Monex GeoScope Ltd.; The Basin, VIC, Australia) together with a TerraTX-50 transmitter (Figure 3). The Terra TX-50 transmitter delivers an output voltage of 96 volts and 50 A transmitter current, with a GPS synchronization module. A coincident-loop 600 m × 600 m square configuration was selected to obtain higher penetration and better signal to noise levels at late points, allowing a more reliable apparent conductivity estimation at depth [44]. Loops were laid out using a compass for correct placement. TDEM locations were determined using a handheld 3 m accuracy GPS while topography heights were extracted from 5 m resolution DEM (Instituto Geográfico Nacional, https://centrodedescargas.cnig.es/CentroDescargas/index.jsp) (accessed on 11 October 2022).

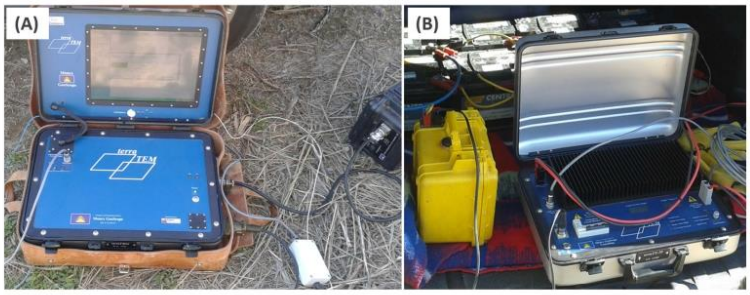

Figure 3. Field picture of the (**A**) TerraTEM equipment with the (**B**) Terra TX-50 transmitter.

TDEM survey points were distributed in a self-regular grid covering the selected survey area, where there was sufficient spacing for the loop laying and avoiding the close presence of anthropogenic interferences. TDEM-13 was laid out in the vicinity of the Monzón-1 borehole. The presence of power lines, plot fencing and lack of spacing in some points, especially in the southern part of the study area, generated a deformation of the recording grid, creating a final non regular grid with an important gap between southern survey points (TDEM-7, 12, 13 and 15) and the northern ones (TDEM-5, 6, 8 and 11) (Figure 2). To improve data quality during acquisition and decrease the interference noise, a strong signal and enhanced signal-to-noise ratio proceeding was established based on up to 4000 stacks per channel [45] and a high current external transmitter (up to 50 amperes)0020(Figure 4).

3.3. Processing Strategy

Raw recorded field data was downloaded and transformed into usf format to numerically process using TerraTEM equipment TEMPlot V 2.0.0 software (Monex GeoScope Ltd.; The Basin, VIC, Australia), allowing the display of voltage/time curves, automatic and manual filtering to remove wrong time windows and the exporting of initial preprocessed data.

TDEM was modeled using the commercial IX1D-V3 software (Interpex Limited; Golden, CO, USA), designed for a 1D analysis of electric and electromagnetic data inversion and interpretation. The inversion software obtains 1-D resistivity models, producing geoelectric resistivity versus depth columns for each TDEM.

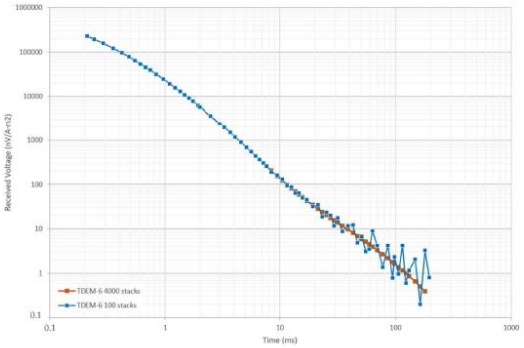

Figure 4. Decay curves in TDEM-6 with 100 stacks and 4000 stacks. Noise effect can be noticed from 8 ms in 100 stacks survey decay curve, disappearing in the 4000 stacks acquisition parameters.

The inversion software allows the user to insert an initial geoelectrical model with a preferred number of layers, resistivity values and thickness. For this task, data processing started with a parametric TDEM (TDEM-13) executed close to the Monzón-1 borehole. The available lithological information was used to define the number of layers and its thickness, only allowing the inversion software to adjust the resistivity of the layers in the model, to get the best fit of the model curve convergence with the field data. As a result of this process, an initial model based on the lithological data from the borehole and layer resistivity was obtained. The inversion process was repeated iteratively until a minimum RMS % model was obtained, showing the model adjustment degree to the data.

The remaining TDEM survey points were then inverted using the parametric model, allowing the inversion software to adjust the model curves to better fit with the field data, adjusting its thickness and contacts.

4. Inversion Results

Inversion starts with the analysis of the parametric TDEM executed next to the Monzón-1 borehole (TDEM-13 parametric). According to the lithological drilling log of the Monzon-1 borehole, a seven-layer geoelectrical model with next defined thickness and depth contacts is be defined (Figure 5).

Layer 1 consists of quaternary materials, with a thickness of 54 m. Layer 2 corresponds to continental tertiary materials of the Sariñena Formation, mainly silts, mudstones and sandstones, extending between 54 and 982 m deep. Under this layer, the materials of the Peraltilla Formation appear in layer 3, similar to the previous layer but with a higher relative proportion of sandstones. This layer extends to 1433 m depth, comprising the first meters of the Barbastro Formation, with low salt and gypsum content. Layer 4 consists of the most saline and evaporitic part of the Barbastro Formation, with predominance of anhydrite and massive salty layers. The layer is 601 m thick, extending between 1433 and 2034 m deep. Layer 5 constitutes the transition layer between the bottom non saline part of the Barbastro Formation with the Red Marls Formation, up to the Jurassic, showing a thickness of 413 m. The Jurassic limestones is layer 6, located between 2447 and 2656 m depth. The last layer, layer 7, contains all the Triassic materials up to the end of the drilling, composed of clays, evaporitic materials, sandstones and limestones.

Due to limitations of TDEM survey acquisition parameters (big loop size and measuring windows), a lack of data (ramp) on the first meter's depth is obtained, affecting the layers near the surface, so the depth of layer one (quaternary) was fixed due to the processing at close to 54 m, even thought the borehole lithological description only reflects a few meters of these materials.

As a result of this process, an initial model based on the lithological data from the borehole and layer resistivity was obtained. The designed model obtains an RMS % fitting

error of 0.65, indicating a good fit of the model curve based on the proposed geoelectrical model with the field data.

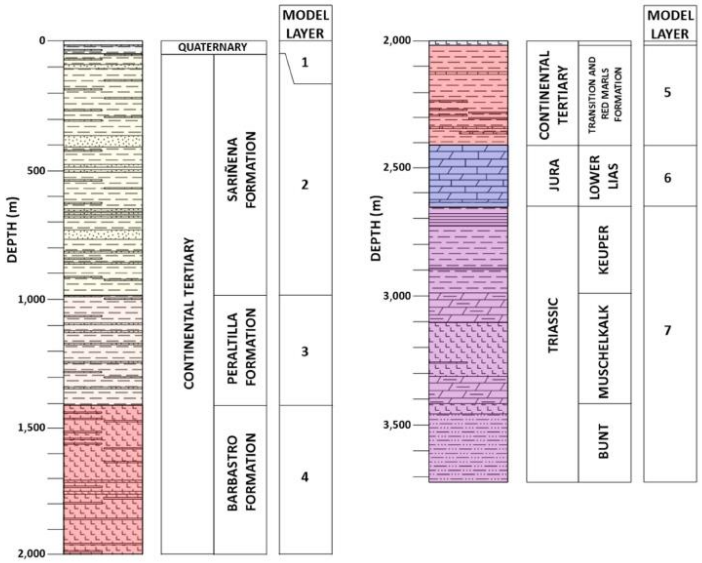

Figure 5. Lithological log of Monzón-1 borehole with indication of the geoelectrical model layers position.

There are other models equally consistent with the measured data (Figure 6B). All the equivalent models present similar results in the upper part of the data, layers 1 and 2. Additionally, the contact position between layers 2 and 3 corresponds to the hanging wall of the most saline-evaporitic part of the Barbastro Formation. The resistivity and contact position between layers 3 and 4, and the rest of the layers, shows bigger disparity between models. Taking into account that, although the equivalent models are viable from the geophysical point of view, they imply a worse correlation with the observed lithological data; these equivalent models were therefore discarded.

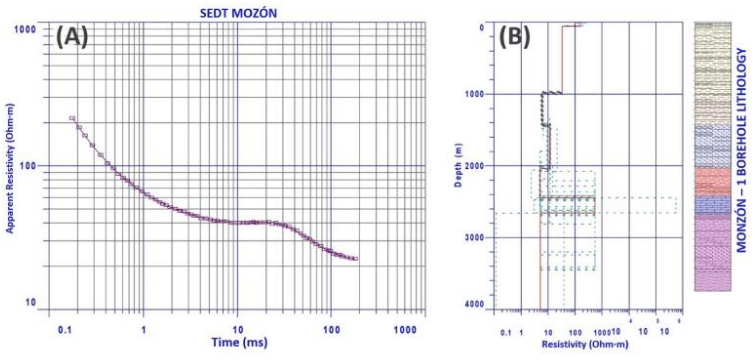

Figure 6. (**A**) Apparent resistivity–time curve for parametric TDEM-13 and (**B**) geoelectrical model based on the lithological log of Monzón-1 (red) and equivalence models (dashed green lines).

After the obtaining of the parametric model, it was applied to the rest of the TDEM resistivity–time curves (Figure 7) to obtain the geoelectric resistivity–depth columns. RMS% residuals error obtained for all the TDEM survey presents acceptable values, between 0.64–1.88%.

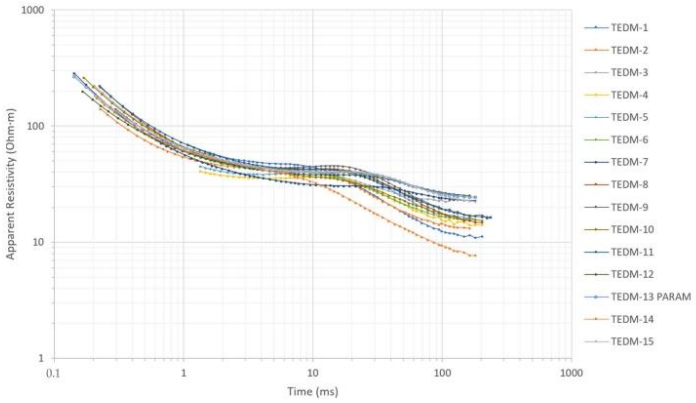

Figure 7. TDEM resistivity—time curves.

5. Discussion

Once the parametric model was obtained and used to obtain the 1D model (resistivity-depth) of all TDEM survey points, three profiles were elaborated to visualize the structure and thickness variation of the saline-evaporitic Barbastro Formation (Figure 2): Profile A, with NW-SE orientation, and Profiles B and C, with NW-SE orientation. Profile A's path follows the supposed maximum slope and strike of the Barbastro-Balaguer Anticline in the survey area, deduced from the geological cartography (Figure 2), while Profiles B and C were placed perpendicular to Profile A. All TDEMs reached a minimum penetration over 3000 m, enough to reach the hanging wall and footwall of the Basbastro Formation and reach the Mesozoic local basement. TDEM is very sensitive to the conductive layers [45,46], helping to distinguish the saline-evaporitic formation from the upper and lower geological formations due to its higher resistivity.

Profile A (Figure 8) follows the deduced maximum slope of the saline-evaporitic Barbastro Formation. The hanging wall is located at greater depths as we move to the SW, ranging from 1000 m to 1433 m depth. The footwall shows a subhorizontal morphology with slight depth variations, being located along the profile around 2050 m depth. As a result of the defined structure, saline-evaporitic materials thickness ranges along the profile from 1077 m to 601 m.

Profiles B and C follows the same direction as the Barbastro-Balaguer anticline, but at different distances from the axis, so a thickness decrease of the saline-evaporitic Barbastro Formation is observed towards Southwest, but with a constant value along the profile. Profile B defines a 900 m thickness of the saline-evaporitic formation with the hanging wall and footwall placed at 1125 and 2030 m depth, respectively (Figure 9B). Profile C, located further to the SW, shows the thinning of the Barbastro Formation as it is placed away from the core of the anticline, showing a formation thickness close to 670 m, with the hanging wall lying at 1375 m depth, while the footwall is located at 2050 m depth (Figure 10B).

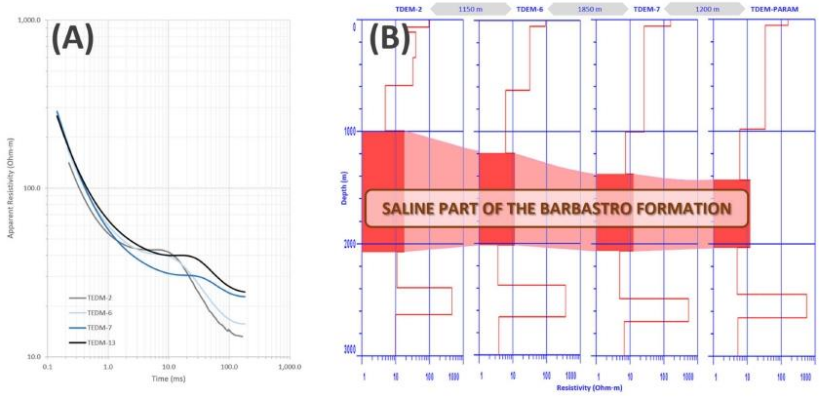

Figure 8. Profile A. (**A**) TDEM-2, 6, 7 and 13 (parametric) resistivity-time curves and (**B**) resistivity-depth models with indication of the inferred position of the saline-evaporitic Barbastro Formation.

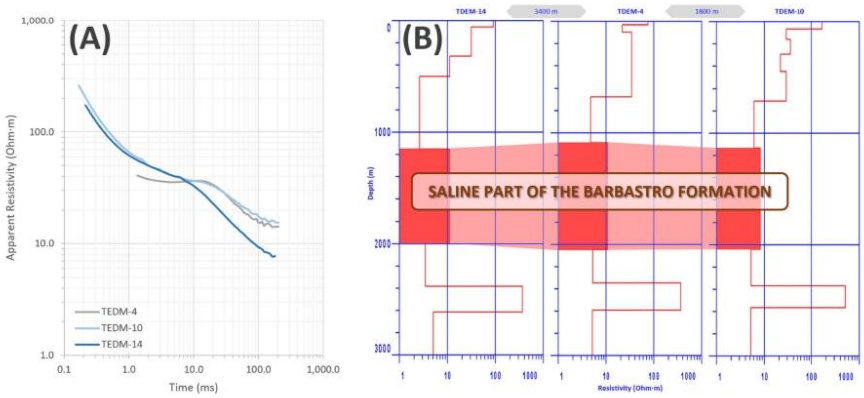

Figure 9. TDEM Profile B. (**A**) TDEM-14, 4 and 10 resistivity–time curves and (**B**) resistivity–depth models with indication of the inferred position of the saline-evaporitic Barbastro Formation.

D Surfaces and Thickness Map

The processing and interpretation of the TDEMs attempted to obtain the position of the hanging wall and footwall of the saline-evaporitic part of the Barbastro Formation. An interpolation processing using Surfer V 15.1 software (Golden Software LLC.; Golden, CO, USA) allows us to obtain both surfaces, defining the main structure of the formation and Barbastro-Balaguer Anticline.

Figure 11 integrates all interpreted TDEM points, showing the spatial elevation of the hanging wall and footwall of the saline-evaporitic Barbastro Formation in the survey area. In case of the hanging wall surface, the outcropping mapped position based on the official geological cartography 1:50,000. Magna [47] is used in the interpolation process to define its morphology and limit due to its outcropping to the North. According to the obtained surface (Figure 11A), the hanging wall surface becomes progressively less steep as we move to the SW, with a dip varying between 40° in TDEM-2 zone to almost subhorizontal in the southernmost TDEM survey points area (TDEM-13 and TDEM-15). The hanging wall elevation ranges between −658 and −1135 m above sea level (masl) (996 and 1433 m depth). The footwall shows a subhorizontal morphology, with small

elevations and small local depressions, recording in the TDEM elevations between −1640 and −1762 masl (2001 and 2101 m depth) (Figure 11B). The inferred structure agrees with the initial geological structure.

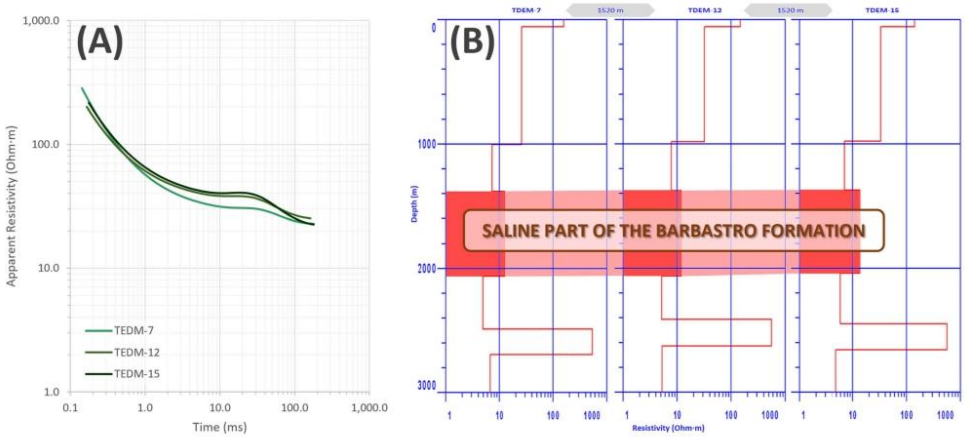

Figure 10. Profile C. (**A**) TDEM-7, 12, and 15 resistivity–time curves and (**B**) resistivity–depth models with indication of the inferred position of the saline-evaporitic Barbastro Formation.

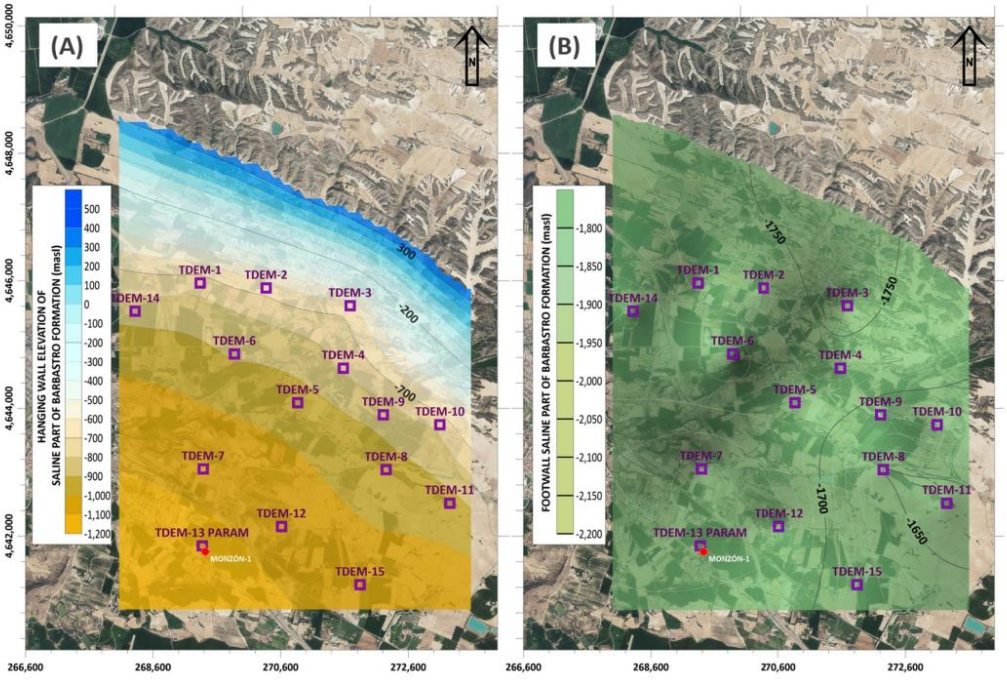

Figure 11. Elevation (meters above sea level (masl)) of the hanging wall (**A**) and foot wall (**B**) of the saline-evaporitic Barbastro Formation in the survey area.

Once the hanging and footwall surfaces have been obtained, the saline-evaporitic part of the Barbastro Formation thickness can be calculated, which ranges between 601 and 1103 m in the TDEM survey points, decreasing in the SW direction according to regional anticlinal defined structure (Figure 12) constrained by the hanging wall depth variation.

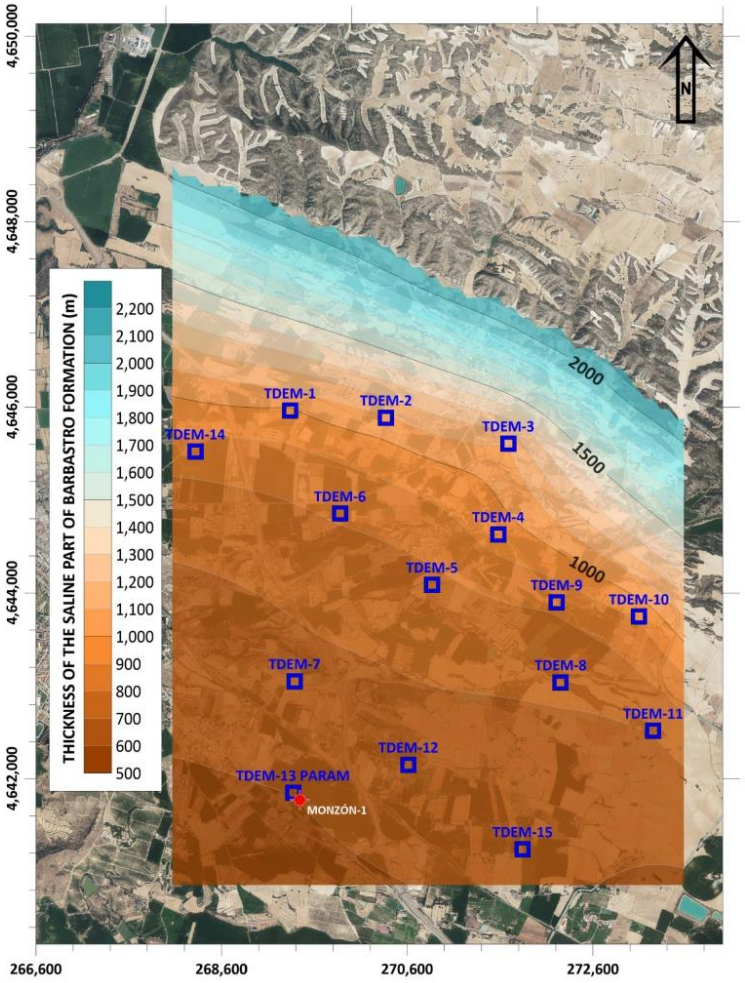

Figure 12. Thickness of the saline-evaporitic Barbastro Formation in the survey area.

No influence on the interpolated surfaces is observed due to the irregular distribution of the TDEM points (Figure 2), presenting a realistic structure in accordance with the accepted geological structural model.

The surfaces generated show the structure of the southern flank of the Barbastro-Balaguer anticline in the survey area, and its affectation of the Barbastro Formation materials, generating a thinning of the formation towards the SW, as can be seen in a 3D representation in Figure 13 created with the commercial Voxler V 4.1.509 3D modelling software (Golden Software LLC).

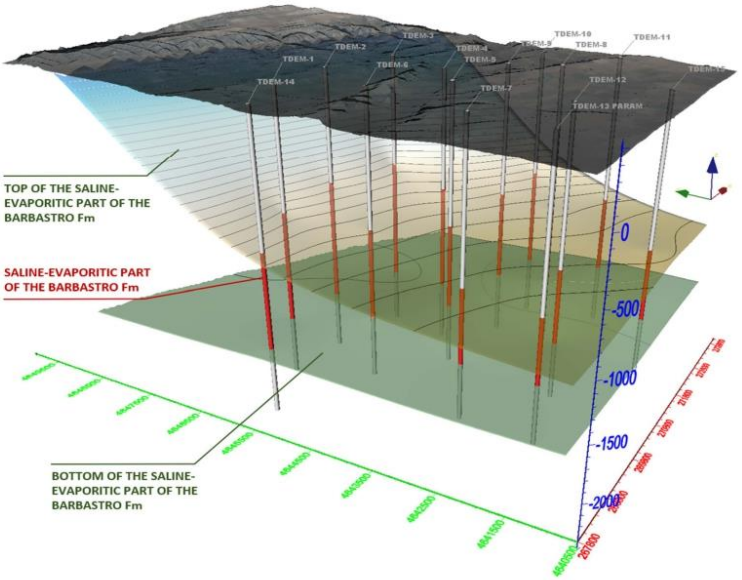

Figure 13. 3D representation of the hanging wall and footwall of the saline-evaporitic part of the Barbastro Formation in the survey area, including TDEM position and results.

6. Conclusions

This study presents the new results of deep time domain electromagnetic soundings (TDEM) study to gain insights into the Barbastro saline-evaporitic formation, affected by the Barbastro-Balaguer Anticline regional structure. The survey was conducted in the southern flank of the anticline in the vicinity of Graus, Spain. Resistivity data were obtained from 15 TDEM survey points with a coincident-loop 600 m × 600 m square configuration, allowing a depth penetration of up to 3.0 km. An initial inversion model was stablished using a thickness and layered parametric constrained model based on the Monzón-1 drilling lithological logging in the rest of the TDEM survey points. The applied methodology allows for an improved detailed geological and structural view of the saline-evaporitic Barbastro Formation affected by the Barbastro-Balaguer Anticline.

The results support the idea that that the Barbastro saline-evaporitic formation presents a complex structure because of the regional anticlinal structure, dipping SW, where the hanging wall shows a variable dip from 40° to close to subhorizontal (distally), ranging from 996 to 1433 m depth, while the footwall shows a close to flat surface between 2001 and 2101 m depth. As a result of the defined structure, the Barbastro saline-evaporitic formation shows a thickness reduction to the SW, ranging from 1103 to 601 m.

Therefore, our study has revealed that the TDEM research method can be an important tool to study saline-evaporitic formations affected by major geological structures, such as the Barbastro-Balaguer Anticline. The new TDEM structural and geoelectrical data would be useful for allocating and designing mining drills at a region of interest for the exploitation of potassium salts in new mining projects.

Author Contributions: Conceptualization, D.P.; methodology, D.P., J.C. and P.C.; software, J.C. and P.C.; validation, D.P., J.C. and P.C.; formal analysis, D.P. and J.C.; investigation, D.P.; resources, D.P., J.C. and P.C.; writing—original draft preparation, D.P.; writing—review and editing, D.P., J.C., P.C. and J.L.H.-P.; visualization, J.C. and J.L.H.-P.; supervision, D.P.; project administration, D.P.; funding acquisition, D.P., J.C. and P.C. All authors have read and agreed to the published version of the manuscript.

Funding: This research received no external funding.

Institutional Review Board Statement: Not applicable.

Informed Consent Statement: Not applicable.

Data Availability Statement: Not available.

Acknowledgments: The authors sincerely appreciate the assistance of reviewers for their comments and support on this paper, especially D. Pedro Carrasco Morillo.

Conflicts of Interest: The authors declare no conflict of interest.

References

1. Goldman, M.; Arad, A.; Kafri, U.; Gilad, D.; Melloul, A. Detection of freshwater/sea-water interface by the time domain electromagnetic (TDEM) method in Israel. In Proceedings of the l0th SWIM, Ghent, Belgium, 16–20 May 1988; pp. 329–344.
2. Ferguson, I.J.; Taylor, W.J.; Schmigel, K. Electromagnetic mapping of saline contamination at an active brine pit. *Can. Geotech. J.* **1996**, *33*, 309–323. [CrossRef]
3. Tartaras, E.; Zhdanov, M.S.; Wada, K.; Saito, A.; Hara, T. Fast imaging of Nojima fault zone TDEM data using S-inversion. In *SEG Technical Program Expanded Abstracts*; Society of Exploration Geophysicists: Houston, TX, USA, 1997; pp. 346–349. [CrossRef]
4. Craven, B.; Rovira, T.; Grammer, T.; Styles, M. The role of geophysics in the discovery and delineation of the Cosmos Nickel Sulphide Deposit, Leinster Area, Western Australia. *Explor. Geophys.* **2000**, *31*, 201–209. [CrossRef]
5. Cummings, D. Transient Electromagnetic Survey of a Landslide and Fault, Santa Susanna Mountains, Southern California. *Environ. Eng. Geosci.* **2000**, *6*, 247–254. [CrossRef]
6. Yechieli, Y.; Kafri, U.; Goldman, M.; Voss, C.I. Factor controlling of configuration of the fresh-saline water interface in the Dead Sea coastal aquifer: Synthesis of TDEM surveys and numerical groundwater modeling. *Hydrogeol. J.* **2001**, *9*, 367–377.
7. Cheng, M.; Yang, D.; Luo, Q. Interpreting Surface Large-Loop Time-Domain Electromagnetic Data for Deep Mineral Exploration Using 3D forward Modeling and Inversion. *Minerals* **2023**, *13*, 34. [CrossRef]
8. Nieto, I.M.; Carrasco García, P.; Sáez Blázquez, C.; Farfán Martín, A.; González-Aguilera, D.; Carrasco García, J. Geophysical Prospecting for Geothermal Resources in the South of the Duero Basin (Spain). *Energies* **2020**, *13*, 5397. [CrossRef]
9. Spies, B.R. Depth of investigation in electromagnetic sounding methods. *Geophysics* **1989**, *54*, 872–888. [CrossRef]
10. Buddo, I.; Shelokhov, I.; Misyurkeeva, N.; Sharlov, M.; Agafonov, Y. Electromagnetic Surveys for Petroleum Exploration: Challenges and Prospects. *Energies* **2022**, *15*, 9646. [CrossRef]
11. Levi, E.; Kafri, U.; Goldman, M. The Delineation of Saline Groundwater Bodies within the Arava Rift Valley, Israel, Using Deep Geoelectromagnetic Measurements. In *AGU Fall Meeting Abstracts*; American Geophysical Union: Washington, DC, USA, 2006.
12. Levi, E.; Goldman, M.; Hadad, A.; Gvirtzman, H. Spatial delineation of groundwater salinity using deep timedomain electromagnetic geophysical measurements: A feasibility study. *Water Resour. Res.* **2008**, *44*, W12404. [CrossRef]
13. Kafri, U.; Goldman, M.; Levi, E. The relationship between saline groundwater within the Arava Rift Valley in Israel and the present and ancient base levels as detected by deep geoelectromagnetic soundings. *Environ. Geol.* **2008**, *54*, 1435–1445. [CrossRef]
14. Kafri, U.; Goldman, M.; Levi, E.; Wollman, S. Detection of Saline Groundwater Bodies between the Dead Sea and the Mediterranean Sea, Israel, Using the TDEM Method and Hydrochemical Parameters. *Environ. Process.* **2014**, *1*, 21–41. [CrossRef]
15. Choukroune, P. The ECORS Pyrenean deep seismic profile reflection data and the overall structure of an orogenic belt. *Tectonics* **1989**, *8*, 23–39. [CrossRef]
16. Muñoz, J.A. The Pyrenees. In *The Geology of Spain*; Gibbons, W., Moreno, T., Eds.; Geological Society: London, UK, 2002; pp. 370–385.
17. Vergés, J.; Millán, H.; Roca, E.; Muñoz, J.A.; Marzo, M.; Cirés, J.; Bezemer, T.D.; Zoetemeijer, R.; Cloetigh, S. Eastern Pyrenees and related foreland basins: Pre-, syn- and post-collisional cristal-scale cross-sections. *Mar. Pet. Geol.* **1995**, *12*, 893–915. [CrossRef]
18. Vergés, J.; Fernàndez, M.; Martínez, A. The Pyrenean orogen: Pre-, syn-, and post-collisional evolution. *J. Virtual Explor.* **2002**, *8*, 55–74. [CrossRef]
19. Teixell, A.; Labaume, P.; Ayarza, P.; Espurt, N.; Blanquat, M.D.S.; Lagabrielle, Y. Crustal structure and evolution of the Pyrenean-Cantabrian belt: A review and new interpretations from recent concepts and data. *Tectonophysics* **2018**, *724–725*, 146–170. [CrossRef]
20. Muñoz, J.A. Evolution of a continental collision belt: ECORS—Pyrenees crustal balanced section. In *Thrust Tectonics*; McClay, K.R., Ed.; Chapman & Hall: London, UK, 1992; pp. 235–246.
21. Burbank, D.W.; Vergés, J.; Muñoz, J.A.; Bentham, P. Coeval hinward- and forward-imbricating thrusting in the south-central Pyrenees, Spain: Timing and rates of shortening and deposition. *Geol. Soc. Am. Bull.* **1992**, *104*, 3–17. [CrossRef]
22. Puigdefàbregas, C.; Muñoz, J.A.; Vergés, J. Thrusting and Foreland Basin Evolution in the Southern Pyrenees. In *Thrust Tectonics*; McClay, K.R., Ed.; Chapman & Hall: London, UK, 1992; pp. 247–254.
23. Cruset, D.; Vergés, J.; Albert, R.; Gerdes, A.; Benedicto, A.; Cantarero, I.; Travé, A. Quantifying deformation processes in the SE Pyrenees using U-Pb dating of fracture-filling calcites. *J. Geol. Soc.* **2020**, *177*, 1186–1196. [CrossRef]

24. Muñoz-López, D.; Cruset, D.; Vergés, J.; Cantarero, I.; Benedicto, A.; Mangenot, X.; Albert, R.; Gerdes, A.; Beranoaguirre, A.; Travé, A. Spatio-temporal variation of fluid flow behavior along a fold: The Bóixols-Sant Corneli anticline (Southern Pyrenees) from U–Pb dating and structural, petrographic and geochemical constraints. *Mar. Pet. Geol.* **2022**, *143*, 105788. [CrossRef]
25. Séguret, M. *Étude Tectonique des Nappes et Séries Décollées de la Partie Centrale du Vesant sud des Pyrénées*; Laboratoire de Géologie Structurale: Montpellier, France, 1972; 155p.
26. Vergés, J.; Martínez, A.; Muñoz, J.A. South Pyrenean fold and thrust belt: The role of foreland evaporitic levels in thrust geometry. In *Thrust Tectonics*; McClay, K., Ed.; Chapman & Hall: London, UK, 1992; pp. 255–264.
27. Sans, M.; Muñoz, J.A.; Vergés, J. Triangle zone and thrust wedge geometries related to evaporitic horizons (Southern Pyrenees). *Can. Pet. Geol. Bull.* **1996**, *4*, 375–384.
28. Costa, E.; Garcés, M.; López-Blanco, M.; Beamud, E.; Gómez-Paccard, M.; Larrasoaña, J.C. Closing and continentalization of the South Pyrenean foreland basin (NE Spain): Magnetochronological constraints. *Basin Res.* **2010**, *22*, 904–917. [CrossRef]
29. Sans, M. From thrust tectonics to diapirism. The role of evaporites in the kinematic evolution of the eastern South Pyrenean front. *Geol. Acta* **2003**, *1*, 239–259.
30. Martínez Peña, B.; Pocoví, A. El amortiguamiento frontal de la estructura de la cobertera surpirenaica y su relación con el anticlinal de Barbastro-Balaguer. *Acta Geol. Hisp.* **1988**, *23*, 81–94.
31. Lanaja, J.M. *Contribución de la Exploración Petrolífera al Conocimiento de la Geología de España*; Instituto Geológico de España: Madrid, Spain, 1987.
32. Muñoz, J.A.; Mencos, J.; Roca, E.; Carrera, N.; Gratacós, O.; Ferrer, O.; Fernàndez, O. The structure of the South-Central-Pyrenean fold and thrust belt as constrained by subsurface data. *Geol. Acta* **2018**, *16*, 439–460.
33. Santolaria, P.; Ayala, C.; Pueyo, E.L.; Rubio, F.M.; Soto, R.; Calvín, P.; Luzón, A.; Rodríguez-Pintó, A.; Oliván, C.; Casas-Sainz, A.M. Structural and Geophysical Characterization of the Western Termination of the South Pyrenean Triangle Zone. *Tectonics* **2020**, *39*, e2019TC005891. [CrossRef]
34. Sáez, A.; Anadón, P.; Herrero, M.J.; Moscariello, A. Variable style of transition between Paleogene fluvial fan and lacustrine systems, southern Pyrenean foreland, NE Spain. *Sedimentology* **2007**, *54*, 367–390. [CrossRef]
35. Pardo, G.; Villena Morales, J. Aportación a la Geología de la región de Barbastro. *Acta Geológica Hispánica* **1979**, *14*, 289–292.
36. Quintares, J. Estudio Sedimentológico y Estratigráfico del Terciario Continental de Los Monegros. Ph.D. Thesis, Universidad de Granada, Granada, Spain, 1969.
37. Crusafont, M.; Riba, O.; Villena, J. *Nota Preliminar Sobre un Nuevo Yacimiento de Vertebrados Aquitanienses en Sta. Cilia (Río Formiga; Provincia de Huesca) y Sus Consecuencias Geológicas, Notas y Comunicaciones IGME*; IGME: Madrid, Spain, 1966; pp. 7–13.
38. Cuenca, G.; Canudo, J.I.; Laplana, C.; Andrés, J.A. Bio y cronoestratigrafía con mamíferos en la Cuenca Terciaria del Ebro: Ensayo de síntesis. *Acta Geol. Hisp.* **1992**, *27*, 127–143.
39. Senz, J.G.; Zamorano, M. Evolución tectónica y sedimentaria durante el Priaboniense superior-Mioceno inferior, en el frente de cabalgamiento de las Sierras Marginales Occidentales. *Acta Geol. Hisp.* **1992**, *27*, 195–209.
40. Luzón, A. Análisis Tectosedimentario de los Materiales Terciarios Continentales del Sector Central de la Cuenca del Ebro (Provincias de Huesca y Zaragoza). Ph.D. Thesis, Universidad de Zaragoza, Zaragoza, Spain, 2001.
41. Stewart, M.; Gay, M.C. Evaluation of transient electromagnetic soundings for deep detection of conductive fluids. *Ground Water* **1986**, *24*, 351–356. [CrossRef]
42. McNeil, J.D. Use of electromagnetic method for groundwater studies. In *Geotechnical and Environmental Geophysics: Review and Tutorial*; SEG Investigations in Geophysics; Ward, S., Ed.; Society of Exploration Geophysicists: Houston, TX, USA, 1990; No. 5; Volume 1, pp. 191–218.
43. Fitterman, D.V.; Stewart, M.T. Transient electromagnetic soundings for groundwater. *Geophysics* **1986**, *53*, 118–128. [CrossRef]
44. Carrasco-García, J.; Porras, D.; Carrasco-García, P.; Herrero-Pacheco, J.; Martín Nieto, I.; Benito-Herrero, J.; Huerta, P. Time-Domain Electromagnetics as a Geophysical Tool in Hydrogeological Exploitation Projects in Mesozoic Formations. *Appl. Sci.* **2022**, *12*, 8655. [CrossRef]
45. Sørensen, K.; Auken, E.; Thomsen, P. TDEM in groundwater mapping—A continuous approach. In *Symposium on the Application of Geophysics to Engineering and Environmental Problems*; Environmental & Engineering Geophysical Society: Denver, CO, USA, 2000; pp. 485–491. [CrossRef]
46. Sørensen, K.; Auken, E.; Christensen, N.B.; Pellerin, L. An integrated approach for hydrogeological investigations: New technology and a case history. *Near-Surf. Geophys.* **2005**, *2*, 583–603.
47. García-Senz, J.; Zamorano-Cáceres, M.; Montes, M.J.; Rico, M. *Mapa Geológico de España 1:50.000, Hoja nº 326 (Monzón) y Memoria*; IGME: Madrid, Spain, 1991; 39p.

Capítulo 3 CONCLUSIONES Y LÍNEAS FUTURAS

3 Conclusiones y líneas futuras

Se recogen en este apartado las principales conclusiones que se han extraído de los trabajos de investigación presentados en los apartados anteriores, así como una propuesta de futuras líneas de investigación que pueden dar continuidad al trabajo existente.

3.1. Conclusiones

Se citan a continuación las principales conclusiones obtenidas en los trabajos de investigación presentados en esta tesis doctoral:

- Las nuevas metodologías de trabajo permiten el análisis de cuerpos o estructuras a gran profundidad, mejorando la resolución espacial y solventando las limitaciones clásicas de estas técnicas de investigación tales como la limitación de aplicabilidad en terrenos con dificultades de acceso, ya sean topográficos o de vegetación, incrementando la productividad y mejorando los costes de ejecución.
- Se demuestra que los enfoques empleados permiten la resolución de problemas geológico-estructurales, así como a estudios sismotectónicos en fallas activas a gran profundidad, habilitando la definición geométrica y cinemática, proporcionando datos esenciales para mejorar la evaluación del potencial sismogénetico de las mismas.
- También se constata la capacidad de aplicación a estudios de geología y minería aplicada, permitiendo la localización del recurso y su geometría lo que define el potencial geológico y minero de la zona permitiendo el diseño y optimización de futuras actividades de investigación y explotación.
- Los avances obtenidos contribuyen de manera significativa al avance en el conocimiento en el campo de la geofísica aplicada y su aplicabilidad a problemas de gran interés académico y profesional.
- Las metodologías aplicadas suponen una clara mejora en la adquisición de datos, mejorando notablemente la cobertura espacial y acceso en entornos con topografía compleja y fuerte vegetación permitiendo la exploración eficiente de grandes áreas.
- Se constata la eficacia de la magnetometría en drones para la exploración de yacimientos minerales. La investigación realizada constituye un notable avance en la investigación minera resultando en una mejora de la exploración mineral y comprensión más profunda de la mineralización de Co-Cu en la sierra de las Estancias definiendo su aplicabilidad en entornos similares, y permitiendo el diseño y desarrollo de futuras actividades de investigación
- El uso del TDEM profundo permite obtener una comprensión más profunda de las características estructurales de la Formación Salina-Evaporítica de Barbastro, incluyendo su profundidad, geometría y estructura interna. El sistema se muestra como una herramienta valida para la realización de estudios con fines estructurales y mineros, permitiendo una mejora notablemente en la exploración minera y su aplicabilidad a otras formaciones geológicas similares.

3.2. Líneas futuras de investigación

A partir de la presente Tesis Doctoral, se abren una serie de líneas de investigación futuras que permitirán la mejora en su aplicabilidad y extensión a la resolución de otros problemas.

En el caso del articulo: Imaging extensional fault systems using deep electrical resistivity tomography: A case study of the Baza fault, Betic Cordillera, Spain. Journal of Applied Geophysics, Volume 202, 2022, 104673, ISSN 0926-9851, https://doi.org/10.1016/j.jappgeo.2022.104673. las futuras líneas de investigación estarán destinadas a:

- Ampliar la metodología de estudio a otras fallas o sistema de fallas ayudando a comprender la posible relación e interacción entre las mismas.
- Evaluación del riesgo sísmico a partir de la integración de los datos DERT con información geofísica de otras técnicas, así como geológica para evaluar la sismicidad de la zona y su impacto potencial en la región.
- Desarrollo de modelos tridimensionales de las estructuras asociadas a la falla de Baza. Esto puede ofrecer una visión más detallada de la geometría del sistema de fallas, obteniendo una comprensión más completa de las implicaciones geológicas y sismotectónicas.
- Ampliación de la metodología de estudio a la investigación de otras fallas con potencial sismotectónico.
- Exploración de Recursos Geotérmicos: Evaluar el potencial geotérmico asociado al sistema de fallas de la región.
- Aplicar la metodología en estudios hidrogeológicos permitiendo determinar la implicación de los sistemas de fractura en los patrones de flujo de aguas subterráneas y estructura de acuíferos profundos, analizando la implicación en la gestión de recursos hídricos.
- Avances Tecnológicos: analizar la potencialidad de la técnica en la obtención de imágenes más profundas a partir de la mejora de la técnica de medida.

En el caso del articulo: Drone Magnetometry in Mining Research. An Application in the Study of Triassic Cu–Co–Ni Mineralizations in the Estancias Mountain Range, Almería (Spain). Drones 2021, 5, 151. https://doi.org/10.3390/drones5040151, se pueden plantear las siguientes líneas de investigación:

- Ampliar la aplicabilidad de la Magnetometría sobre drone a otros contextos geológicos y minerales evaluando la efectividad de la misma en otro tipo de mineralizaciones.
- Estimación Cuantitativa de Recursos Minerales: desarrollar metodologías para la estimación cuantitativa de recursos minerales, empleando de manera conjunta los datos magnetométricos con otros tales como grados de mineralización en sondeos, testificación geofísica, etc.
- Integración de Datos Multisensor: combinar la magnetometría sobre drone con otros sensores tales como el VLF (Very Low Frequency) o imágenes hiperespectrales, de manera que se obtenga una visión más completa de las características geológicas y estructurales relacionadas con los yacimientos minerales, haciendo de esta manera, una exploración más eficiente y completa.
- Ampliar el uso de la magnetometría con drones a otros objetivos como la cartografía geológica, hidrogeología y usos ambientales.

En el caso del estudio: Deep TDEM Study for Structural and Mining Purposes: A Case Study of the Barbastro Saline-Evaporitic Formation, Spain. Appl. Sci. 2023, 13, 6385. https://doi.org/10.3390/app13116385, las futuras líneas de investigación podrían ser:

- Avanzar en el uso del sistema TDEM profundo con fines estructurales y mineros en otros contextos geológicos y mineralizaciones, ayudando a la estimación de recursos y la planificación minera.
- Caracterización estructural profunda en estudios geológicos más allá de la minería.
- Evaluación de Recursos Geotérmicos, dada la capacidad de penetración del sistema, aplicando al estudio y delimitación de formaciones geológicas profundas, así como a sistemas de fracturación susceptibles de albergar potencial geotérmico.

Capítulo 4 REFERENCIAS

Imaging extensional fault systems using deep electrical resistivity tomography: A case study of the Baza fault, Betic Cordillera, Spain

Alfaro, P., Delgado, J., Sanz de Galdeano, C., Galindo- Zaldívar, J., García-Tortosa, F.J., López-Garrido, A.C., López-Casado, C., Marín-Lechado, A., Gil, A., Borque, M.J., 2008. The Baza Fault: a major active extensional fault in the central Betic Cordillera (south Spain). International Journal of Earth Sciences, 97, 1353-1365. DOI: https://doi.org/10.1007/s00531-007-0213-z

Carrasco García, P., 2013. Avance en Técnicas Geofísicas para la caracterización del subsuelo mediante innovación y el uso de herramientas de gestión de información espacial. PhD Thesis, Escuela Politécnica Superior de Ávila. Univ de Salamanca. 523 pp.

Carrier, A., Fischanger, F., Gance, J., Cocchiararo, G., Morelli, G., Lupi, M., 2019. Deep electrical resistivity tomography for the prospection of low-to medium enthalpy geothermal resources. Geophys. J. Int. (2019) 219, 2056–2072. doi: https://doi.org/10.1093/gji/ggz411

Caputo R, Piscitelli S, Oliveto A, Rizzo E, Lapenna V. 2003. High-resolution resistivity tomographies in active tectonic studies. Examples from the Tyrnavos Basin, Greece. J Geodin. 36(1–2):19–35. DOI: https://doi.org/10.1016/S0264-3707(03)00036-X

Castro, J., Martin-Rojas, I., Medina-Cascales, I., García-Tortosa, F.J., Alfaro, P., Insua-Arévalo, J.M., 2018. Active faulting in the central betic Cordillera (Spain): palaeoseismological constraint of the surface-rupturing history of the Baza Fault (central betic Cordillera, Iberian Peninsula). Tectonophysics, 736, 15-30. DOI: https://doi.org/10.1016/j.tecto.2018.04.010

Drahor, M.G., Berge, M.A., 2006. Geophysical investigations of the Seferihisar geotermal area, Western Anatolia, Turkey. Geothermics 35, 302–320. DOI: https://doi.org/10.1016/j.geothermics.2006.04.001

Galindo-Zaldívar, J., González-Lodeiro, F., Jabaloy, A., 1989. Progressive extensional shear structures in a detachment contact in the Western Sierra Nevada (Betic Cordilleras, Spain). Geodinamica Acta, 3(1), 73-85. DOI: https://doi.org/10.1080/09853111.1989.11105175

Galindo-Zaldívar, J., Jabaloy, A., Serrano, I., Morales, J., González- Lodeiro, F., Torcal, F., 1999. Recent and present-day stresses in the Granada Basin (Betic Cordilleras): Example of a late Miocene-present-day extensional basin in a convergent plate boundary. Tectonics, 18(4), 686-702. DOI: https://doi.org/10.1029/1999TC900016

García-Dueñas, V., Balanyá, J.C., Martínez-Martínez, J.M., 1992. Miocene extensional detachments in the outcropping basement of the northern Alboran Basin (Betics) and their tectonic implications. Geo-Marine Letters, 12, 88-95. DOI: https://doi.org/10.1007/BF02084917

García-García, F., Fernández, J., Viseras, C., Soria, J.M., 2006. Architecture and sedimentary facies evolution in a delta stack controlled by fault growth (Betic Cordillera, southern Spain, late Tortonian). Sedimentary Geology, 185(1-2), 79-92. DOI: https://doi.org/10.1016/j.sedgeo.2005.10.010

García Tortosa, F.J., Alfaro, P., Galindo Zaldívar, J., Gibert, L., López Garrido, A.C., Sanz de Galdeano, C., Ureña, M., 2008. Geomorphologic evidence of the active Baza Fault (Betic Cordillera, South Spain). Geomorphology, 97(3-4), 374-391. DOI: https://doi.org/10.1016/j.geomorph.2007.08.007

García-Tortosa, F.J., Alfaro, P., Galindo Zaldívar, J., Sanz de Galdeano, C., 2011. Glacis geometry as a geomorphic marker of recent tectonics: the Guadix-Baza Basin (South Spain). Geomorphology, 125(4), 517-529. DOI: https://doi.org/10.1016/j.geomorph.2010.10.021

Gibert, L., Sanz de Galdeano, C., Alfaro, P., López Garrido A.C., 2005. Seismic-induced slump in Early Pleistocene deltaic deposits of the Baza Basin (SE Spain). Sedimentary Geology 179(3):279-294, doi: https://doi.org/10.1016/j.sedgeo.2005.06.003

Haberland, C., Giber, L., José Jurado, M., Stiller, M., Baumann- Wilke, M., Scott, G., Mertz, D.F., 2017. Architecture and tectono-stratigraphic evolution of the intramontane Baza Basin (Bétics, SE-Spain): Constraints from seismic imaging. Tectonophysics, 709, 69-84. DOI: https://doi.org/10.1016/j.tecto.2017.03.022

Hansen, C., 1992. Analysis of Discrete Ill-Posed Problems by Means of the L-Curve. SIAM Rev., 34(4), 561–580. DOI: https://doi.org/10.1137/1034115

Jabaloy, A., Galindo-Zaldívar, J., Gonzalez-Lodeiro, F., and Aldaya, F., 1995. Main features of the deep structure of the central Bétic Cordillera (SE Spain) from the ESCI-Béticas deep seismic reflection profiles. Rev. Soc. Geol. España, 8 (4), pp. 461 – 476.

Kolawole F, Atekwana EA, Laó-Dávila DA, Abdelsalam MG, Chindandali PR, Salima J, Kalindekafe L. 2018. High-resolution electrical resistivity and aeromagnetic imaging reveal the causative fault of the 2009 Mw 6.0 Karonga, Malawi earthquake. Geophys J Int. 213(2): 1412–1425. DOI: https://doi.org/10.1093/gji/ggy066

Lines, L.R. and Treitel, S. (1984) Tutorial: A Review of Least-Squares Inversion and Its Application to Geophysical Problems. Geophysical Prospecting, 32, 159-186. DOI: http://dx.doi.org/10.1111/j.1365-2478.1984.tb00726.x

Locke, M.H. 2012. Tutorial: 2-D and 3-D Electrical Imaging Surveys. Geotomo Software, Malaysia, 168 p

Locke, M.H. 2019. Rapid 2-D Resistivity & IP inversión using the least-squares method. Geotomo Software, Malaysia, 146 p

Loke, M., Dahlin T., 2002. A comparison of the Gauss–Newton and quasi-Newton methods in resistivity imaging inversion. Journal of Applied Geophysics. Volume 49, Issue 3, March 2002, Pages 149-162. DOI: https://doi.org/10.1016/S0926-9851(01)00106-9

Martínez-Solares, J.M., Mezcua, J., 2002. Catálogo sísmico de la Península Ibérica (880 AC-1900). Madrid (Spain), Instituto Geográfico Nacional (IGN), Monografía nº 18, 254pp.

Medina-Cascales, I., Martin-Rojas, I., García-Tortosa, F.J., Peláez, J.A., Alfaro, P., 2020. Geometry and kinematics of the Baza Fault (central Betic Cordillera, South Spain): insights into its seismic potential. Geologica Acta, Vol.18.11, 1-25. DOI: https://doi.org/10.1344/GeologicaActa2020.18.11

Nocquet, J-M., 2012. Present-day kinematics of the Mediterranean: A comprehensive overview of GPS results. Tectonophysics, 579, 220-242. DOI: https://doi.org/10.1016/j.tecto.2012.03.037

Orozco, M., Alonso-Chaves, F.M., 2002. Estructuras de colapso extensional en el Dominio de Alborán. In: Orozco, M. (ed.). Región de La Axarquía-Sierra Tejeda (provincias de Málaga y Granada). XIV Reunión de

la Comisión de Tectónica de la Sociedad Geológica de España, Guía de Campo, Granada, 120pp. ISBN: 84-607-5712-9

Pace, B., Visini, F., Peruzza, L., 2016. FiSH: MATLAB tools to turn fault data into Seismic-Hazard Models. Seismological Research Letters, 87(2A), 374-386. DOI: https://doi.org/10.1785/0220150189

Palano, M., Gonzalez, P.J., Fernández, J., 2013. Strain and stress fields along the Gibraltar Orogenic Arc: Constraints on active geodynamics. Gondwana Research, Vol 23, Issue 3, 1071-1088. https://doi.org/10.1016/j.gr.2012.05.021

Palano, M., Gonzalez, P.J., Fernández, J., 2015. The Diffuse Plate boundary of Nubia and Iberia in the Western Mediterranean: Crustal deformation evidence for viscous coupling and fragmented lithosphere. Earth and Planetary Science Letters, Volume 430, 439-447. https://doi.org/10.1016/j.epsl.2015.08.040

Pérez-Peña, J.V.; Azañón, J.M.; Galve, J.P.; Booth-Rea, G.; de Lis Mancilla, F.; Stich, D.; Morales, j.; 2018. A post-Tortonian pull-apart basin controlled by lithosphere tearing processes at a STEP boundary of the Gibraltar Arc Suduction System. 20th EGU General Assembly, EGU2018, Proceedings from the conference held 4-13 April, 2018 in Vienna, Austria, p.15695. https://ui.adsabs.harvard.edu/abs/2018EGUGA..2015695P/abstract

Robain, H. & Bobachev, A., 2002. 'X2IPI Tool box for 2D DCand DC-IP measurements'. Available at: http://geophys.geol.msu.ru/x2ipi/x2ipi.html#boba

Rizzo, E., Giampaolo, V (2019) New deep electrical resistivity tomography in the High Agri Valley basin (Basilicata, Southern Italy), Geomatics, Natural Hazards and Risk, 10:1, 197-218, DOI: https://doi.org/10.1080/19475705.2018.1520150

Rodríguez-Fernandez, J; Azor, A; Azañón, J; 2012. The Betic Intramontane Basins (SE Spain): Stratigraphy, Subsidence, and Tectonic History. In book: Tectonics of Sedimentary Basins (pp.461-479). DOI: https://doi.org/10.1002/9781444347166.ch23

Sanz de Galdeano, C., Vera, J.A., 1992. Stratigraphic record and palaeogeographical context of the Neogene basins in the Betic Cordillera, Spain. Basin Research. https://doi.org/10.1111/j.1365-2117.1992.tb00040.x

Sanz de Galdeano, C., Vera, J.A., 2007. Stratigraphic record and palaeogeographical context of the Neogene basins in the Bétic Cordillera, Spain. Basin Research 4, 21–36. DOI: https://doi.org/10.1111/j.1365-2117.1992.tb00040.x

Sanz de Galdeano, C., García-Tortosa, F.J., Peláez, J.A., Alfaro, P., Azañón, J.M., Galindo-Zaldívar, J., López-Casado, C., López- Garrido, A.C., Rodríguez-Fernández, J., Ruano, P., 2012. Main active faults in the Granada and Guadix-Baza Basins (Betic Cordillera). Journal of Iberian Geology, 38(1), 209-223. DOI: http://dx.doi.org/10.5209/rev_JIGE.2012.v38.n1.39215

Sanz de Galdeano, C., Azañón, J.M., Cabral, J., Ruano, P., Alfaro, P., Canora, C., Ferrater, M., García-Tortosa, F., Mayordomo, J., Gràcia, E., Insua-Arévalo, J.M., Jiménez, A., Lacan, P., Marín-Lechado, C., Martín-Banda, R., Martín-González, F., Martinez-Diaz, J.J., Martin-Rojas, I., Masana, E., Simón, J.L., 2020. Active Faults in Iberia. Quesada, C., Oliveira, J. (eds.). The Geology of Iberia: A Geodynamic Approach. Cham, Regional Geology Reviews, Springer, 33-75.

Scholz, C.H., 2019. The mechanics of Earthquakes and Faulting. 3rd Edition, Cambridge, Cambridge University Press, 493pp.

Soria, J.M., Viseras, C., and Fernandez, J., (1998). Late Miocene–Pleistocene tectono-sedimentary evolution and subsidence history of the central Betic Cordillera (Spain): A case study in the Guadix intramontane basin. Geological Magazine, 135(4), 565-574. doi: https://doi.org/10.1017/S0016756898001186

Steeples DW. 2001. Engineering and environmental geophysics at the millenium. Geophysics. 66(1):31–35. DOI: https://doi.org/10.1190/1.1444910.

Storz, H., Storz, W., Jacobs, F. 2000. Electrical resistivity tomography to investigate geological structures of the earth's upper crust. Geophysical Prospecting, 2000, 48, 455-471. DOI: https://doi.org/10.1046/j.1365-2478.2000.00196.x

Suzuki K, Toda S, Kusunoki K, Fujimitsu Y, Mogi T, Jomori A. 2000. Case studies of electrical and electromagnetic methods applied to mapping active faults beneath the thick quaternary. Developments in Geotechnical Engineering. 84, 29-45. DOI: https://doi.org/10.1016/S0165-1250(00)80005-X

Telford, W.M, L.P. Geldart, and R.E. Sheriff. 1990. Applied geophysics. 2nd ed. Cambridge Univ. Press, Cambridge, UK. DOI: https://doi.org/10.1017/CBO9781139167932

Troiano, A., Isaia, R., Di Giuseppe, M. G., Tramparulo, D. A., Vitale, S.. 2019. Deep electrical Resistivity Tomography for a 3D picture of the most active sector of Campi Flegrei caldera. Scientific Reports, (2019) 9:15124. https://doi.org/10.1038/s41598-019-51568-0

Vera, J.A., 1970a. Facies del Plioceno de la Depresión de Guadix- Baza. Cuadernos Geológicos de la Universidad de Granada, 1, 23-25.

Vera, J.A., 1970b. Estudio estratigráfico de la Depresión de Guadix-Baza. Boletín del Instituto Geológico y Minero de España, 81, 429-462.

Wesnousky, S.G., 2008. Displacement and Geometrical Characteristics of Earthquake Surface Ruptures: Issues and Implications for Seismic-Hazard Analysis and the Process of Earthquake Rupture. Bulletin of the Seismological Society of America, 98(4), 1609-1632. DOI: https://doi.org/10.1785/0120070111

Drone Magnetometry in Mining Research. An Application in the Study of Triassic Cu–Co–Ni Mineralizations in the Estancias Mountain Range, Almería (Spain)

Giordan, D.; Adams, M.S., Aicardi, I. et al. The use of unmanned aerial vehicles (UAVs) for engineering geology applications. Bull Eng Geol Environ 2020, 79, 3437–3481. https://doi.org/10.1007/s10064-020-01766-2

Aleshin, I.M.; Ivanov, S.D.; Koryagin, V.N. et al. Review on the Use of Light Unmanned Aerial Vehicles in Geological and Geophysical Research. Seism. Instr. 2020, 56, 509–515. https://doi.org/10.3103/S0747923920050035

Parvar, K.; Braun, A.; Layton-Matthews, D. and Burns, M. UAV magnetometry for chromite exploration in the Samail ophiolite sequence, Oman. Journal of Unmanned Vehicle Systems 2018, 6, 57–69.

Shahmoradi, J.; Talebi, E.; Roghanchi, P.; Hassanalian, M. A comprehensive review of applications of drone technology in the mining industry. Drones 2020, 4, 34; DOI: 10.3390/drones4030034.

Malehmir, A.; Dynesius, L.; Paulusson, K.; Paulusson, A.; Johansson, H.; Bastani, M.; Wedmark, P.; Marsden, P. The potential of rotary-wing UAV-based magnetic surveys for mineral exploration: A case study from central Sweden. Leading Edge 2017, 36, 552–557.

Park, S. and Choi, Y., 2020, Applications of unmanned aerial vehicles in mining from exploration to reclamation: A review: Minerals 2020, 10, 1–32, doi:10.3390/min10080663.

Kim, B.; Lee, S.; Park, G.; and Cho, S.-J. Development of an unmanned airship for magnetic exploration. Exploration Geophysics 2020, 1–6, doi:10.1080/08123985.2020.1827949.

Le Maire, P.; Bertrand, L.; Munschy, M.; Diraison, M.; and Géraud, Y. Aerial magnetic mapping with an unmanned aerial vehicle and a fluxgate magnetometer: a new method for rapid mapping and upscaling from the field to regional scale: Geophysical Prospecting 2020, 68, 2307–2319, doi:10.1111/1365-2478.12991.

Schmidt, V.; Becken, M.; and Schmalzl, J. A UAV-borne magnetic survey for archaeological prospection of a Celtic burial site. First Break 2020, 38, 61–66, doi:10.3997/1365-2397.fb2020061.

Alex, N.; Timothy, S.d.S. A UAV-based magnetic survey method to detect and identify orphaned oil and gas wells. Lead. Edge 2019, 38 (6), 447–452.

Hammack, R.W.; Veloski, G.A.; Lowe, R.; Zorn, A.; Wylie, L.; Schlagenhauf, M. Using Drone-Mounted Geophysical Sensors to Map Legacy Oil and Gas Infrastructure. National Energy Technology Laboratory (NETL), Pittsburgh, PA, Morgantown, WV (United States). Medium: ED. 2020.

de Smet, T.S.; Nikulin, A.; Romanzo, N.; Graber, N.; Dietrich, C.; Puliaiev, A. Successful application of drone-based aeromagnetic surveys to locate legacy oil and gas wells in Cattaraugus county, New York. Appl. Geophys 2021, 186, 104250.

Everett, M. Near-Surface Applied Geophysics. Cambridge University Press, Cambridge, 2013

Parvar, K. Development and evaluation of unmanned aerial vehicle (UAV) magnetometry systems. Master of Applied Science thesis, Department of Geological Sciences and Geological Engineering, Queen's University, Kingston, Ontario, Canada, 2016; 1–141.

Parshin, A.; Morozov, V.; Blinov, A.; Kosterev, A. and Budyak, A. Low-altitude geophysical magnetic prospecting based on multirotor UAV as a promising replacement for traditional ground survey. Geo-spatial Information Science 2018, 21, 1-8. 10.1080/10095020.2017.1420508.

Jackisch, R.; Madriz, Y.; Zimmermann, R.; Pirttijärvi, M.; Saartenoja, A.; Heincke, B.H.; Salmirinne, H.; Kujasalo, J.-P.; Andreani, L., and Gloaguen, R. Drone-borne hyperspectral and magnetic data integration: Otanmäki Fe-Ti-V deposit in Finland. Remote Sensing 2019, 11, doi:10.3390/rs11182084.

Empresa Nacional Adaro de investigaciones Mineras (ADARO).1987. Programa de investigación sistemática de recursos. Zona Sureste. Sierra de Las Estancias.

IGME MAGNA 1Instituto Geológico y Minero de España (IGME), 1972. Hoja de Chirivel (973). Mapa Geológico de España (E. 1:50.000), 46 pags.

IGME MAGNA 2Instituto Geológico y Minero de España (IGME), 1972. Hoja de Cantoria (995). Mapa Geológico de España (E. 1:50.000), 51 pags.

EXCO MINING SL. Informe Geológico y minero del Permiso de Investigación Burán, Sierra de Oria, Almería. Informe interno no publicado, 2019.

EXCO MINING SL. Análisis geoquímico y petrográfico de muestras superficiales tomadas en el Permiso de Investigación Burán, Almería. Informe interno no publicado. 2020.

Hernandez-Lopez, D.; Felipe-Garcia, B.; Gonzalez-Aguilera, D.; Arias-Perez, B. An automatic approach to UAV flight planning and control for photogrammetric applications. Photogrammetric Engineering & Remote Sensing 2013, 79 (1), 87-98.

Cunningham, M.; Samson, C.; Wood, A. and Cook, I. Aeromagnetic Surveying with a Rotary-Wing Unmanned Aircraft System: A Case Study from a Zinc Deposit in Nash Creek, New Brunswick, Canada. Pure and Applied Geophysics, 2018, 175 (9). DOI:10.1007/s00024-017-1736-2.

Walter, C.A.; Braun, A.; Fotopoulos, G. Impact of three-dimension6al attitude variations of an unmanned aerial vehicle magnetometry system on magnetic data quality. Geophysical Prospecting 2019, 67(2), 465-479, DOI: 10.1111/1365-2478.12727.

Jirigalatu, J.; Krishna, V.; Silva, E.; Døssing, A. Experiments on magnetic interference for a portable airbone magnetometry system using a hybrid unmanned aerial vehicle (UAV). Geoscientific Instrumentation Methods and Data Systems 2020, 10(1), 25-34 DOI:10.5194/gi-10-25-2021.

Telford, W.M.; Geldart, L.R. and Sheriff, R.E. Applied Geophysics 2nd ed. 1990. Cambridge: Cambridge University Press, 770 pp.

Briggs, I.C. Machine contouring using minimum curvature. Geophysics 1974, 39, 39–48. DOI: 10.1190/1.1440410.

Lee, M. and Morris, W. Quality assurance of aeromagnetic data using lineament analysis. Exploration Geophysics 2013, 44(2), 104. doi:10.1071/eg12034.

Nabighian, M.N.; Grauch, V.J.S.; Hansen, R.O.; LaFehr, T.R.; Li, Y.; Peirce, J.W.; Phillips, J.D.; and Ruder, M.E. The historical development of the magnetic method in exploration. Geophysics 2005, 70(6), 33–61. https://doi.org/10.1190/1.2133784.

MacLeod, I.N. and Ellis, R.G. Magnetic vector inversion, a simple approach to the challenge of varying direction of rock magnetization: Australian Society of Exploration Geophysicists, 2013, v. 1.

Deep TDEM Study for Structural and Mining Purposes: A Case Study of the Barbastro Saline-Evaporitic Formation, Spain

Goldman et al., 1989. M. Goldman, A. Arad, U. Kafri, D. Gilad, A. Melloul. Detection of freshwater/sea-water interface by the time domain electromagnetic (TDEM) method in Israel. Proc. l0th SWIM, Ghent, 1988 (1989), pp. 329-344

Ferguson, I. J., Taylor, W. J., & Schmigel, K. (1996). Electromagnetic mapping of saline contamination at an active brine pit. Canadian Geotechnical Journal, 33(2), 309–323. doi:10.1139/t96-009

Tartaras, E.; Zhdanov, M. S.; Wada, K.; Saito, A.; and Hara, T, (1997), "Fast imaging of Nojima fault zone TDEM data using S - inversion," SEG Technical Program Expanded Abstracts: 346-349. https://doi.org/10.1190/1.1885902

Craven B., Rovira T., Grammer T. and Styles M., 2000. The role of geophysics in the discovery and delineation of the Cosmos Nickel Sulphide Deposit, Leinster Area, Western Australia Exploration Geophysics 31(1-2) 201- 209 https://doi.org/10.1071/EG00201

Cummings D., 2000. Transient Electromagnetic Survey of a Landslide and Fault, Santa Susanna Mountains, Southern California Environmental and Engineering Geoscience 6 (3) 247-254.

Yechieli, Y.; Kafri, U.; Goldman, M.; Voss, C.I.; 2001. Factor controlling of configuration of the fresh-saline water interface in the Dead Sea coastal aquifer: Synthesis of TDEM surveys and numerical groundwater modeling. Hydrogeol. J. 2001, 9, 367–377

Cheng, M.; Yang, D.; Luo, Q. Interpreting Surface Large-Loop Time-Domain Electromagnetic Data for Deep Mineral Exploration Using 3D Forward Modeling and Inversion. Minerals 2023, 13, 34. https://doi.org/10.3390/min13010034

Nieto, I.M.; Carrasco García, P.; Sáez Blázquez, C.; Farfán Martín, A.; González-Aguilera, D.; Carrasco García, J. Geophysical Prospecting for Geothermal Resources in the South of the Duero Basin (Spain). Energies 2020, 13, 5397. https://doi.org/10.3390/en13205397

Brian R. Spies, (1989), "Depth of investigation in electromagnetic sounding methods," GEOPHYSICS 54: 872-888. https://doi.org/10.1190/1.1442716

Buddo, I.; Shelokhov, I.; Misyurkeeva, N.; Sharlov, M.; Agafonov, Y. Electromagnetic Surveys for Petroleum Exploration: Challenges and Prospects. Energies 2022, 15, 9646. https://doi.org/10.3390/en15249646

Antiguo 9Levi, E., Kafri, Uri and Goldman M. (2006). The Delineation of Saline Groundwater Bodies Within the Arava Rift Valley, Israel, Using Deep Geoelectromagnetic Measurements. AGU Fall Meeting Abstracts

Levi, E., Goldman M., A. Hadad, and H. Gvirtzman (2008), Spatial delineation of groundwater salinity using deep timedomain electromagnetic geophysical measurements: A feasibility study,Water Resour. Res.,44, W12404,doi:10.1029/2007WR006459

Kafri, U., Goldman, M. & Levi, E. The relationship between saline groundwater within the Arava Rift Valley in Israel and the present and ancient base levels as detected by deep geoelectromagnetic soundings. Environ Geol 54, 1435–1445 (2008). https://doi.org/10.1007/s00254-007-0924-2

Kafri, U., Goldman, M. & Levi, E & Wollman, Stuart & Goldman, M & Levi, E. (2014). Detection of Saline Groundwater Bodies between the Dead Sea and the Mediterranean Sea, Israel, Using the TDEM Method and Hydrochemical Parameters. Environmental Processes. 1. 21-41. 10.1007/s40710-014-0001-2.

Choukroune, P. and team, E., 1989. The ECORS Pyrenean deep seismic profile reflection data and the overall structure of an orogenic belt. Tectonics, 8: 23-39

Muñoz, J.A., 2002. The Pyrenees. In: W. Gibbons and T. Moreno (Editors), The Geology of Spain. Geological Society, London, pp. 370-385.

Vergés, J., Millán, H., Roca, E., Muñoz, J.A., Marzo, M., Cirés, J., Bezemer, T.D., Zoetemeijer, R. and Cloetigh, S., 1995. Eastern Pyrenees and related foreland basins: pre-, syn- and post-collisional cristal-scale cross-sections. Marine and Petroleum Geology, 12(8): 893-915.

Vergés, J., Fernàndez, M. and Martínez, A., 2002. The Pyrenean orogen: pre-, syn-, and post-collisional evolution. In: G. Rosenbaum and G. Lister (Editors), Reconstruction of the evolution of the Alpine-Himalayan Orogen. Journal of the Virtual Explorer, pp. 55-74.

Teixell, A., Labaume, P., Ayarza, P., Espurt, N., Blanquat, M.d.S. and Lagabrielle, Y., 2018. Crustal structure and evolution of the Pyrenean-Cantabrian belt: A review and new interpretations from recent concepts and data. Tectonophysics, 724-725: 146-170.

Muñoz, J.A., 1992. Evolution of a continental collision belt: ECORS–Pyrenees crustal balanced section. In: K.R. McClay (Editor), Thrust Tectonics. Chapman & Hall, London, pp. 235-246.

Burbank, D.W., Vergés, J., Muñoz, J.A. and Bentham, P., 1992. Coeval hinward- and forward-imbricating thrusting in the south-central Pyrenees, Spain: Timing and rates of shortening and deposition. Geological Society of America Bulletin, 104: 3-17.

Puigdefàbregas, C., Muñoz, J.A. and Vergés, J., 1992. Thrusting and Foreland Basin Evolution in the Southern Pyrenees. In: K.R. McClay (Editor), Thrust Tectonics. London, Chapman & Hall, pp. 247-254.

Cruset, D., Vergés, J., Albert, R., Gerdes, A., Benedicto, A., Cantarero, I. and Travé, A., 2020. Quantifying deformation processes in the SE Pyrenees using U-Pb dating of fracture-filling calcites. Journal of the Geological Society, 177: 1186-1196.

Muñoz-López, D., Cruset, D., Vergés, J., Cantarero, I., Benedicto, A., Mangenot, X., Albert, R., Gerdes, A., Beranoaguirre, A. and Travé, A., 2022. Spatio-temporal variation of fluid flow behavior along a fold: The Bóixols-Sant Corneli anticline (Southern Pyrenees) from U–Pb dating and structural, petrographic and geochemical constraints. Marine and Petroleum Geology, 143: 105788.

Séguret, M., 1972. Étude tectonique des nappes et séries décollées de la partie centrale du vesant sud des Pyrénées. Pub. USTELA, sér, Geol. Struct. n.2, Montpellier, 155 pp.

Vergés, J., Martínez, A. and Muñoz, J.A., 1992. South Pyrenean fold and thrust belt: The role of foreland evaporitic levels in thrust geometry. In: K. McClay (Editor), Thrust Tectonics. London, Chapman & Hall, pp. 255-264.

Sans, M., Muñoz, J.A. and Vergés, J., 1996. Triangle zone and thrust wedge geometries related to evaporitic horizons (Southern Pyrenees). Canadian Petroleum Geology Bulletin, 4(2): 375-384.

Costa, E., Garcés, M., López-Blanco, M., Beamud, E., Gómez-Paccard, M. and Larrasoaña, J.C., 2010. Closing and continentalization of the South Pyrenean foreland basin (NE Spain): magnetochronological constraints. Basin Research, 22(6): 904-917.

Sans, M., 2003. From thrust tectonics to diapirism. The role of evaporites in the kinematic evolution of the eastern South Pyrenean front. Geologica Acta, 1(3): 239-259.

Martínez Peña, Begoña; Pocoví Juan, A. El amortiguamiento frontal de la estructura de la cobertera surpirenaica y su relación con el anticlinal de Barbastro-Balaguer. Acta geológica hispánica, 1988, Vol. 23, Núm. 2, p. 81-94.

Lanaja, J.M., 1987. Contribución de la exploración petrolífera al conocimiento de la geología de España, Instituto Geológico de España.

Muñoz, J.A., Mencos, J., Roca, E., Carrera, N., Gratacós, O., Ferrer, O. and Fernàndez, O., 2018. The structure of the South-Central-Pyrenean fold and thrust belt as constrained by subsurface data. Geologica Acta, 16(4): 439-460.

Santolaria, P., Ayala, C., Pueyo, E.L., Rubio, F.M., Soto, R., Calvín, P., Luzón, A., Rodríguez-Pintó, A., Oliván, C. and Casas-Sainz, A.M., 2020. Structural and Geophysical Characterization of the Western Termination of the South Pyrenean Triangle Zone. Tectonics, 39(8): e2019TC005891.

Sáez, A., Anadón, P., Herrero, M.J. and Moscariello, A., 2007. Variable style of transition between Paleogene fluvial fan and lacustrine systems, southern Pyrenean foreland, NE Spain. Sedimentology, 54: 367-390.

Pardo, G.; Villena Morales, J.. «Aportación a la Geología de la región de Barbastro». Acta geológica hispánica, 1979, Vol. 14, Núm. 1, p. 289-292,

Quintares, J., 1969. Estudio sedimentológico y estratigráfico del Terciario continental de Los Monegros, PhD Thesis. Granada: Universidad de Granada.

Crusafont, M., Riba, O. and Villena, J., 1966. Nota preliminar sobre un nuevo yacimiento de vertebrados aquitanienses en Sta. Cilia (río Formiga; Provincia de Huesca) y sus consecuencias geológicas, Notas y Comunicaciones IGME, Marid, pp. 7-13.

Cuenca, G., Canudo, J.I., Laplana, C. and Andrés, J.A., 1992. Bio y cronoestratigrafía con mamíferos en la Cuenca Terciaria del Ebro: ensayo de síntesis. Acta Geologica Hispanica, 27(1-2): 127-143.

Senz, J.G. and Zamorano, M., 1992. Evolución tectónica y sedimentaria durante el Priaboniense superior - Mioceno inferior, en el frente de cabalgamiento de las Sierras Marginales Occidentales. Acta Geologica Hispanica, 27(1-2): 195-209.

Luzón, A., 2001. Análisis Tectosedimentario de los materiales Terciarios continentales del sector central de la Cuenca del Ebro (provincias de Huesca y Zaragoza), PhD Thesis. Zaragoza: Universidad de Zaragoza.

Stewart M., Gay M.C. (1986) Evaluation of transient electromagnetic soundings for deep detection of conductive fluids. Ground Water 24(3):351–356

McNeil J.D. (1990). Use of electromagnetic method for groundwater studies. In: Ward S (ed) Geotechnical and environmental geophysics. Review and Tutorial, SEG investigations in Geophysics No. 5, vol 1. Tulsa, pp 191–218

Fitterman D.V., Stewart M.T. (1986). Transient electromagnetic soundings for groundwater. Geophysics 53:118–128

Carrasco García, P., 2013. Avance en Técnicas Geofísicas para la caracterización del subsuelo mediante innovación y el uso de herramientas de gestión de información espacial. PhD Thesis, Escuela Politécnica Superior de Ávila. Univ de Salamanca. 523 pp.

Carrasco-García, J., Porras, D., Carrasco-García, P., Herrero-Pacheco, J., Martín Nieto, I., Benito-Herrero, J. and Huerta, P.. (2022). Time-Domain Electromagnetics as a Geophysical Tool in Hydrogeological Exploitation Projects in Mesozoic Formations. Applied Sciences. 12. 8655. 10.3390/app12178655.

Sørensen, K., Auken, E., Thomsen, P., 2000. TDEM in groundwater mapping- a continuous approach, in: Symposium on the Application of Geophysics to Engineering and Environmental Problems. pp. 485-491. https://doi.org/10.4133/1.2922780

Sørensen, K., Auken, E., Christensen, N.B., Pellerin, L., 2005. An integrated approach for hydrogeological investigations: New technology and a case history. Near-Surface Geophys. Vol. 2 Appl. Case Hist. 583 – 603.

García-Senz, J., Zamorano-Cáceres, M., Montes, M. J., y Rico, M. (1991). Mapa Geológico de España 1:50.000, hoja nº 326 (Monzón) y memoria. IGME. 39 p.

Capítulo 5 ÍNDICES DE CALIDAD DE LAS REVISTAS

4.1 Índices de calidad de las revistas

Se indican a continuación los índices de calidad de las revistas en las que se ha realizado las publicaciones.

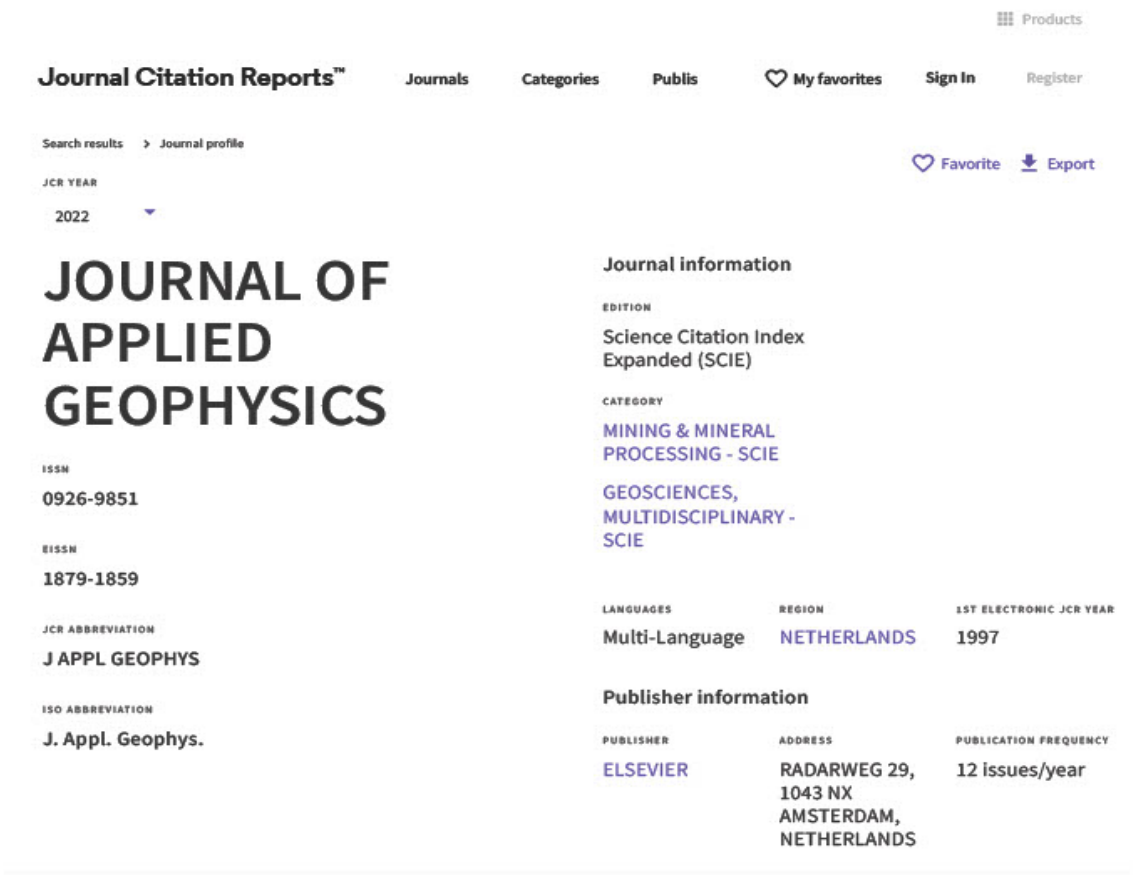

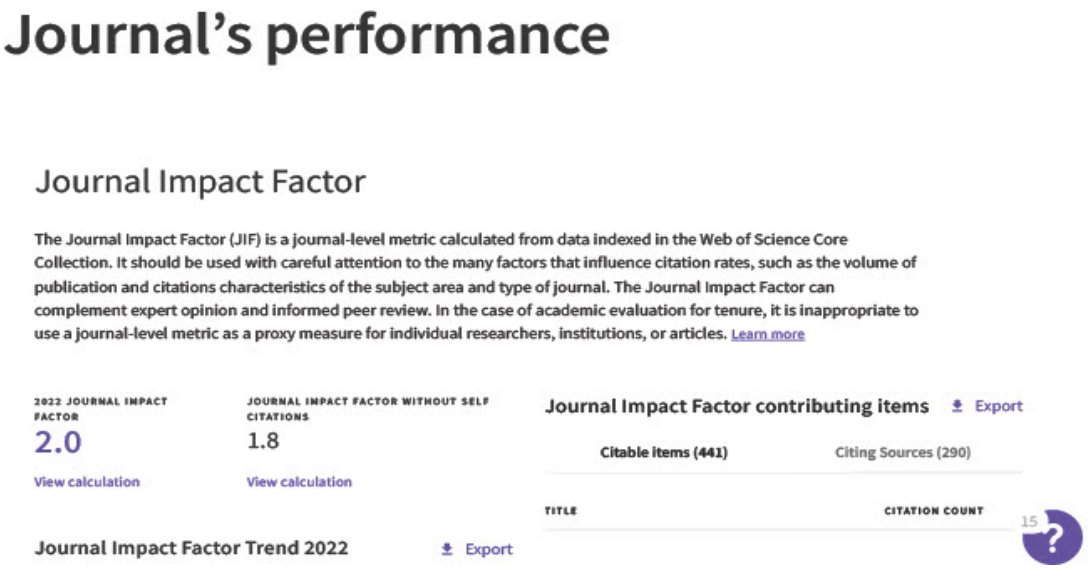

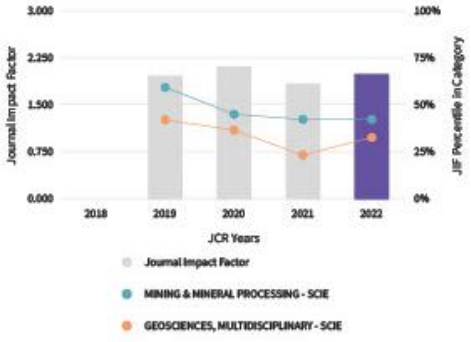

View all years

A challenging archaeo-geophysical	11	˅
Comparison of novel semi-airborne electromagnetic data with multi-scale…	11	˅
Research on the overburden deformation and migration law in dee…	11	˅
Shear modulus prediction of embedded pressurized salt layers and pinpointin…	11	˅
Volcanic lithology identification based on parameter-optimized GBDT…	11	˅
A new approach for porosity and permeability prediction from well logs…	10	˅
Gravity applications to groundwater storage variations of the Nile Delta…	10	˅
The influence of minerals on the mechanism of microwave-induced…	10	˅
Application of combined electrical resistivity tomography (ERT) and seis…	9	˅
De-noising low-frequency magnetotelluric data using…	9	˅

View All in Web of Science

Journal Citation Indicator (JCI)

Export

0.59

The Journal Citation Indicator (JCI) is the average Category Normalized Citation Impact (CNCI) of citable items (articles & reviews) published by a journal over a recent three year period. The average JCI in a category is 1. Journals with a JCI of 1.5 have 50% more citation impact than the average in that category. It may be used alongside other metrics to help you evaluate journals. Learn more

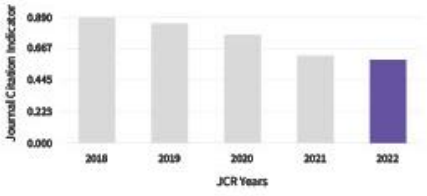

View all years

Total Citations

Export

7,529

The total number of times that a journal has been cited by all journals included in the database in the JCR year. Citations to journals listed in JCR are compiled annually from the JCR years combined database, regardless of which JCR edition lists the journal.

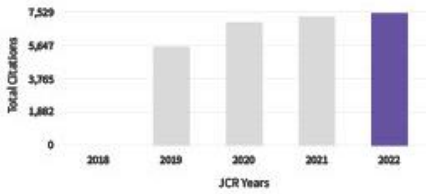

View all years

Citation distribution

Export

The Citation Distribution shows the frequency with which items published in the year or two years prior were cited in the JCR data year (i.e., the component of the calculation of the JIF). The graph has similar functionality as the JIF Trend graph, including hover-over data descriptions for each data point, and an interactive legend where each data element's legend can be used as a toggle. You can view Articles, Reviews, or Non-Citable (other) items to the JIF numerator. Learn more

ARTICLE CITATION MEDIAN
1

REVIEW CITATION MEDIAN
1

UNLINKED CITATIONS
22

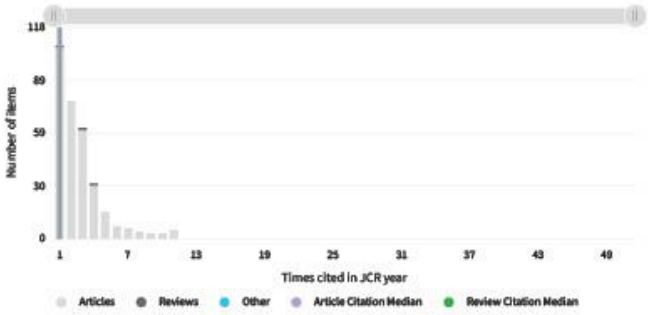

TIMES CITED
0

ARTICLES
118

REVIEWS
2

OTHER
5

Open Access (OA)

Export

The data included in this tile summarizes the items published in the journal in the JCR data year and in the previous two years. This three-year set of published items is used to provide descriptive analysis of the content and community of the journal. Learn more

Items

TOTAL CITABLE	% OF CITABLE OA
712	8.99%

Citations*

TOTAL CITABLE	% OF CITABLE OA
985	12.69%

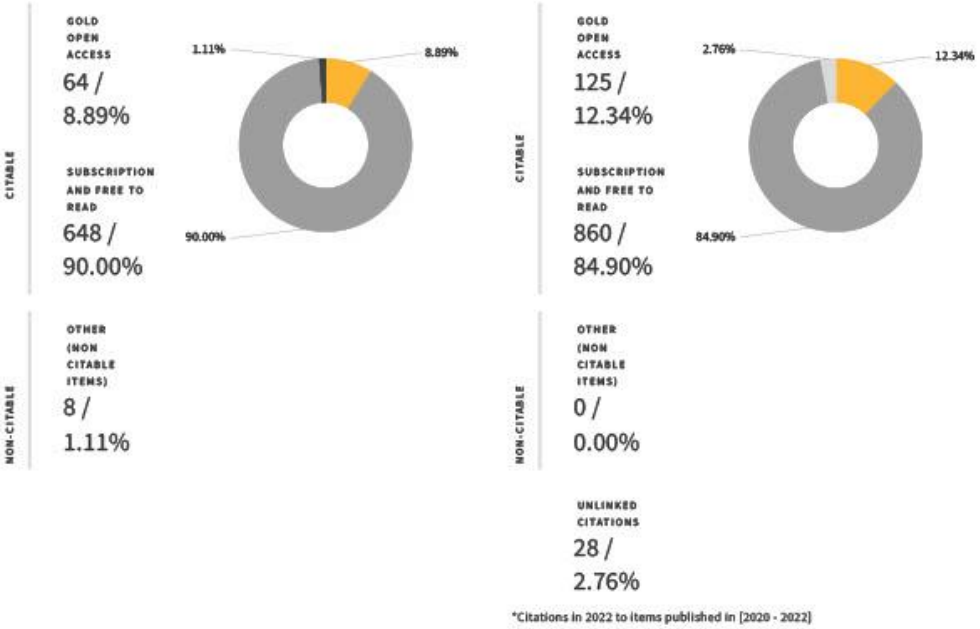

Rank by Journal Impact Factor

Journals within a category are sorted in descending order by Journal Impact Factor (JIF) resulting in the Category Ranking below. A separate rank is shown for each category in which the journal is listed in JCR. Data for the most recent year is presented at the top of the list, with other years shown in reverse chronological order. Learn more

EDITION
Science Citation Index Expanded (SCIE)

CATEGORY
GEOSCIENCES, MULTIDISCIPLINARY
136/202

JCR YEAR	JIF RANK	JIF QUARTILE	JIF PERCENTILE
2022	136/202	Q3	32.9
2021	155/202	Q4	23.51
2020	127/200	Q3	36.75
2019	116/200	Q3	42.25
2018	N/A	N/A	N/A

EDITION
Science Citation Index Expanded (SCIE)

CATEGORY
MINING & MINERAL PROCESSING
12/20

JCR YEAR	JIF RANK	JIF QUARTILE	JIF PERCENTILE
2022	12/20	Q3	42.5
2021	12/20	Q3	42.50
2020	12/21	Q3	45.24
2019	9/21	Q2	59.52
2018	N/A	N/A	N/A

Rank by Journal Citation Indicator (JCI)

Journals within a category are sorted in descending order by Journal Citation Indicator (JCI) resulting in the Category Ranking below. A separate rank is shown for each category in which the journal is listed in JCR. Data for the most recent year is presented at the top of the list, with other years shown in reverse chronological order. Learn more

CATEGORY
GEOSCIENCES, MULTIDISCIPLINARY
141/249

JCR YEAR	JCI RANK	JCI QUARTILE	JCI PERCENTILE
2022	141/249	Q3	43.57
2021	139/245	Q3	43.47
2020	98/239	Q2	59.21
2019	86/239	Q2	64.23
2018	77/231	Q2	66.88
2017	97/226	Q2	57.30

CATEGORY
MINING & MINERAL PROCESSING
13/32

JCR YEAR	JCI RANK	JCI QUARTILE	JCI PERCENTILE
2022	13/32	Q2	60.94
2021	12/31	Q2	62.90
2020	7/30	Q1	78.33
2019	5/29	Q1	84.48
2018	5/26	Q1	82.69
2017	6/26	Q1	78.85

Citation network

Cited Half-life

7.9 years

The Cited Half-Life is the median age of the items in this journal that were cited in the JCR year. Half of a journal's cited items were published more recently than the cited half-life.

TOTAL NUMBER OF CITES
7,529

NON SELF-CITATIONS
6,872

SELF-CITATIONS
657

Citing Half-life

11.1 years

The Citing Half-Life is the median age of items in other publications cited by this journal in the JCR year.

TOTAL NUMBER OF CITES
11,714

NON SELF-CITATIONS
11,057

SELF-CITATIONS
657

Cited Half-life Data | Citing Half-life Data

Export

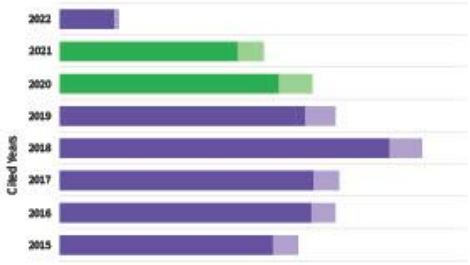

CITED YEAR	# OF CITES FROM 2022	CUMULATIVE %	# OF CITING SOURCES
All years	7,529 citations	100.00%	866 sources
2022	116 citations	1.54%	65 sources
2021	401 citations	6.87%	170 sources
2020	496 citations	13.45%	204 sources
2019	542 citations	20.65%	199 sources
2018	712 citations	30.11%	230 sources
2017	549 citations	37.40%	203 sources
2016	542 citations	44.60%	200 sources

Journal Citation Relationships

Cited Data | Citing Data

Top 20 journals citing J APPL GEOPHYS by number of citations

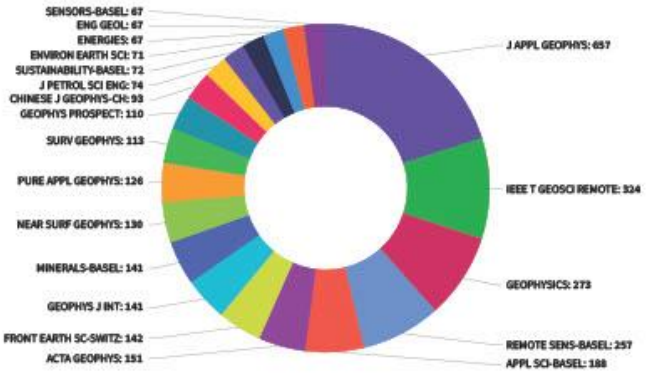

Content metrics

Source data

Average JIF Percentile

Export

This tile shows the breakdown of document types published by the journal. Citable Items are Articles and Reviews. For the purposes of calculating JIF, a JCR year considers the publications of that journal in the two prior years. Learn more

271 total citable items

	ARTICLES	REVIEWS	COMBINED(C)	OTHER DOCUMENT TYPES(O)	PERCEN
NUMBER IN JCR YEAR 2022 (A)	271	0	271	3	99%
NUMBER OF REFERENCES (B)	11,711	0	11,711	3	100%
RATIO (B/A)	43.2	N/A	43.2	1.0	

The Average Journal Impact Factor Percentile takes the sum of the JIF Percentile rank for each category under consideration, then calculates the average of those values. Learn more

ALL CATEGORIES AVERAGE
37.7

EDITION
Science Citation Index Expanded

GEOSCIENCES, MULTIDISCIPLINARY
32.9

MINING & MINERAL PROCESSING
42.5

Contributions by organizations

Export

Organizations that have contributed the most papers to the journal in the most recent three-year period. Learn more

RANK	ORGANIZATION	COUNT
1	CHINESE ACADEMY OF SCIENCES	37
2	CHINA UNIVERSITY OF GEOSCIENCES	35
3	CHINA UNIVERSITY OF PETROLEUM	33
4	CENTRAL SOUTH UNIVERSITY	32
-	JILIN UNIVERSITY	32
6	ZHEJIANG UNIVERSITY	27

Contributions by country/region

Export

Countries or Regions that have contributed the most papers to the journal in the most recent three-year period. Learn more

RANK	COUNTRY / REGION	COUNT
1	CHINA MAINLAND	302
2	USA	72
3	Brazil	46
-	India	46
5	GERMANY (FED REP GER)	42
6	Iran	36
7	France	24
-	Italy	24

Additional metrics

Eigenfactor Score
0.00566

Normalized Eigenfactor
1.23225

Article influence score
0.541

The Eigenfactor Score is a reflection of the density of the network of citations around the journal using 5 years of cited content as cited by the Current Year. It considers both the number of citations and the source of those citations, so that highly cited sources will influence the network more than less cited sources. The Eigenfactor calculation does not include journal self-citations. Learn more

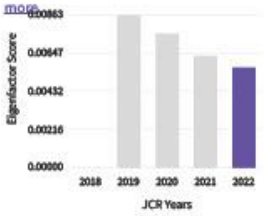

The Normalized Eigenfactor Score is the Eigenfactor score normalized, by rescaling the total number of journals in the JCR each year, so that the average journal has a score of 1. Journals can then be compared and influence measured by their score relative to 1. Learn more

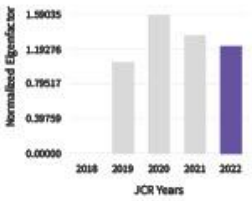

The Article Influence Score normalizes the Eigenfactor Score according to the cumulative size of the cited journal across the prior five years. The mean Article Influence Score for each article is 1.00. A score greater than 1.00 indicates that each article in the journal has above-average influence. Learn more

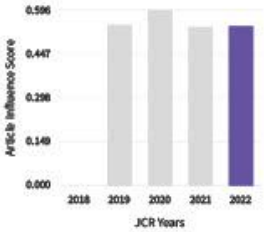

5 Year Impact Factor

2.3

View Calculation

The 5-year Impact Factor is the average number of times articles from the journal published in the past five years have been cited in the JCR year. It is calculated by dividing the number of citations in the JCR year by the total number of articles published in the five previous years. Learn more

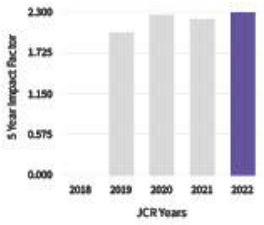

Immediacy Index

0.4

View Calculation

The Immediacy Index is the count of citations in the current year to the journal that reference content in this same year. Journals that have a consistently high Immediacy Index attract citations rapidly. Learn more

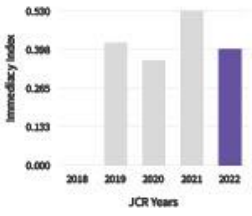

Products

Journal Citation Reports™ Journals Categories Publis My favorites Sign In Register

Home > Journal profile

Favorite Export

JCR YEAR

2022

Drones

Open Access since 2017

ISSN

N/A

EISSN

2504-446X

JCR ABBREVIATION

DRONES-BASEL

ISO ABBREVIATION

Drones-Basel

Journal information

EDITION

Science Citation Index Expanded (SCIE)

CATEGORY

REMOTE SENSING - SCIE

LANGUAGES	REGION	1ST ELECTRONIC JCR YEAR
English	SWITZERLAND	2021

Publisher information

PUBLISHER	ADDRESS	PUBLICATION FREQUENCY
MDPI	ST ALBAN-ANLAGE 66, CH-4052 BASEL, SWITZERLAND	12 issues/year

Journal's performance

Journal Impact Factor

The Journal Impact Factor (JIF) is a journal-level metric calculated from data indexed in the Web of Science Core Collection. It should be used with careful attention to the many factors that influence citation rates, such as the volume of publication and citations characteristics of the subject area and type of journal. The Journal Impact Factor can complement expert opinion and informed peer review. In the case of academic evaluation for tenure, it is inappropriate to use a journal-level metric as a proxy measure for individual researchers, institutions, or articles. Learn more

2022 JOURNAL IMPACT FACTOR	JOURNAL IMPACT FACTOR WITHOUT SELF CITATIONS
4.8	3.9
View calculation	View calculation

Journal Impact Factor Trend 2022 Export

Journal Impact Factor contributing items Export

Citable items (227) Citing Sources (346)

TITLE	CITATION COUNT
A Comprehensive Review of Applications of Drone Technology in the Mining…	34

15

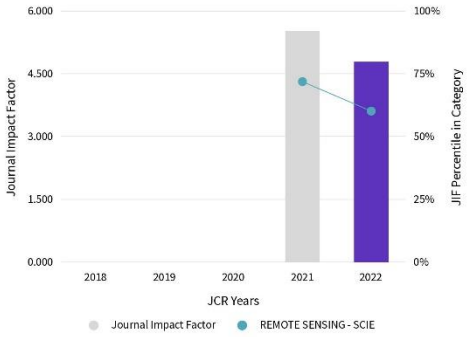

View all years

Coastal Mapping Using DJI Phantom 4 RTK in Post-Processing Kinematic Mode	24	˅
Operational Protocols for the Use of Drones in Marine Animal Research	23	˅
The Drone Revolution of Shark Science: A Review	22	˅
A Review on Communications Perspective of Flying Ad-Hoc Network…	21	˅
Ground Control Point Distribution for Accurate Kilometre-Scale Topographic…	20	˅
The Application of Drones in Healthcare and Health-Related Services in North…	19	˅
UAV-Enabled Mobile Edge-Computing for IoT Based on AI: A Comprehensive…	18	˅
A Citizen Science Unmanned Aerial System Data Acquisition Protocol and…	17	˅
Unmanned Aerial Vehicles for Wildland Fires: Sensing, Perception, Cooperatio…	16	˅

View All in Web of Science

Journal Citation Indicator (JCI)

Export

0.91

The Journal Citation Indicator (JCI) is the average Category Normalized Citation Impact (CNCI) of citable items (articles & reviews) published by a journal over a recent three year period. The average JCI in a category is 1. Journals with a JCI of 1.5 have 50% more citation impact than the average in that category. It may be used alongside other metrics to help you evaluate journals. Learn more

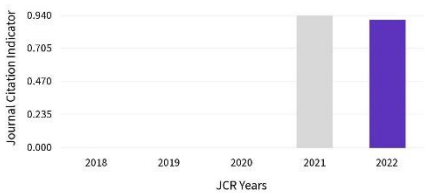

View all years

Total Citations

Export

2,543

The total number of times that a journal has been cited by all journals included in the database in the JCR year. Citations to journals listed in JCR are compiled annually from the JCR years combined database, regardless of which JCR edition lists the journal.

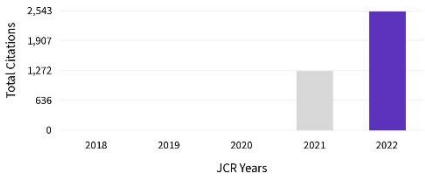

View all years

Citation distribution

Export

The Citation Distribution shows the frequency with which items published in the year or two years prior were cited in the JCR data year (i.e., the component of the calculation of the JIF). The graph has similar functionality as the JIF Trend graph, including hover-over data descriptions for each data point, and an interactive legend where each data element's legend can be used as a toggle. You can view Articles, Reviews, or Non-Citable (other) items to the JIF numerator. Learn more

ARTICLE CITATION MEDIAN
3

REVIEW CITATION MEDIAN
11

UNLINKED CITATIONS
8

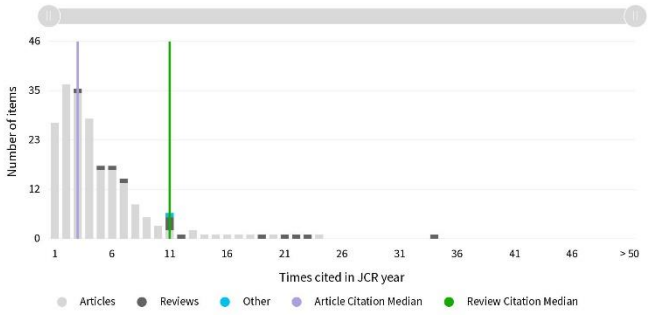

TIMES CITED
0

ARTICLES
17

REVIEWS
0

OTHER
0

Open Access (OA)

Export

The data included in this tile summarizes the items published in the journal in the JCR data year and in the previous two years. This three-year set of published items is used to provide descriptive analysis of the content and community of the journal. Learn more

Items

TOTAL CITABLE	% OF CITABLE OA
654	99.69%

Citations*

TOTAL CITABLE	% OF CITABLE OA
1,658	99.64%

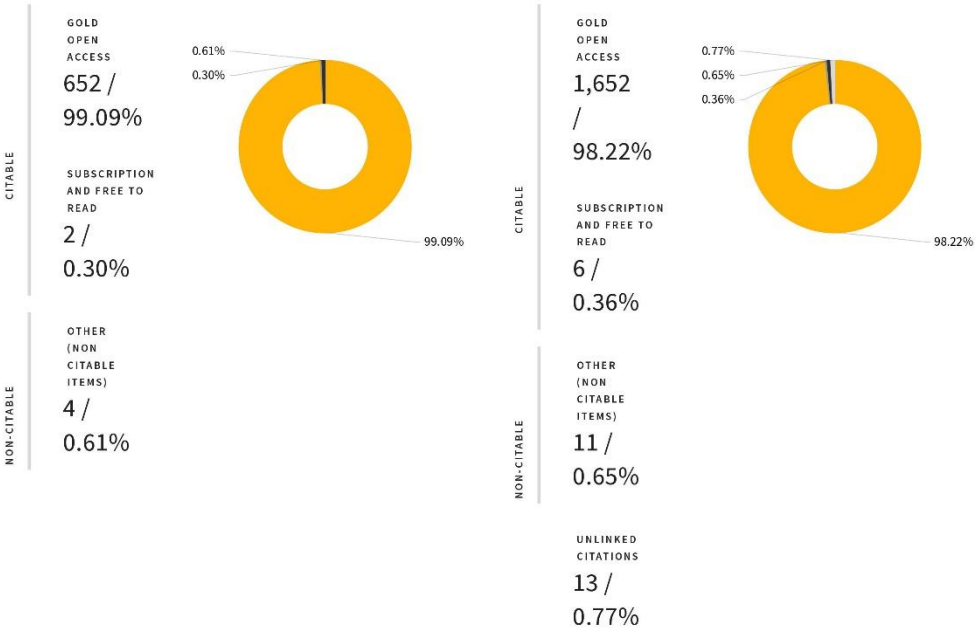

*Citations in 2022 to items published in [2020 - 2022]

Rank by Journal Impact Factor

Journals within a category are sorted in descending order by Journal Impact Factor (JIF) resulting in the Category Ranking below. A separate rank is shown for each category in which the journal is listed in JCR. Data for the most recent year is presented at the top of the list, with other years shown in reverse chronological order. Learn more

EDITION
Science Citation Index Expanded (SCIE)

CATEGORY
REMOTE SENSING
14/34

JCR YEAR	JIF RANK	JIF QUARTILE	JIF PERCENTILE
2022	14/34	Q2	60.3
2021	10/34	Q2	72.06

Rank by Journal Citation Indicator (JCI)

Journals within a category are sorted in descending order by Journal Citation Indicator (JCI) resulting in the Category Ranking below. A separate rank is shown for each category in which the journal is listed in JCR. Data for the most recent year is presented at the top of the list, with other years shown in reverse chronological order. Learn more

CATEGORY
REMOTE SENSING
18/59

JCR YEAR	JCI RANK	JCI QUARTILE	JCI PERCENTILE
2022	18/59	Q2	70.34
2021	18/57	Q2	69.30

Citation network

Cited Half-life

2.1 years

The Cited Half-Life is the median age of the items in this journal that were cited in the JCR year. Half of a journal's cited items were published more recently than the cited half-life.

TOTAL NUMBER OF CITES
2,543
NON SELF-CITATIONS
1,989
SELF-CITATIONS
554

Citing Half-life

4.6 years

The Citing Half-Life is the median age of items in other publications cited by this journal in the JCR year.

TOTAL NUMBER OF CITES
20,275
NON SELF-CITATIONS
19,721
SELF-CITATIONS
554

Cited Half-life Data | Citing Half-life Data

Export

CITED YEAR	# OF CITES FROM 2022	CUMULATIVE %	# OF CITING SOURCES
All years	**2,543 citations**	**100.00%**	**606 sources**
2022	587 citations	23.08%	143 sources
2021	641 citations	48.29%	216 sources

Journal Citation Relationships

Cited Data | Citing Data

Top 20 journals citing DRONES-BASEL by number of citations

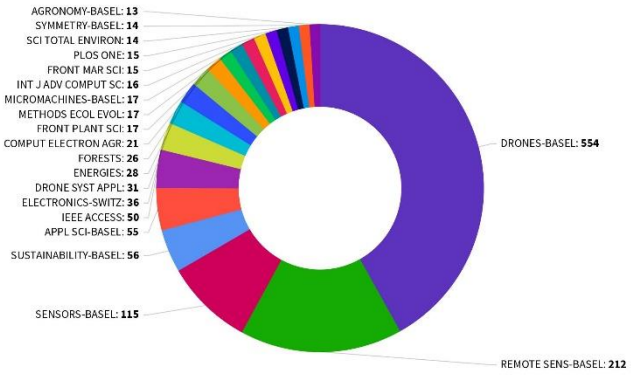

Content metrics

Source data

This tile shows the breakdown of document types published by the journal. Citable Items are Articles and Reviews. For the purposes of calculating JIF, a JCR year considers the publications of that journal in the two prior years. Learn more

427 total citable items

	ARTICLES	REVIEWS	COMBINED(C)	OTHER DOCUMENT TYPES(O)	PERCENTAGE
NUMBER IN JCR YEAR 2022 (A)	408	19	427	3	99%
NUMBER OF REFERENCES (B)	18,289	1,982	20,271	4	100%
RATIO (B/A)	44.8	104.3	47.5	1.3	

Contributions by organizations

Export

Organizations that have contributed the most papers to the journal in the most recent three-year period. Learn more

RANK	ORGANIZATION	COUNT
1	NATIONAL UNIVERSITY OF DEFENSE TECHNOLOGY - CHINA	23
2	BEIHANG UNIVERSITY	14
-	NANJING UNIVERSITY OF AERONAUTICS & ASTRONAUTICS	14
4	UNIVERSITY OF NEW SOUTH WALES SYDNEY	13
5	CENTRE NATIONAL DE LA RECHERCHE SCIENTIFIQUE (CNRS)	10
-	CHINESE ACADEMY OF SCIENCES	10

Contributions by country/region

Export

Countries or Regions that have contributed the most papers to the journal in the most recent three-year period. Learn more

RANK	COUNTRY / REGION	COUNT
1	CHINA MAINLAND	150
2	USA	107
3	Italy	53
4	Australia	47
5	Spain	34
6	Saudi Arabia	30
7	South Korea	29
8	England	28
9	Canada	27

Additional metrics

Eigenfactor Score

0.00240

The Eigenfactor Score is a reflection of the density of the network of citations around the journal using 5 years of cited content as cited by the Current Year. It considers both the number of citations and the source of those citations, so that highly cited sources will influence the network more than less cited sources. The

Normalized Eigenfactor

0.52358

The Normalized Eigenfactor Score is the Eigenfactor score normalized, by rescaling the total number of journals in the JCR each year, so that the average journal has a score of 1. Journals can then be compared and influence measured by their score relative to 1. Learn more

Article influence score

0.773

The Article Influence Score normalizes the Eigenfactor Score according to the cumulative size of the cited journal across the prior five years. The mean Article Influence Score for each article is 1.00. A score greater than 1.00 indicates that each article in the journal has above-average influence. Learn more

15

Eigenfactor calculation does not include journal self-citations. Learn more

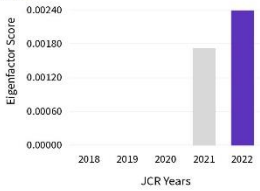

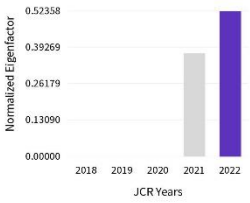

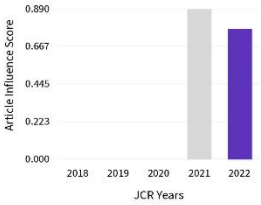

5 Year Impact Factor

5.5

View Calculation

The 5-year Impact Factor is the average number of times articles from the journal published in the past five years have been cited in the JCR year. It is calculated by dividing the number of citations in the JCR year by the total number of articles published in the five previous years. Learn more

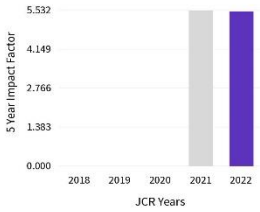

Immediacy Index

1.4

View Calculation

The Immediacy Index is the count of citations in the current year to the journal that reference content in this same year. Journals that have a consistently high Immediacy Index attract citations rapidly. Learn more

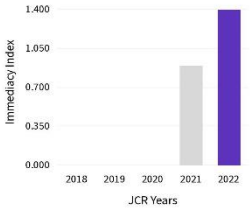

Products

Journal Citation Reports™ Journals Categories Publis My favorites Sign In Register

Search results > Journal profile

Favorite Export

JCR YEAR

2022

Applied Sciences-Basel

Open Access since 2011

ISSN

N/A

EISSN

2076-3417

JCR ABBREVIATION

APPL SCI-BASEL

ISO ABBREVIATION

Appl. Sci.-Basel

Journal information

EDITION

Science Citation Index Expanded (SCIE)

CATEGORY

CHEMISTRY, MULTIDISCIPLINARY - SCIE

MATERIALS SCIENCE, MULTIDISCIPLINARY - SCIE

PHYSICS, APPLIED - SCIE

ENGINEERING, MULTIDISCIPLINARY - SCIE

LANGUAGES	REGION	1ST ELECTRONIC JCR YEAR
English	SWITZERLAND	2014

Publisher information

PUBLISHER	ADDRESS	PUBLICATION FREQUENCY
MDPI	ST ALBAN-ANLAGE 66, CH-4052 BASEL, SWITZERLAND	24 issues/year

Journal's performance

Journal Impact Factor

The Journal Impact Factor (JIF) is a journal-level metric calculated from data indexed in the Web of Science Core Collection. It should be used with careful attention to the many factors that influence citation rates, such as the volume of publication and citations characteristics of the subject area and type of journal. The Journal Impact Factor can complement expert opinion and informed peer review. In the case of academic evaluation for tenure, it is inappropriate to use a journal-level metric as a proxy measure for individual researchers, institutions, or articles. Learn more

2022 JOURNAL IMPACT FACTOR	JOURNAL IMPACT FACTOR WITHOUT SELF CITATIONS

Journal Impact Factor contributing items Export 15

2.7

View calculation

2.4

View calculation

Journal Impact Factor Trend 2022 Export

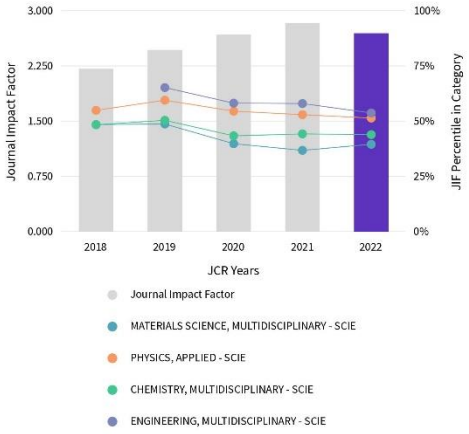

View all years

Citable items (21,030) Citing Sources (6,128)

TITLE	CITATION COUNT
A Novel K-Means Clustering Algorithm with a Noise Algorithm for Capturing…	110
Observation of Potential Contaminants in Processed Biomass Using Fourier…	89
A Novel Transfer Learning Based Approach for Pneumonia Detection in…	88
Sentence Representation Method Based on Multi-Layer Semantic Network	78
The Impact of Drought in Plant Metabolism: How to Exploit Tolerance…	77
Diversity of Synthetic Dyes from Textile Industries, Discharge Impacts and…	75
A Novel Advancing Signal Processing Method Based on Coupled Multi-Stabl…	66
Transfer Learning with Deep Convolutional Neural Network (CNN) f…	61
A Review of the Potential Climate Change Impacts and Adaptation Optio…	60
Peak Fitting Applied to Fourier Transform Infrared and Raman…	57

View All in Web of Science

Journal Citation Indicator (JCI)

Export

0.57

The Journal Citation Indicator (JCI) is the average Category Normalized Citation Impact (CNCI) of citable items (articles & reviews) published by a journal over a recent three year period. The average JCI in a category is 1. Journals with a JCI of 1.5 have 50% more citation impact than the average in that category. It may be used alongside other metrics to help you evaluate journals. Learn more

Total Citations

Export

98,949

The total number of times that a journal has been cited by all journals included in the database in the JCR year. Citations to journals listed in JCR are compiled annually from the JCR years combined database, regardless of which JCR edition lists the journal.

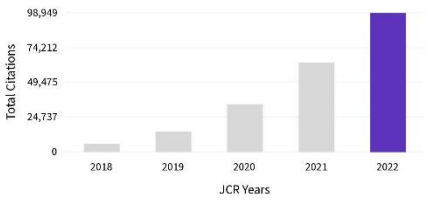

15

View all years

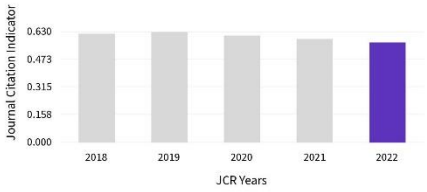

View all years

Citation distribution

Export

The Citation Distribution shows the frequency with which items published in the year or two years prior were cited in the JCR data year (i.e., the component of the calculation of the JIF). The graph has similar functionality as the JIF Trend graph, including hover-over data descriptions for each data point, and an interactive legend where each data element's legend can be used as a toggle. You can view Articles, Reviews, or Non-Citable (other) items to the JIF numerator. Learn more

ARTICLE CITATION MEDIAN

1

REVIEW CITATION MEDIAN

4

UNLINKED CITATIONS

714

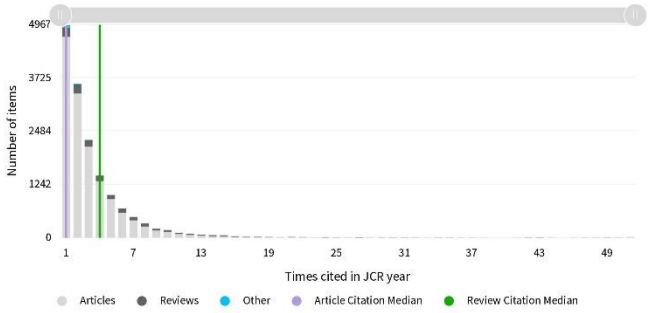

TIMES CITED

0

ARTICLES

5,064

REVIEWS

169

OTHER

200

Open Access (OA)

Export

The data included in this tile summarizes the items published in the journal in the JCR data year and in the previous two years. This three-year set of published items is used to provide descriptive analysis of the content and community of the journal. Learn more

Items

TOTAL CITABLE	% OF CITABLE OA
33,771	99.30%

Citations*

TOTAL CITABLE	% OF CITABLE OA
65,765	99.08%

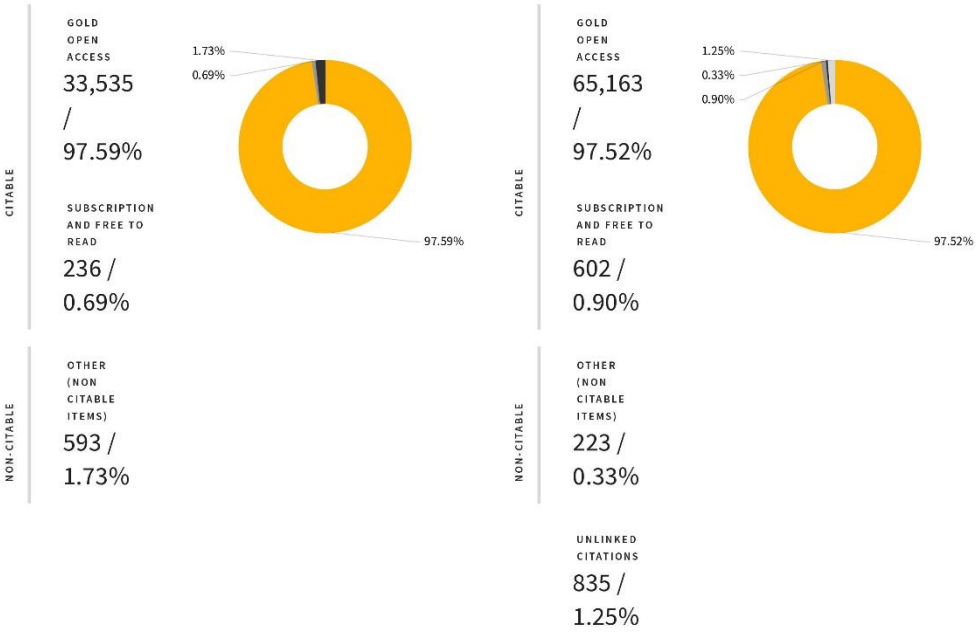

*Citations in 2022 to items published in [2020 - 2022]

Rank by Journal Impact Factor

Journals within a category are sorted in descending order by Journal Impact Factor (JIF) resulting in the Category Ranking below. A separate rank is shown for each category in which the journal is listed in JCR. Data for the most recent year is presented at the top of the list, with other years shown in reverse chronological order. Learn more

EDITION
Science Citation Index Expanded (SCIE)

CATEGORY
CHEMISTRY, MULTIDISCIPLINARY
100/178

JCR YEAR	JIF RANK	JIF QUARTILE	JIF PERCENTILE
2022	100/178	Q3	44.1
2021	100/179	Q3	44.41
2020	101/178	Q3	43.54
2019	88/177	Q2	50.56
2018	89/172	Q3	48.55

EDITION
Science Citation Index Expanded (SCIE)

CATEGORY
ENGINEERING, MULTIDISCIPLINARY
42/90

JCR YEAR	JIF RANK	JIF QUARTILE	JIF PERCENTILE
2022	42/90	Q2	53.9
2021	39/92	Q2	58.15
2020	38/90	Q2	58.33
2019	32/91	Q2	65.38
2018	N/A	N/A	N/A

Rank by Journal Citation Indicator (JCI)

Journals within a category are sorted in descending order by Journal Citation Indicator (JCI) resulting in the Category Ranking below. A separate rank is shown for each category in which the journal is listed in JCR. Data for the most recent year is presented at the top of the list, with other years shown in reverse chronological order. Learn more

CATEGORY
CHEMISTRY, MULTIDISCIPLINARY
97/230

JCR YEAR	JCI RANK	JCI QUARTILE	JCI PERCENTILE
2022	97/230	Q2	58.04
2021	90/224	Q2	60.04
2020	84/219	Q2	61.87
2019	73/215	Q2	66.28
2018	71/212	Q2	66.75
2017	81/205	Q2	60.73

CATEGORY
ENGINEERING, MULTIDISCIPLINARY
65/178

JCR YEAR	JCI RANK	JCI QUARTILE	JCI PERCENTILE
2022	65/178	Q2	63.76
2021	63/175	Q2	64.29
2020	55/170	Q2	67.94
2019	57/169	Q2	66.57
2018	56/168	Q2	66.96
2017	69/168	Q2	59.23

Citation network

Cited Half-life

2.4 years

The Cited Half-Life is the median age of the items in this journal that were cited in the JCR year. Half of a journal's cited items were published more recently than the cited half-life.

TOTAL NUMBER OF CITES
98,949

NON SELF-CITATIONS
88,372

SELF-CITATIONS
10,577

Citing Half-life

6.3 years

The Citing Half-Life is the median age of items in other publications cited by this journal in the JCR year.

TOTAL NUMBER OF CITES
576,866

NON SELF-CITATIONS
566,289

SELF-CITATIONS
10,577

Cited Half-life Data | Citing Half-life Data

Export

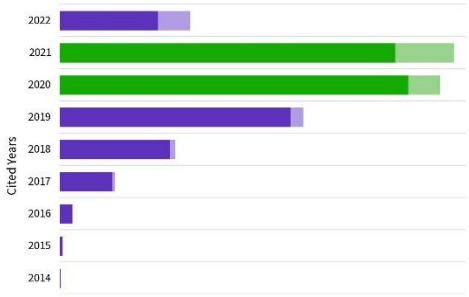

CITED YEAR	# OF CITES FROM 2022	CUMULATIVE %	# OF CITING SOURCES
All years	**98,949 citations**	**100.00%**	**6,782 sources**
2022	9,637 citations	9.74%	1,688 sources
2021	29,106 citations	39.15%	4,034 sources
2020	28,080 citations	67.53%	4,356 sources
2019	17,984 citations	85.71%	3,446 sources
2018	8,530 citations	94.33%	2,275 sources
2017	4,062 citations	98.43%	1,440 sources
2016	969 citations	99.41%	536 sources
2015	223 citations	99.64%	167 sources

Journal Citation Relationships

Cited Data | Citing Data

Top 20 journals citing APPL SCI-BASEL by number of citations

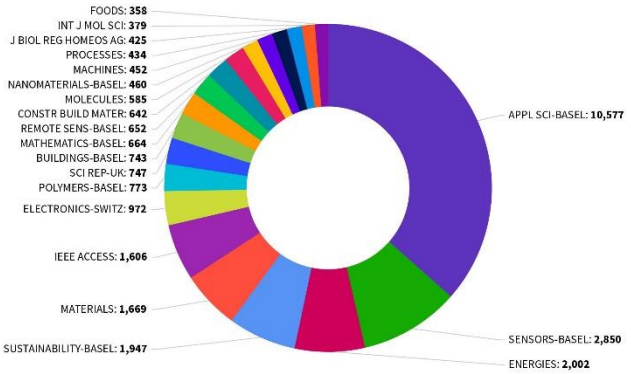

Content metrics

Source data

Average JIF Percentile

Expor... 15

This tile shows the breakdown of document types published by the journal. Citable Items are Articles and Reviews. For the purposes of calculating JIF, a JCR year considers the publications of that journal in the two prior years. Learn more

12,741 total citable items

	ARTICLES	REVIEWS	COMBINED(C)	OTHER DOCUMENT TYPES(O)	PERCEN
NUMBER IN JCR YEAR 2022 (A)	12,099	642	12,741	303	98%
NUMBER OF REFERENCES (B)	506,501	66,283	572,784	4,082	99%
RATIO (B/A)	41.9	103.2	45.0	13.5	

The Average Journal Impact Factor Percentile takes the sum of the JIF Percentile rank for each category under consideration, then calculates the average of those values. Learn more

ALL CATEGORIES AVERAGE
47.3

EDITION
Science Citation Index Expanded

MATERIALS SCIENCE, MULTIDISCIPLINARY
39.7

CHEMISTRY, MULTIDISCIPLINARY
44.1

ENGINEERING, MULTIDISCIPLINARY

Contributions by organizations

Export

Organizations that have contributed the most papers to the journal in the most recent three-year period. Learn more

RANK	ORGANIZATION	COUNT
1	CHINESE ACADEMY OF SCIENCES	811
2	EGYPTIAN KNOWLEDGE BANK (EKB)	421
3	CONSIGLIO NAZIONALE DELLE RICERCHE (CNR)	382
4	CENTRE NATIONAL DE LA RECHERCHE SCIENTIFIQUE (CNRS)	350
5	KING SAUD UNIVERSITY	281
-	RUSSIAN ACADEMY OF SCIENCES	281
7	CENTRAL SOUTH UNIVERSITY	273

Contributions by country/region

Export

Countries or Regions that have contributed the most papers to the journal in the most recent three-year period. Learn more

RANK	COUNTRY / REGION	COUNT
1	CHINA MAINLAND	9116
2	South Korea	4428
3	Italy	3398
4	Spain	2460
5	USA	2018
6	Poland	1726
7	GERMANY (FED REP GER)	1422
8	Taiwan	1333
9	Saudi Arabia	1250

Additional metrics

Eigenfactor Score
0.11103

Normalized Eigenfactor
24.16562

Article influence score
0.414

15

The Eigenfactor Score is a reflection of the density of the network of citations around the journal using 5 years of cited content as cited by the Current Year. It considers both the number of citations and the source of those citations, so that highly cited sources will influence the network more than less cited sources. The Eigenfactor calculation does not include journal self-citations. Learn more

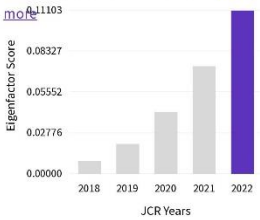

The Normalized Eigenfactor Score is the Eigenfactor score normalized, by rescaling the total number of journals in the JCR each year, so that the average journal has a score of 1. Journals can then be compared and influence measured by their score relative to 1. Learn more

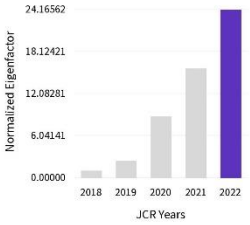

The Article Influence Score normalizes the Eigenfactor Score according to the cumulative size of the cited journal across the prior five years. The mean Article Influence Score for each article is 1.00. A score greater than 1.00 indicates that each article in the journal has above-average influence. Learn more

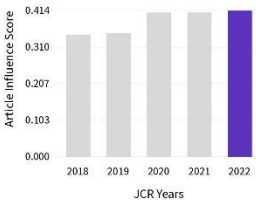

5 Year Impact Factor

2.9

View Calculation

The 5-year Impact Factor is the average number of times articles from the journal published in the past five years have been cited in the JCR year. It is calculated by dividing the number of citations in the JCR year by the total number of articles published in the five previous years. Learn more

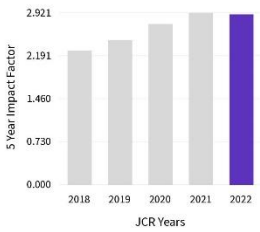

Immediacy Index

0.8

View Calculation

The Immediacy Index is the count of citations in the current year to the journal that reference content in this same year. Journals that have a consistently high Immediacy Index attract citations rapidly. Learn more